SEISMIC PHENOMENA CONNECTED WITH EARTHQUAKES AND EXPLOSIONS

David G. Harkrider

California Institute of Technology

Prepared for:

Air Force Office of Scientific Research
Advanced Research Projects Agency

28 May 1974

UNCLASSIFIED

SECURITY CLASSIFICATION OF THIS PAGE (When Data Entered)

AD 783 326

REPORT DOCUMENTATION PAGE	READ INSTRUCTIONS BEFORE COMPLETING FORM
1. REPORT NUMBER: AFOSR - TR - 74 - 1287	2. GOVT ACCESSION NO. / 3. RECIPIENT'S CATALOG NUMBER
4. TITLE (and Subtitle): Seismic Phenomena Connected with Earthquakes and Explosions	5. TYPE OF REPORT & PERIOD COVERED: Annual Technical Report 15 March 1973 - 14 March 197[illegible]
	6. PERFORMING ORG. REPORT NUMBER
7. AUTHOR(s): David G. Harkrider	8. CONTRACT OR GRANT NUMBER(s): F44620-72-C-0078
9. PERFORMING ORGANIZATION NAME AND ADDRESS: California Institute of Technology, Seismological Laboratory, P.O. Bin 2 - Arroyo Annex, Pasadena, CA 91109	10. PROGRAM ELEMENT, PROJECT, TASK AREA & WORK UNIT NUMBERS: 62701E, AO 1827
11. CONTROLLING OFFICE NAME AND ADDRESS: Advanced Research Projects Agency/NMR, 1400 Wilson Blvd., Arlington, Va. 22209	12. REPORT DATE: 28 May 1974
	13. NUMBER OF PAGES: 167
14. MONITORING AGENCY NAME & ADDRESS(if different from Controlling Office): Air Force Office of Scientific Research/NP, 1400 Wilson Blvd., Arlington, VA 22209	15. SECURITY CLASS. (of this report): Unclassified
	15a. DECLASSIFICATION/DOWNGRADING SCHEDULE

16. DISTRIBUTION STATEMENT (of this Report)

Approved for public release; distribution unlimited.

17. DISTRIBUTION STATEMENT (of the abstract entered in Block 20, if different from Report)

18. SUPPLEMENTARY NOTES

19. KEY WORDS (Continue on reverse side if necessary and identify by block number)

detection
discrimination
seismic sources
shear velocities
earthqu akes models
earth models
crustal structure

20. ABSTRACT (Continue on reverse side if necessary and identify by block number)

The spatial and frequency distribution of path-corrected Rayleigh waves from the San Fernando earthquake are systematically related to the faulting process as a multiple event. The surface wave source is taken to be a depth-distributed set of double couples. A least-squares inversion is used to find the set of source parameters which optimally fit the variance-weighted data. In this study the strength, the slip angle, and the rupture delay times are optimally determined for the spatially

12

DD FORM 1 JAN 73 1473 EDITION OF 1 NOV 65 IS OBSOLETE

20. Abstract Cont'd.

assumed distribution of double couples. A sophisticated error analysis is performed to estimate the uncertainties of the calculated model variables.

One of the interesting side results from this inversion technique is the a priori determination of what azimuthal distribution of observations is most beneficial in determining the source parameters, the uncertainties in the calculated model parameters, and the relative coupling between various parameters. Of the 18 WWSSN stations used for this event, two stations contain a total of 30% of the total information in the data set. In fact, the data set could have been reduced by one-half and only 25% of the total information which constrains the model variables would have been lost.

Transversely polarized shear waves (SH) from well located earthquakes are used to determine an upper mantle shear velocity structure compatible with both travel times and waveforms of observed seismograms. Vertically polarized shear waves (SV) are shown to be inadequate in identifying triplications because of contamination by PL-coupled shear waves and other P-SV interactions. The observed SH travel times are considerably slower than the JB values out to 30 degrees.

CONTENTS

I. Summary

This year's research in Seismic Phenomena Connected with Earthquakes and Explosions has concentrated on four task areas.

1) Evaluation of seismic discriminants
2) Understanding and determination of seismic source characteristics
3) Determination of the earth's seismic properties (i.e. velocity and density structure and Q^{-1})
4) Inversion of observations using crust and upper mantle properties to obtain the spatial and temporal characteristics of earthquakes and explosions

In the semiannual technical report, we reported on two different approaches for investigating the characteristics of the seismic source, in particular the determination of the corner frequency for P and S waves. The first uses theoretical volume source models of tectonic release of the Archambeau type and obtains numerically their P- and S-wave spectra. The spectra for these particular models show a definite difference in the P-waves and S-wave corner frequencies. This approach yields theoretical M_S vs m_b curves which can be discussed in terms of scaling by the various source parameters. The second approach is to obtain the earthquake P-wave source history from comparison of theoretical and observed seismograms. This history is then used as the S-wave source history to obtain theoretical seismograms which are compared with S-wave observations of the same events.

Two possible criticisms of the first approach is that the Archambeau type tectonic release source does not model the tectonic region realistically and that the

presence of a zero frequency minimum on the far-field spectrum is due to a questionable termination of the tectonic release region at a finite distance from the source. Archambeau claims that the approximation using a finite termination is realsistic and closer to actual field situations than using the same spatial release distribution to infinity. We are continuing research on tectonic release sources using more realistic models of tectonic stress distributions. In particular we are trying to determine for what stress and body force distributions the zero frequency minimum is a valid result.

The use of synthetic body and surface waves is becoming an extremely valuable tool in not only determining the character of the seismic source but also in defining the seismic propagation properties of the earth. In the semiannual report, we gave an example of a method using amplitudes and arrival times of body and Rayleigh waves from NTS events to determine an average crustal model from NTS to mid-Arizona. In this report, transversely polarized shear waves (SH) from well located earthquakes are used to determine an upper mantle shear velocity structure. It is further demonstrated that observations of travel times for vertically polarized shear waves (SV), the most common technique, can lead to erroneous shear structure models due to continuation of P-SV interactions.

In Section III, the spatial and frequency distribution of path-corrected Rayleigh waves from the San Fernando earthquake are systematically related to the faulting process as a multiple event. The surface wave source is taken to be a depth-distributed set of double couples. A least-squares inversion is used to find the set of source parameters which optimally fit

the variance-weighted data. In this study the strength, the slip angle, and the rupture delay times are optimally determined for the spatially assumed distribution of double couples. A sophisticated error analysis is performed to estimate the uncertainties of the calculated model variables.

One of the interesting side results from this inversion technique is the a priori determination of what azimuthal distribution of observations is most beneficial in determining the source parameters, the uncertainties in the calculated model parameters, and the relative coupling between various parameters. Of the 18 WWSSN stations used for this event, two stations contain a total of 30% of the total information in the data set. In fact, the data set could have been reduced by one-half and only 25% of the total information which constrains the model variables would have been lost.

One could visualize, using these inversion operators to design multiple explosion events which would make discrimination criteria unreliable except in azimuths where data was difficult to obtain. Of course, the inversion operators used here were for Rayleigh wave data only. For discrimination techniques based on Love and Rayleigh waves possibly combined with body waves the design would probably be extremely complicated and economically unfeasible.

Of equal importance, this section describes and uses techniques for correcting surface wave data for mixed path crustal structure between source and receiver, and for multipath propagation interference. The error bounds associated with these corrections are estimated, and their influence on the reliability of the model are determined.

Since the crust and upper-mantle shear structure dominate the propagation characteristics of Rayleigh and Love surface waves, Section IV deals

with an attempt at constructing a preliminary shear velocity model compatible with both travel times and waveforms of observed seismograms. Transversely polarized (SH) LRSM and WWSSN observations are used in the study. Vertically polarized shear waves (SV) are shown to be inadequate in identifying triplications because of contamination by PL-coupled shear waves and other P-SV interactions. Accurately located west coast earthquakes, modeled as shear dislocations, are used as sources. The observed SH travel times are considerably slower than the JB values out to 30 degrees. Select profiles of observed waveforms in conjunction with the travel-times provide the data for model determinations. This is accomplished by fitting the observed waveforms with synthetics.

Research is continuing on the relations between seismic source characteristics and magnitude. Recently Anderson and Kanimori have made a study on the relationships between energy, moment, magnitude and source dimensions. Using both deterministic and statistical source models, they have shown that the empirical Gutenberg-Richter magnitude-energy relationship has strong theoretical support and implies that rupture times for large earthquakes are much longer than rise times. In general, earthquake magnitudes (M) are proportional to L^2, where L is a linear source dimension, but $M \sim L^3$ for small events and $M \sim L$ for very large events. Interplate and intraplate earthquakes form separate populations in moment-magnitude, or moment-dimension plots. In each population the inferred stress drop and effective stress is roughly constant. The large scatter in plots involving magnitude is considerably reduced when earthquakes are grouped according to type. The scatter virtually disappears when magnitude is removed as a variable, e.g., dimensions versus moment plots.

II. Abstracts of Publications and Reports During This Contract Period

Helmberger, D.V., "Generalized Ray Theory for Shear Dislocations," Bull. Seism. Soc. Am., in press.

Displacements at the surface of a layered halfspace produced by a point source dislocation is investigated. Expressing the source in terms of P, SV and SH displacement potentials allows the solution to be expanded in generalized rays. The transient response for each ray is obtained by the Cagniard-deHoop method. First-motion and high-frequency asymptotic approximations of the exact solutions are discussed.

Numerical experiments on the far-field response produced by shallow dislocations are presented. Synthetic seismograms computed for a strike-slip dislocation are compared with some observations from the Borrego Mountain earthquake. Preliminary results indicate an equivalent point source depth of 9 km with the far-field time function approximated by a step function with an exponential decay. This time function fits both the P and S waveforms. The apparent shift in corner frequency between the P and S waves for shallow events as reported by some investigators is explained by surface reflections.

Kurita, T., "Upper Mantle Structure in the Central United States From P and S Wave Spectra[1]," Phys. Earth and Planet. Inter., in press.

In order to study regional variations in the upper mantle structure in the central United States, the second step of a two step procedure formulated in Kurita (1972a) has been taken and experimentally shown to be very powerful method for elucidating the fine configuration of the low-velocity zone. The strong advantage of this method as compared with the other methods, is a mutual independency of the extent of the velocity decrease and the depth to the bottom of the low-velocity zone. The upper mantle structure down to about 220 km in this region has been inferred from complex transfer ratios of long period P and S waves from deep-focus earthquakes recorded at FLO, OXF, and SHA on the basis of the crustal models obtained in Kurita (1972b). From the Interior Plain to the Gulf of Mexico the low-velocity zone shifts to a shallower depth while increasing its thickness and decreasing its velocity. This zone is about 50 km thick layer ranging in depth from about 150 to 200 km under the Interior Plain, about 75 km thick layer from about 120 to 195 km under the Gulf Coastal Plain, and about 80 km thick layer from about 95 to 175 km under the continental shelf of the Gulf of Mexico, all nearly along 89°N longitude. The decrease in S wave velocity at the top of this zone is about 0.30, 0.45, and 0.70 km/sec under each of the areas above, although the last value may be somewhat an overestimate. Both boundaries of this zone are sharp, the transition occurring over at most about 10 km. In this region the existence of the high-velocity lid zone is possible.

Geller, R.J., "Body Force Equivalents for Stress Drop Seismic Sources," submitted to Geophys. Journ.

When an earthquake point source is represented in the most general way (a stress drop source) six independent functions of time (the six stress drop elements) are required to describe the source. The common seismological practice of using a single time function for a point source model of actual earthquakes is not valid unless all six time functions are independently obtained from observed data and found to be the same. The difficulty first noted by Knopoff and Randall (1970) (that one double couple lacked sufficient degrees of freedom to represent an arbitrary point source but that there was not a unique decomposition of a source into a combination of a double couple and a compensated linear vector dipole (CLVD)) is shown to result from their choice of non-orthogonal basis elements. The unique equivalent force representation of an earthquake source is shown to be three perpendicular force doublets parallel to the principal axes of the stress drop tensor. The success of the double couple source model, a special case of the stress drop source, in matching most observations of shallow earthquakes implies, but does not require that most shallow earthquakes result from shear dislocations along essentially flat surfaces.

Geller, R.J., "Representation Theorems for an Infinite Shear Fault," submitted to Geophys. Journ.

The Green's function solutions for a shear dislocation with symmetry in the direction of infinite length have been integrated analytically over the direction of infinite length. The displacement solution is reduced from a surface integral over the fault plane to a line integral of temporal convolutions over the width of the fault. If the time history function of fault displacement is any piecewise linear function the convolutions can be integrated analytically, reducing the solutions to line integrals. Numerical results and plots are presented for a simple example. The two-dimensional solutions give exact first motions at points "over" the fault. Also the solutions can be used to test two-dimensional finite difference and finite element computer programs.

Helmberger, D.V. and Engen, G.R., "Upper-Mantle Shear Structure," submitted to Journ. of Geophys. Res.

This is an attempt at constructing a preliminary shear velocity model compatible with both travel times and waveforms of observed seismograms. Transversely polarized LRSM and WWSS observations are used in this study. SV signatures are demonstrated to be inadequate in identifying triplications because of contamination by PL-coupled shear waves and other P-SV interactions. Well located west coast earthquakes, modeled as shear dislocations, are used as sources. The observed SH travel times are considerably slower than the JB values out to 30 degrees. Select profiles

of observed waveforms in conjunction with the travel-times provide the data for model determinations. This is accomplished by fitting the observed waveforms with synthetics.

Synthetics are computed for a number of current models as preliminary attempts at fitting the data. Models containing large, sharp transitions predict strong second arrivals beyond 30°. Models containing low velocity zones between 400 and 700 km predict complicated waveshapes between 20 and 25°. None of the above features are apparent in observed SH waveforms. The final model is relatively smooth and exhibits the same characteristics as the HWB P-model, except that the percentage velocity jump is much less at 400 km and slightly larger at 500 km. The 600 km transition is subdued similar to the P-model.

Langston, C.A. and Helmberger, D.V., "Interpretation of Body and Rayleigh Waves from NTS to Tucson," submitted to Bull. Seism. Soc. Am.

A linear array of eight Caltech portable broad-band seismograph trailers was set out from NTS to near Phoenix, Arizona, for the pre-announced underground nuclear test, Oscuro, on September 21, 1972. Travel time and amplitude information were used to find an average crustal model by calculating synthetic seismograms using the Cagniard-deHoop method. Rayleigh waves from other nuclear events at NTS, as recorded at the Tucson WWSS station, were examined as a control for determining the structure of the top half of the crust. Group velocity curves were found and synthetic Rayleigh waves calculated for Tucson and Kingman (LRSM). The formations and characteristics of Pn, a reflected Pn, and the Pg phases were examined. Pg is demonstrated to be composed of the primary P reflection from the mantle and contains multiple arrivals of P-SV conversions. Comparisons of synthetic and observed seismograms indicate a crustal thickness of 30 km with a Poisson's ratio of .23. The crust-mantle transition appears to be sharp jumping from 6.1 to 7.9 km/sec. The amplitude behavior of Pn shows little evidence of any lid structure.

ABSTRACTS OF PAPERS PRESENTED AT MEETINGS DURING THIS CONTRACT PERIOD

Seismological Society of America, 1974 Joint Annual Meeting, May 29-31, 1974, Hilton Hotel, Las Vegas, Nevada.

Hanks, T.C., "Long-period Strong Ground Motion Following the San Fernando Earthquake."

Two hundred thirty-four components of ground displacement are the basis of an investigation of long-period (approximately 2-10 seconds) strong ground motion following the San Fernando, California, earthquake at local ($\Delta \leq 100$ km) distances. Seismic moment, source dimension, radiation pattern, source propagation, the development of surface waves together with their subsequent dispersion, and the local structure of the Los Angeles Basin all appear to have first order significance in the shaping of observed ground displacements and their variation with azimuth and epicentral distance. Long-period strong ground motion occurred with considerably greater amplitude at southern azimuths than at northern azimuths; at comparable epicentral distances amplitude differences approached a factor of 10. Radiation pattern alone seems insufficient to explain the observed variations. Especially strong signals at azimuths due south of the epicenter and the development of large amplitude (3-5 cm), long duration surface wave trains at stations along the southeastern margin of the Los Angeles Basin suggest the significant effect of this geologic structure on the observed ground displacements. Data redundancy at closely spaced stations in Los Angeles and at Lake Isabella Dam suggest that errors in ground displacement at periods near 8 seconds are approximately 1 cm and at periods near 15 seconds are several cm, for a record sensitivity of 7.6 cm/g.

Newton, C.A., "Temporal Changes in P-Wave Velocity Near Riverside, California."

P_n travel times from NTS to Goldstone and Riverside, California have been measured for the last eight years. During this period there have been four or more cycles of compressional velocity changes in the crust NNE of Riverside, but not necessarily limited to that area. Periods of lower velocity are associated with decreased seismicity and periods of higher velocity are associated with increased seismicity. These data suggest that this area which includes portions of the San Jacinto and San Andreas fault zones have repeatedly strained to a dilatant state and then fractured. The largest earthquake related to these velocity changes was a magnitude 5.4 shock which followed a low velocity period of approximately 450 days. It appears that this area is now in a dilatant state which began on August 1972.

Whitcomb, J.H., "P'P' Times and Average Mantle Velocities Under Continents and Oceans."

P'P' times are an important data type because they provide one of the few means at hand for comparison of mantle structure under different lithospheric regions such as continents and oceans. However, scatter of the

data for this phase has long discouraged investigators from using the readings for anything more than an approximate check on P'P' times. A partial explanation for this scatter is asymmetric P'P' which arrives earlier than the symmetrically reflected phases, but at least some of the difficulty lies in assignment of the incorrect P'P' branch to a reading and in assumption of the incorrect velocity structure at the reflection point. These problems are avoided and the analysis suggests that one-way travel of P waves through oceanic mantle is delayed by 0.65 to 0.95 sec relative to United States mid-continental mantle.

American Geophysical Union, Fifth-Fifth Annual Meeting, April 8-12, 1974, Washington, D.C.

Kanamori, H. and Cipar, J.J., "Focal Process of the 1960 Chilean Earthquake."

Long-period seismograms recorded at Pasadena are used to determine the focal process of the 1960 Chilean earthquake. Synthetic seismograms computed for various fault models are matched with the observed strain seismograms to determine the fault parameters. A low-angle thrust model with rupture length of 800 km and rupture velocity of 3.5 km/sec is consistent with the observed Rayleigh to Love wave ratio and the radiation assymmetry. A seismic moment of 1 to 3 x 10^{30} dyne cm, the largest ever reported, is obtained over a period range from 200 to 300 sec. This value together with the estimated fault area of about 2 x 10^{5} km^{2} fits into the recently established moment vs. fault area systematics. The excitation efficiency seems to increase with the period. The strain seismogram clearly shown unusually long-period (300 to 600 sec) wave arriving at the P time of a large foreshock which occurred 15 minutes before the main shock, suggesting a large slow deformation in the epicentral area prior to the major failure; the entire focal process may be envisaged in terms of a large-scale deformation which started rather gradually and eventually triggered the foreshocks and the "main" shock. This mechanism may explain the large premonitory deformations decumented, but not recorded instrumentally, for several Japanese earthquakes.

Alewine, R.W. III, "Application of a Least-Squares Inversion Technique to Surface Wave Spectra to Determine Source Parameters of a Finite Source."

A linear inversion scheme is presented to fit in a least-squares sense discretized surface wave spectra. With this technique, an estimate of the uncertainty in the predicted source model is given when errors in the observed data are considered. An earthquake source is represented by a series of double couples which can be offset both spatially and temporally to approximate a moving rupture. A comparison of this representation of a moving source and that classically representing a finite source is given. The inversion scheme yields the source parameters (moment and slip angle)

for the individual double couples as well as rupture velocity. Rayleigh wave spectra from a suite of stations recording the 1971 San Fernando, California earthquake are examined and the resolvability of the inverted source parameters are discussed.

III. Least-Squares Inversion of Surface Above Spectra to Obtain Source Parameters: The 1971 San Fernando Earthquake

This section is Chapter 5 and Appendices 3 and 4 of Ralph Wilson Alewine's thesis (1974) titled "Application of Linear Inversion Theory Toward the Estimation of Seismic Source Parameters". References and details cited in this section can be found in the thesis. This Thesis has been submitted and successfully defended as partial fulfillment of the requirements of the Degree of Doctor of Philosophy at the California Institute of Technology, Pasadena, California.

Chapter 5

Least-Squares Inversion of Surface Wave Spectra to Obtain Source Parameters: The 1971 San Fernando Earthquake

5.1 Introduction.

In this chapter, we will examine the spatial and frequency distribution of Rayleigh waves from the 1971 San Fernando, California, earthquake and how this distribution is related to the faulting processes of that event. The use of surface waves to determine gross source parameters has been a common tool in recent seismological investigations, e.g. Wu (1968), Tsai and Aki (1970, 1971), Canitez and Toksöz (1971, 1972), and Mitchell (1973). Unfortunately, the problem of systematically finding values of the source variables which optimally fit the observed data has not yet received the attention due the problem. With the exception of a Monte Carlo technique by Tsai (1972) and an iterative technique by Turnbull et al. (1973), the "trial and error" method was usually employed in finding suitable variables which describe the data.

We hope to extend the usefulness of surface observations by showing how an inversion procedure can be applied to surface wave observations in order to see what information can and cannot be gained about the earthquake source.

Along with this inversion, we will use a method of expressing the finiteness of the fault plane by numerically summing point source solutions. This method will allow for the variation of parameters over the fault surface. Finally, we would like to compare the solution that we obtained for the San Fernando source mechanism from the static study in the previous chapter to that obtained by the dynamical surface waves.

5.2 Theoretical Model.

Spectra from a Point Source. Theoretical surface wave spectra will be computed for a source in a multilayered medium which approximates the San Fernando area. The elastic parameters for this medium are given in Appendix 5. Far-field amplitude spectra depend on the surface wave amplitude response of the layered medium and also the source type, depth and orientation. Expressions for the frequency dependent media response factor, which is dependent of the source, are given by Harkrider (1964). Computation of this factor involves use of the Thomson-Haskell matrices for the multilayered half-space (Haskell, 1953). The formulation for the component of the surface wave spectra which is due to different source types and the orientation of the source was developed by Ben-Menahem and Harkrider (1964). The far-field solution for Rayleigh wave

spectra for a point double-couple can be written as

$$A(\omega) = \frac{S(\omega)\ k\ A_R\ \chi(\theta,h)e^{-i(kr+\frac{3\pi}{4})}}{\sqrt{kr}} \quad , \qquad (5.1)$$

where

$S(\omega)$ = transformed spectral source function

k = Rayleigh wave wave number

A_R = medium response factor

r = radial distance to receiver

$\chi(\theta,h)$ = complex radiation pattern function, where θ is the azimuth of the station relative to the source and h is the source depth.

The radiation pattern function is given by Ben-Menahem and Harkrider (1964) and by Harkrider (1970). This function is dependent on the source parameters and the source depth. At a given depth, this azimuth dependent function is characterized by the slip, or rake, angle and the dip of the source-equivalent fault. The numerical techniques used in the computer programs which calculate these functions are discussed by Harkrider (1970).

The source function is assumed to be a step function in moment. This is given by

$$S(t) = \begin{cases} 0 & \text{for } t < 0 \\ M_0 & \text{for } t > 0 \end{cases} \quad , \qquad (5.2)$$

where t is the origin time of the event.

Source Finiteness Effects. In the above discussion, the source was represented by a point source. However, if the dislocation on the actual fault surface initiates at one point and propagates to another point, the fault finiteness and rupture velocity can become important. Ben-Menahem (1961) has shown how the dimensions of the source and the speed of rupture play an important role in the resulting spectral radiation patterns. This author shows that spectra from a source which radiates energy evenly as propagation occurs was modulated by the shift factor,

$$\frac{\sin (X)}{X} \; e^{iX} \quad , \tag{5.3}$$

where

$$X = \frac{\omega \, b}{2C} \left[\frac{C}{v} - \cos(\beta_0)\right] .$$

The following parameters are defined:

ω = angular frequency

C = Rayleigh wave phase velocity

b = horizontal rupture length

v = horizontal rupture velocity

β_0 = angle measured from the direction of rupture.

However, if the source radiates energy unevenly during propagation, then this simple modulation no longer applies. One such method of uneven radiation can occur by having the dislocation (i.e., moment) vary along the fault. The fact that surface wave excitation is depth dependent means that a fault which has a vertical component of propagation can also give rise to uneven radiation during propagation. The analytic modeling of such rupture would be very difficult for a layered medium, however, we give here a numerical approximation to this phenomena.

Numerical Approximation of a Propagating Fault. In this section, we will present a method of numerically approximating the surface wave spectra due to a propagating rupture. To do this, we will consider the fault to be modeled by a discrete number of double couple sources arranged spatially to reflect the length of a fault. Propagation along the fault occurs by "turning on" each of the sources sequentially at a time given by

$$T_{d_i} = \frac{\Delta_{s_i}}{V_R} \quad ,$$

where Δ_{s_i} is the distance to the ith individual source from some origin and V_R is some rupture, or propagation, velocity that we wish to approximate. The spectra from

each of the sources will have a different phase at some fixed observation point. The total spectra measured at this point will be the complex sum of the individual contributions. The phase delay of the individual propagation sources relative to the initial source taken to occur at the origin is given by

$$\tau_{p_i} = \frac{\hat{R}_i - R_0}{C(\omega)} + T_{d_i} \quad ,$$

where R_0 is the distance from the initial, or reference source, to the exterior observation point and $\hat{R}_i$ are the distances from the other sources to the observation point. $C(\omega)$ is the phase velocity. The geometry of this problem is illustrated in Figure 5.1. From this figure, we can write

$$\hat{R}_i = [d_{s_i}^2 + R_0^2 - 2\, d_{s_i} R_0 \cos(\lambda_R - \theta_F)]^{1/2},$$

where d_{s_i} is the horizontal separation of the individual sources relative to the initial source taken in the direction of rupture, λ_R. θ_F is the "azimuth" to the station relative to the initial source. Appendix 4 goes into the details of how the spectra are summed given this phase information. Both strike slip and dip slip faulting can be approximated with this geometry.

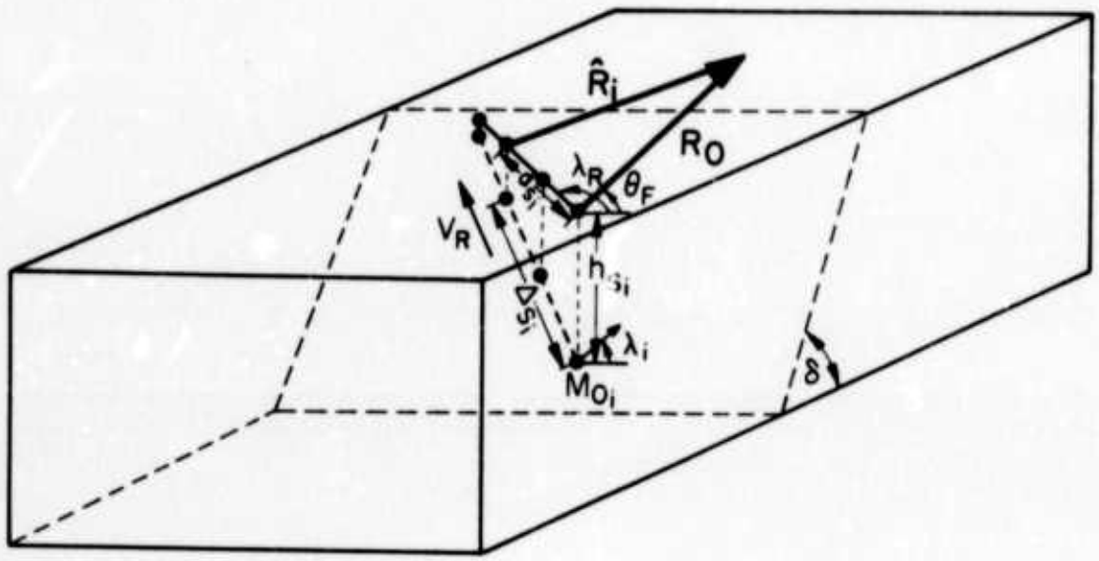

Figure 5.1. Geometry of the assumed multiple double couple source.

We caution here that the angle θ_F as defined in Figure 5.1 is not the same angle as the angle θ in the complex radiation pattern term of equation (5.1). A preliminary examination of Figure 1 in the Ben-Menahem and Harkrider (1964) paper would indicate that these two angles are equivalent, but their definition of θ is in error. The angle θ should be measured positively clockwise from the positive strike direction when viewed above the half-space.

As a check to this numerical approximation, we will model a vertical strike slip earthquake and check the resulting spectra with that calculated by the method of Ben-Menahem (1961). This model consisted of 16 sources, each at a depth of 20 km, with dip 90°, slip angle 0° (pure left lateral faulting), and identical moments. The sources were spaced at 2 km increments along the strike of the origin source (λ_s=180°) so that the fault length and propagation length were 30 km. Spectra were computed for apparent propagation velocities of 1.5, 3.0 and 4.5 km/sec at a point in a direction 45° to the direction of propagation in order to avoid a node in the radiation pattern of strike slip events. These spectra were then compared to that calculated for a single point source with the shift term for this fault length and propagation velocities. The moment of the single source was taken as the simple sum of

the moments in the discretized model. The results are shown in Figure 5.2.

In this figure, we have normalized the amplitudes to the values calculated for a non-propagating point source at the depth of the source at the point of initial rupture. By utilizing this normalization, we cancel the media source depth effects on the spectra. The ratio shows only the effects of the fault finiteness. In Figure 5.2a, we see that the directivity calculated by this numerical technique matches very closely that given by Ben-Menahem (1961). For propagation velocities 3.0 km/sec and greater, there is less than 1% difference in the two calculations. We see that the directivity is a very pronounced function in the period range of interest for slow propagation velocities.

Now that we have shown that the directivity function can be accurately calculated numerically, we now examine the effect of dip slip propagation on surface wave amplitude spectra. A model of a 45° pure dip slip fault was constructed. The initial motion occurs at a depth of 20 km and propagates at a constant velocity up the fault to a depth of 2 km. A total of 10 double couple sources were spaced at a 2 km depth and lateral increments to approximate this fault. The propagation distance along the fault is 28.3 km, and the pure horizontal propagation distance is

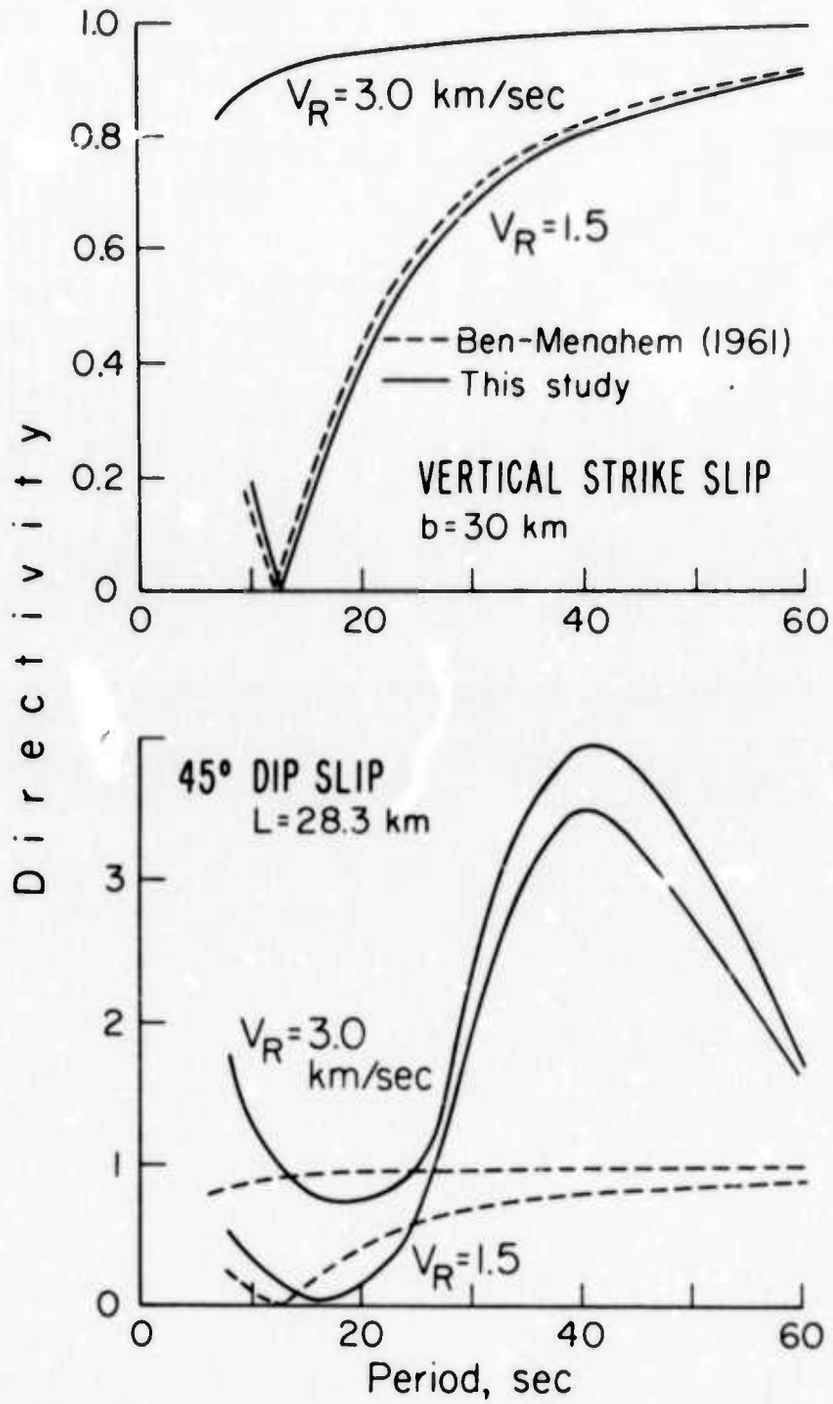

Figure 5.2. Comparison of the frequency-dependent directivity function given by the Ben-Menahem formulation and the numerical approximation. Upper--results for a 30 km long left lateral strike slip fault. Lower--results for a 28.3 km wide 45° dip slip fault.

18 km. The spectra were calculated at an exterior point which is in the direction of propagation. Spectra were also calculated using the Ben-Menahem formulism for the same parameters. All the amplitudes were normalized to a non-propagating point source at a depth of 20 km. Figure 5.2b shows a comparison of the resulting directivities for this dip slip case.

We see in this figure that there is a vast difference in the spectra computed by the two methods. The most significant difference is the accentuation of the amplitudes in the 25-60 sec period range. As a check as to whether the large amplitudes calculated in the numerical case were due to a Doppler effect or due to the non-uniform depth excitation along the propagation length, we normalized these amplitudes to the spectrum which was calculated using the numerical approach when an infinite propagation velocity was used. This normalization cancels any non-uniform depth excitation since the depth distribution was identical in both cases. The resulting directivity was almost identical to that calculated by the Ben-Menahem method and shown in the lower part of the figure.

We thus conclude that the effect of a source radiating energy as it propagates from one depth to another during faulting can be much larger than the Doppler effect and

cannot be ignored when spectra due to this type of faulting are being modeled. The depth effect on the spectra will vary from medium to medium and from source type to source type. No attempt was made here to catalogue this effect for various media and propagation parameters.

Approximation of San Fernando Faulting. In the previous chapter, we discussed the geophysical observations which constrained the fault model geometry for the 1971 San Fernando, California, earthquake. In this chapter, we would like to adopt an approximation to this same geometry to try to explain the radiation of surface wave energy from this fault. This approximation is accomplished by using four double-couple sources. The primary constraint for limiting the approximation to only four sources was economic, since the forward problem had to be recalculated after each iteration for the partial derivative matrix. However, we consider that the approximation chosen is adequate in light of the periods of the surface waves used. The parameters which describe this fault geometry and remain fixed in the inversion are listed below.

Source No.	depth(km)	dip	d_s(km)
1	14.5	52°	0.0
2	10.5	52°	2.49
3	6.25	35°	7.51
4	2.00	35°	14.36

These loci of the four point sources do not lie on a straight depth-distance line, but rather define the center line of a fault plane whose dip increases with depth. In calculating the propagation delay time for each of the elements, the distance, Δ_i, is used. Δ_i is given by

$$\Delta_i^2 = (h_{s_i} - h_{s_1})^2 + d_{s_i}^2 .$$

These distances are the straight line distances from the initial source to the three other double-couples. The delay time error caused by using this distance rather than the distance measured along the curved "fault plane" is less than 1 sec in the extreme case.

5.3 Forward Problem Formulation.

In this section, we wish to pose a relationship between the source model parameters and the observed spectra in a linear form as in equation (2.3). As we did for the static problem, we will propose some fault geometry and use an inversion scheme to solve the fault model parameters for this geometry. In order to describe the data, we will use a set of double-couple sources that are arranged spatially to approximate the fault model system which was presented in the previous chapter. Some of the parameters of the individual sources, specifically those which

describe the geometry of the fault system, will be set initially and not changed in the inversion. These parameters are the depth and dip associated with individual source elements and the spatial relationship between elements. The variable parameters for each element are taken to be the moment and slip angle. In addition, we will include the propagation velocity and propagation direction as variables for the entire system.

The model response matrix, **A**, for this problem is given to be composed of partial derivatives of the form

$$\frac{\partial S_i}{\partial X_k} \quad , \tag{5.4}$$

where S_i is the spectral amplitude value at some frequency f_ℓ (ℓ=1,L) measured at some "azimuth" θ_{F_j} (j=1,J) with respect to the fault system. X_k (k=1,K) is the source parameter which is allowed to be varied. The matrix **A** has K columns and L x J rows, where K is the number of model variables (specified below), L is the number of discrete spectral points at a single station and J is the number of stations used. For this case, L=10, J=18, K=10.

We see from Appendix 4 that the addition of multiple sources is a non-linear operation. This problem can be overcome by mapping only small increments of the model into

changes in the data. The criterion for this linearization is the same as was discussed in Chapter 2. The partial derivatives which compose the matrix **A** were computed numerically for a given model. This was done by the simple differencing,

$$\left.\frac{\partial S_i}{\partial X_k}\right]_m \approx \frac{S_i(m+\Delta m_k) - S_i(m)}{\Delta m_k} . \qquad (5.5)$$

The incremental values of the source parameters used were:

M_0 - moment = 0.1×10^{26} dyne-cm

$\Delta\lambda$ - slip angle = 10°

$\Delta\lambda_R$ - propagation direction = 10°

ΔV_R - propagation velocity = 0.25 km/sec .

5.4 Inversion Procedure.

An inversion procedure will be adopted to find the model parameters which best fit the observed spectral data. Since the number of data points far exceed the number of variables, we will fit the data in a least-squares sense. Appendix 3 gives the derivation of the inversion operators for the general least-squares case.

Since we have mixed units in the source model parameters and thus mixed units in **A** and $\delta\mathbf{m}$, a problem of

scaling arises. One way of correcting for the dimensionality of the parameters is through the use of the weighting, or model correlation, coefficients. The weights of the source parameters can be adjusted so that the weighted coefficients of the rows of **A** are about equal. For a non-linear problem, this scaling would be model dependent and thus would probably vary in the inversion. This method, although it can give satisfactory results in obtaining a fit to the data, is not esthetically pleasing. A satisfactory method was found to solve this scaling problem. This was accomplished by non-dimensionalizing the problem,

$$\mathbf{A}\,\delta\mathbf{m} = \delta\mathbf{d} \quad ,$$

by dividing through by the data and model parameters. The dimensional matrices and vectors are replaced by their non-dimensional counterparts in the inversion. The components of the quantities are defined as:

$$\hat{A}_{ij} = \frac{m_j}{d_{o_i}} A_{ij} \qquad \delta\hat{d}_i = \frac{1}{d_{o_i}} \delta d_i$$

$$\hat{C}_{nn_{ii}} = \frac{1}{d^2_{o_i}} C_{nn_{ii}} \qquad \delta\hat{m}_j = \frac{1}{m_j} \delta m_j \quad .$$

We note that this scaling is also non-linear.

Throughout the inversion calculations carried out in this chapter, we will limit the absolute value of a model perturbation in one iteration to that used in the differencing method of calculating the partial derivatives in the forward problem. This was done to avoid projecting any model perturbation outside the range of assumed linearity.

As a test to the inversion scheme, we will calculate the theoretical spectra at 18 far-field points (corresponding to the location of the 18 stations which are described in the next section) for a given set of source parameters. The non-variable source parameters are the same as those used to describe the San Fernando faulting. These theoretical spectra were then input into the inversion scheme as "data" to see how accurately the corresponding variable source parameters could be recovered. The results of this test are shown in Figure 5.3. The initial values for the source parameters are that shown on the left at Iteration = 0. The source values used in calculating the "data" are shown by the arrows on the right hand side of the figure. We see that at least 6 iterations are required before the solution starts to converge to the true values, and after 11 iterations, the estimated values are very close to the true values. The restriction that the maximum size of the perturbations can be no larger than the differencing

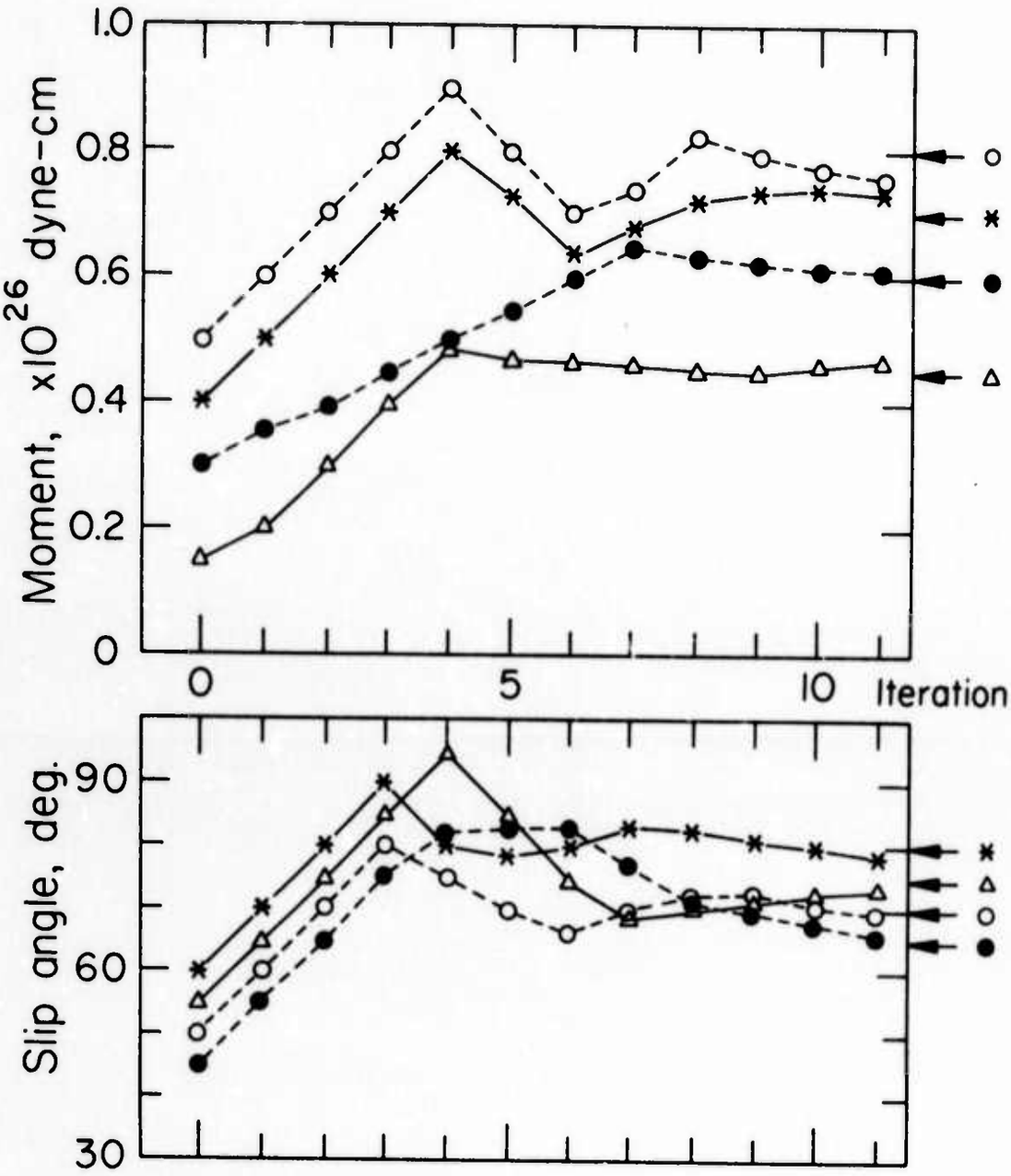

Figure 5.3. Test to check the amplitude spectra inversion technique. Initial values of the fault parameters are shown on the left; the theoretical values are indicated by arrows on the right.

values slows the convergence somewhat. Not shown in this figure is the estimate of the propagation velocity and propagation direction for each iteration. These two quantities varied more smoothly and converged more quickly to the theoretical values than did the moments and slip angles. The propagation velocity and propagation direction converged to 4.2 km/sec and 120° from an initial value of 3.2 km/sec and 100°, respectively.

In this test, the variance of each "datum" was taken to be 5% of the calculated value. The test was repeated with the data variances set at 25% of the calculated values. Although the convergence to the true model values was not as good as in the previous example, the solution remained stable through the iterations, and a fair estimate of the model parameters was obtained. The results from these experiments were encouraging enough to attempt to apply the technique to actual observed surface wave spectra.

5.5 Data.

The source of the surface wave data used in this study was from the long period vertical component instruments of the World-Wide Standard Seismograph Network (WWSSN). Only the vertical Rayleigh wave component at each station was considered in this study. Data from the Canadian Standard Stations and the WWSSN stations located in the continental

United States could not be used since either the long period vertical component was inoperative or off-scale during the passage of the Rayleigh wave train. The original intent in collecting this data was to limit the stations used to those whose epicentral distances were less than 60°-70°. However, to provide a more uniform and extensive azimuthal coverage of stations, this condition was relaxed somewhat. The closest station in a given azimuthal increment from the epicenter which gave a readable record was chosen. A total of 18 records was chosen to be examined, and these stations provided a fairly good azimuthal coverage for this event. Table 5.1 gives a list of all these stations used, the epicentral distances, and the geodetic azimuth of the station with respect to the epicenter.

The Rayleigh wave signal was identified on each of the records and digitized at an irregular interval taking adequate care to sufficiently define the trace. These data were then linearly interpolated to an equal increment rate of one sample every two seconds. The digitization was restricted to a velocity window of between about 4.3 km/sec to about 1.5 km/sec. There was a slight variance to this window depending on the distance and source-receiver path. The choice of the velocity window was based on a visual judgment as to when the signal arrived and essentially

TABLE 5.1

Station	Geodetic Azimuth	Distance (Deg)	% Land	% Ocean	Geom. Fact.	Geographic Location
NOR	10	58	90	10	1.66	Nord, Greenland
KTG	23	60	77	23	1.68	Kap Tobin, Greenland
AKU	27	63	75	25	1.70	Akureyri, Iceland
VAL	38	74	55	45	1.76	Valentia, Ireland
MAL	47	86	61	39	1.80	Malaga, Spain
BEC	77	45	78	22	1.51	Bermuda
SJG	96	49	69	31	1.56	San Juan, Puerto Rico
CAR	104	53	43	57	1.61	Caracas, Venezuela
BHP	116	44	70	30	1.50	Balboa Heights, Canal Zone
GIE	137	44	11	89	1.50	Galapagos Islands
PEL	141	81	16	84	1.79	Peldehue, Chile
SBA	194	120	0	100	1.67	Scott Base, Antarctica
WEL	224	97	0	100	1.79	Wellington, New Zealand
AFI	236	70	0	100	1.74	Afiamalu, Samoa
KIP	260	38	0	100	1.41	Kipapa, Hawaii
GUA	285	88	0	100	1.80	Guam Island
MAT	307	80	1	99	1.79	Matsushiro, Japan
COL	339	35	69	31	1.36	College, Alaska

Table 5.1. Stations used in this surface wave study.

ended at a particular station and on the dispersion curves expected for the traveled path. Typical of the dispersion curves used were those of Brune and Dorman (1963), McEvilly (1964), Santo (1963), Tryggvason (1962), and Brune (1969).

The Fourier spectra of these records were then taken with a numerical transform routine. The spectra were calculated for the frequency range from 60 sec period to 8 sec period, with 512 discrete frequency points in this range. The spectra were smoothed slightly with a two-point Hanning filter such that for the ith frequency component of a particular record

$$f_i(\omega) = \frac{2}{5}\left\{\frac{1}{4}[f_{i-2}(\omega)+f_{i+2}(\omega)]+\frac{1}{2}[f_{i-1}(\omega)+f_{i+1}(\omega)]+f_i(\omega)\right\} .$$

Instrument Correction. The instrument frequency and amplitude response for the World-Wide long period seismograph system were calculated from the published instrument and coupling constants for that instrument. These calculations are based on the relations given by Hagiwara (1958) and Mitchell and Landisman (1969). Both an amplitude and frequency correction were supplied. Since some of the stations that were used in this study operate at different instrument gains during different parts of the year, a check was made on each seismogram to verify the listed

instrument gain. This was done by comparing the height of the calibration pulse to the applied current impulse. The magnification computed in this fashion was within about 10% of the listed magnification except for station SBA which appeared to be off by a factor of 2.

Geometrical Spreading Correction. All of the amplitude spectra $A(\omega)$ are corrected back to a common distance, Δ_c, by multiplying by the well-known relation for spreading on the surface of a sphere

$$C_{GS} = \sqrt{\frac{\sin \Delta}{\sin \Delta_c}} \quad , \tag{5.6}$$

where Δ and Δ_c are given in radians. For the data in this case, we chose our reference distance, Δ_c, to be 2000 km.

Attenuation Correction. Following the instrumental and geometrical spreading corrections, the spectral amplitudes were corrected for attenuation. This correction takes the form

$$A_c(\omega) = A(\omega)\, e^{\gamma(\omega)\, x} \quad , \tag{5.7}$$

where $\gamma(\omega)$ is the amplitude attenuation coefficient appropriate for the particular source to receiver path, and x is the epicentral distance. Since the paths from the San Fernando epicenter to most of the WWSSN stations used in

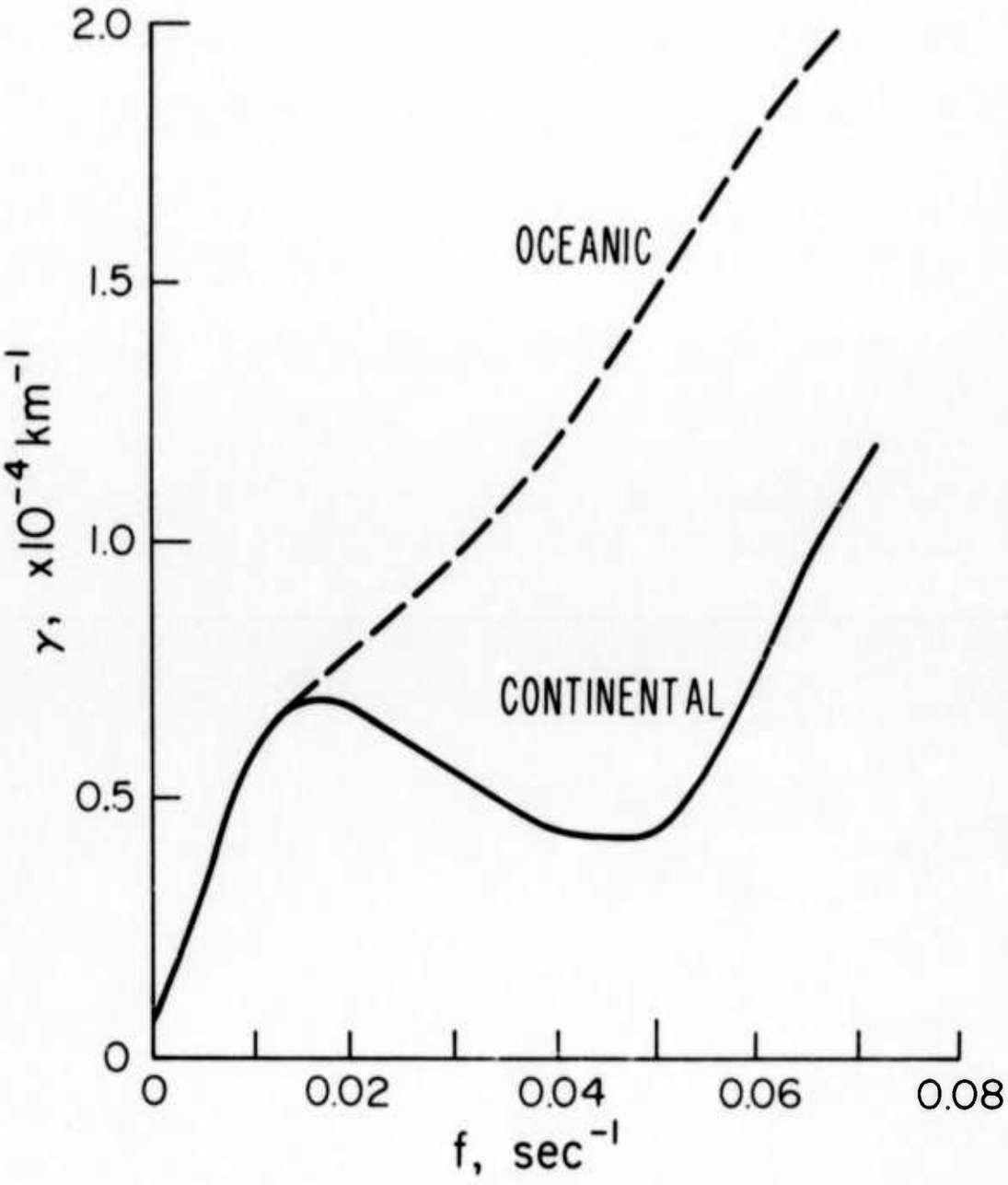

Figure 5.4. Amplitude attenuation coefficients assumed for the two structures used in this study.

this study involve mixed crustal type paths, the appropriate attenuation coefficient would necessarily be a path-averaged value. We attempted to take this into consideration in the following manner.

We assume that each of the transmission paths can be divided into two types: continental and oceanic. From the literature, we compiled estimates of the fundamental model Rayleigh wave attenuation coefficients for these two media. These estimates are summarized in Figure 5.4. The continental attenuation coefficients are reduced from data given by Gutenberg (1945), Gutenberg and Richter (1936), Tryggvason (1965), Nuttli (1973) and Mitchell (1973). The oceanic attenuation coefficient curve was reduced from data in papers by Gutenberg (1945), Ben-Menahem (1965), and Tsai and Aki (1969). The partitioning of continental and oceanic travel paths was estimated for each station, and the spectral amplitudes measured at that station were corrected by multiplying by the following relation,

$$C_A = e^{[x_L \gamma_L(\omega) + x_O \gamma_O(\omega)]}, \qquad (5.8)$$

where

$\gamma_L(\omega)$ = the continental, or land, amplitude dissipation coefficient

$\gamma_o(\omega)$ = the oceanic amplitude dissipation coefficient

x_L = the distance traveled over a continental type path

x_o = the distance traveled over an oceanic type path.

Table 5.1 lists the percentage of the total path length that is spent in each of the assumed attenuation provinces. Also listed in this table is the geometrical spreading factor given by the equation in the above paragraph.

Local Crustal Correction. This correction attempts to compensate for the effects of surface waves traveling laterally from one structure to another. In the case under consideration, there are marked variations in the structure of the crust and upper mantle between the area in which the surface waves were generated and the area around the stations at which they are measured. Fortunately, the corrections applied along the path between these two points cancel out so that only a local crustal correction at the receiver needs to be applied to correct the spectral amplitudes back to the medium in which they were generated. An approximation which has given satisfactory results in predicting the amplitude changes of Rayleigh waves traveling across a lateral boundary has been given by McGarr (1969) and McGarr and Alsop (1967). The validity of this

approximation has been verified by wave propagation studies in laterally heterogenous media using the finite-difference numerical technique (D. Boore, personal communication, 1974).

If we assume that the total energy in the fundamental mode Rayleigh wave remains constant in the process of transmissions across the boundary margin, then we can write

$$\frac{A_R}{A_S} = \sqrt{\frac{W_S(\omega)}{W_R(\omega)}} \quad ,$$

where

$A_S(\omega)$ = the amplitude in the source medium

$A_R(\omega)$ = the amplitude in the receiver medium

$W_S(\omega)$ = the normalized energy flux in the source medium

$W_R(\omega)$ = the normalized energy flux in the receiver medium.

The normalized energy flux is given by

$$W(\omega) = 2\ E(\omega)\ U(\omega) \ ,$$

where $E(\omega)$ is the total potential or kinetic energy at a particular frequency normalized to the surface displacement. The calculation of this energy excited in a given layered earth model is given by Harkrider and Anderson

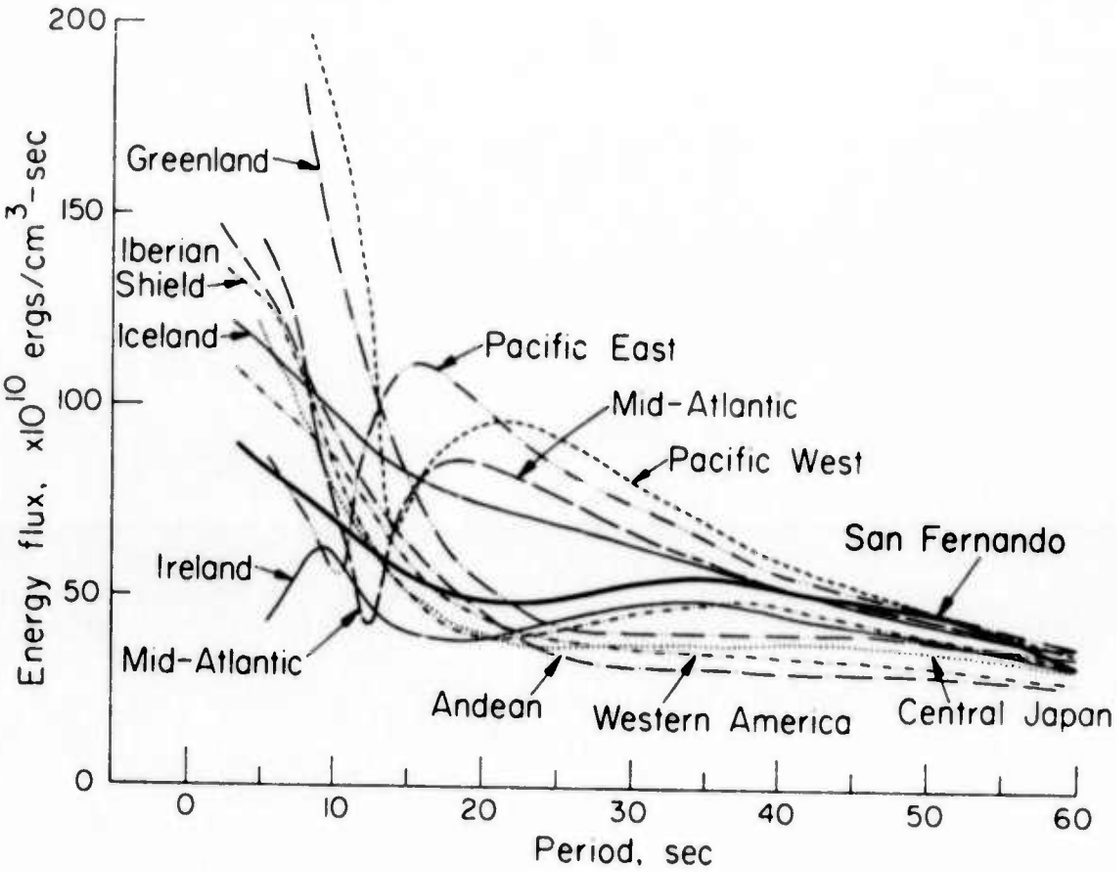

Figure 5.5. Energy flux as a function of frequency calculated for various crustal and upper-mantle models. The velocity-density structures for the various models are given in Appendix 5.

TABLE 5.2

Crust & Upper Mantle Type		Station
San Fernando Crust over Gutenberg Continent	-	Source Medium
Greenlandic Shield with Ice Cap	-	NOR, KTG, SBA
Iceland	-	AKU
Irish Continental Shelf	-	VAL
Iberian Shield	-	MAL
Mid-Atlantic Ocean	-	BEC, SJG
Western America Tectonic	-	CAR, BHP, COL
Pacific Ocean East	-	GIE
Pacific Ocean West	-	AFI, KIP, GUA, WEL
Andean	-	PEL
Central Japan	-	MAT

Table 5.2. Crust and upper mantle structure used for the local crustal structure spectral amplitude correction. Velocity-density models for the different structures are given in Appendix 5.

(1966, equation 1). $U(\omega)$ is the group velocity for the particular medium.

At each of the 18 WWSSN stations used in this study, the crustal structure at that station was approximated and the velocity dispersion and the spectral energy density calculated. The crustal models used in this calculation and the references for these models are given in Appendix 5. The energy flux, $W(\omega)$, given by these calculations is summarized in Figure 5.5. The stations for which each crustal model correction was used are listed in Table 5.2.

In order to correct the spectral amplitudes back to a common medium, we multiply by a correction which normalizes the amplitudes to the source medium. This correction takes the form

$$C_{LC} = \sqrt{\frac{W_R(\omega)}{W_S(\omega)}} \quad . \tag{5.9}$$

Multipath Propagation Removal. The complex cepstrum technique which was established by Schafer (1969) has proven to be an effective means of removing spectral modulations caused by the interference of simultaneously arriving signals. Two or more signals can arrive simultaneously at a given station due to either multipathing of a single signal or can result from the addition of several seismic

signals, multisourcing, or some combination of these two effects. In this study, we want to eliminate as best we can from our observed spectra that modulation which is due to any multipathing effects and retain any modulations which may arise from the addition of multiple sources. The spectra which have been de-modulated from multipathing effects can then be examined by this method to try to determine the existence of whether the source is a single or multiple event.

Cohen (1970) and Flinn et al. (1973) have used the technique to detect the separation of the body phases P and pP for very shallow events, while Linville (1971) and Tsai (1972) have applied the method to surface waves. In the cepstrum technique, a homomorphic deconvolution is applied to separate the components of a convolution of a seismic signal and a multipath operator. Basically, the method acts like a filter applied to the amplitude spectra where the interferrence effect appears as a scalloping of the spectra over a wide frequency range. When a long pass filter is applied, the spectrum modulating effects are removed. This filtering is done by applying the appropriate bandpass to the cepstrum. Tsai (1972) and Linville (1971) give a summary of the technique involved and the appropriate filter bands to use in correcting spectra in the

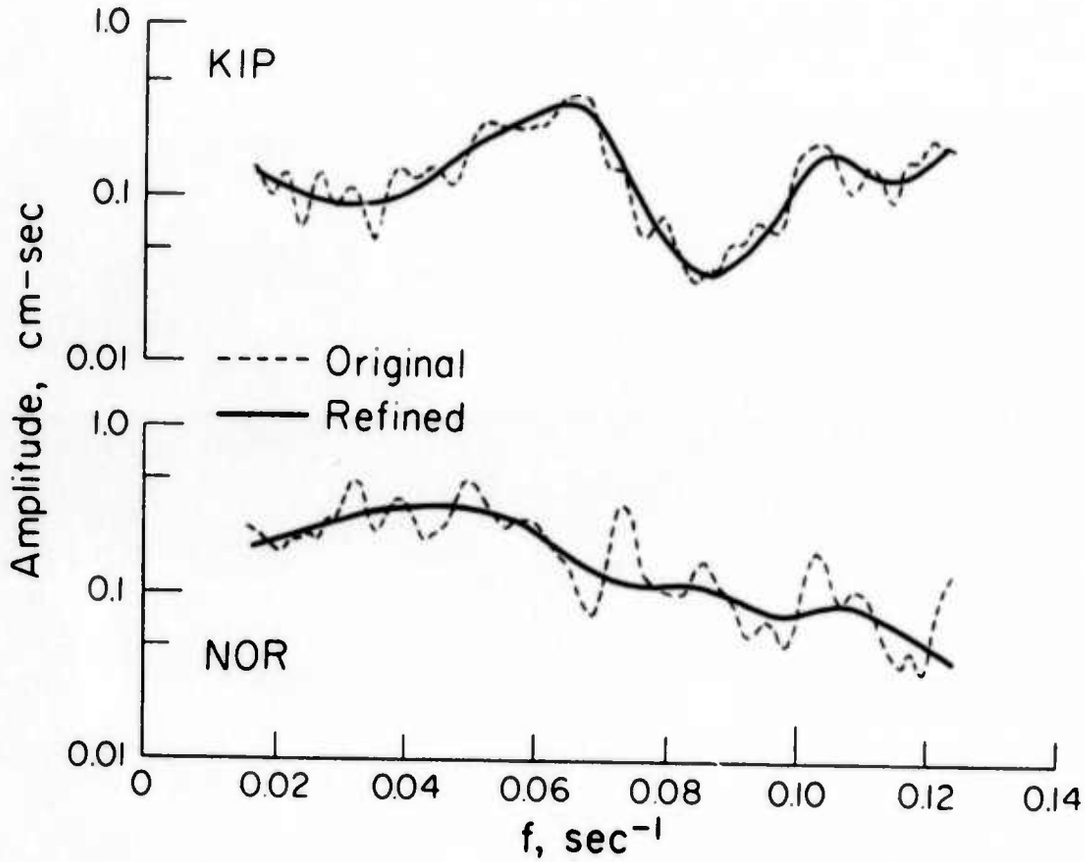

Figure 5.6. Example of cepstral filtering at two stations. Original spectra are shown by dashed line; the refined, or filtered, spectra are shown by the solid line.

bandwidth which is involved in this study. Such a long pass filter was applied to the observed spectra. This spectral filtering had little effect except to smooth the spectra. A typical example of the removal of the spectral modulations is shown in Figure 5.6. The spectra are presented as a function of frequency to show how the modulations are frequency distributed. In this figure, the original spectra are shown by the dashed line, and the spectra after the application of the cepstrum technique are shown as a solid line.

We saw in the last chapter from the static dislocation models of the San Fernando earthquake that there appeared to be two areas of large dislocation -- one in the hypocentral region and one near the surface. If the dislocations from these two areas acted like two separate sources, separated spatially and temporally, then the interference of these two sources should appear in the complex cepstrum. The cepstra were calculated at several of the stations chosen in the opposite direction of the apparent rupture. This was done to maximize the effect of the final separateness of the sources. At station COL, there appeared to be some signal interference at a delay time of about 8 sec and at 11.5 sec. This might be interpreted as the interference of the signal excited at the hypocenter by another

signal which was excited when the fault became near or broke the surface. This effect was not as apparent at station NOR, so we feel that no firm conclusions should be drawn from this particular analysis.

Corrected Data. All of the above corrections were applied to the measured amplitude spectra at the WWSSN stations. These spectra are shown in Figure 5.7. The upper part of this figure shows the location and azimuthal distribution of the stations used. The lower part of the figure gives the corrected amplitude spectra at each of the stations. The spectra are arranged by columns with geodetic azimuth increasing from top to bottom. The spectral values indicated by a dashed line in the figure are the values for which the total correction exceeded a factor of 10. These data will have to be considered less reliable than the longer period data because of the uncertainties in the corrections. Samples of the spectral values were chosen at ten discrete periods: 60, 50, 40, 34, 30, 26, 22, 20, 18, and 16 sec. It was felt that this sampling interval was adequate to reflect the spectra shape at the individual stations. Periods shorter than 16 sec were not included into the inversion data set because of the larger uncertainty in the corrections at these periods, particularly in the attenuation factor.

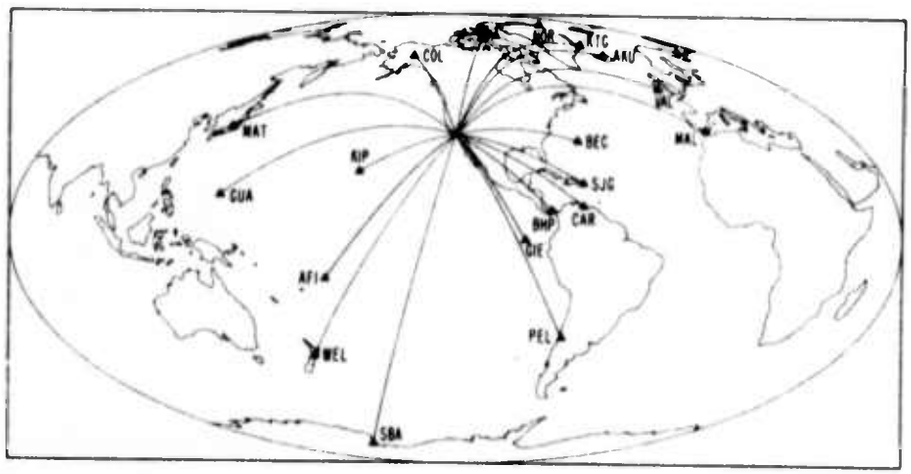

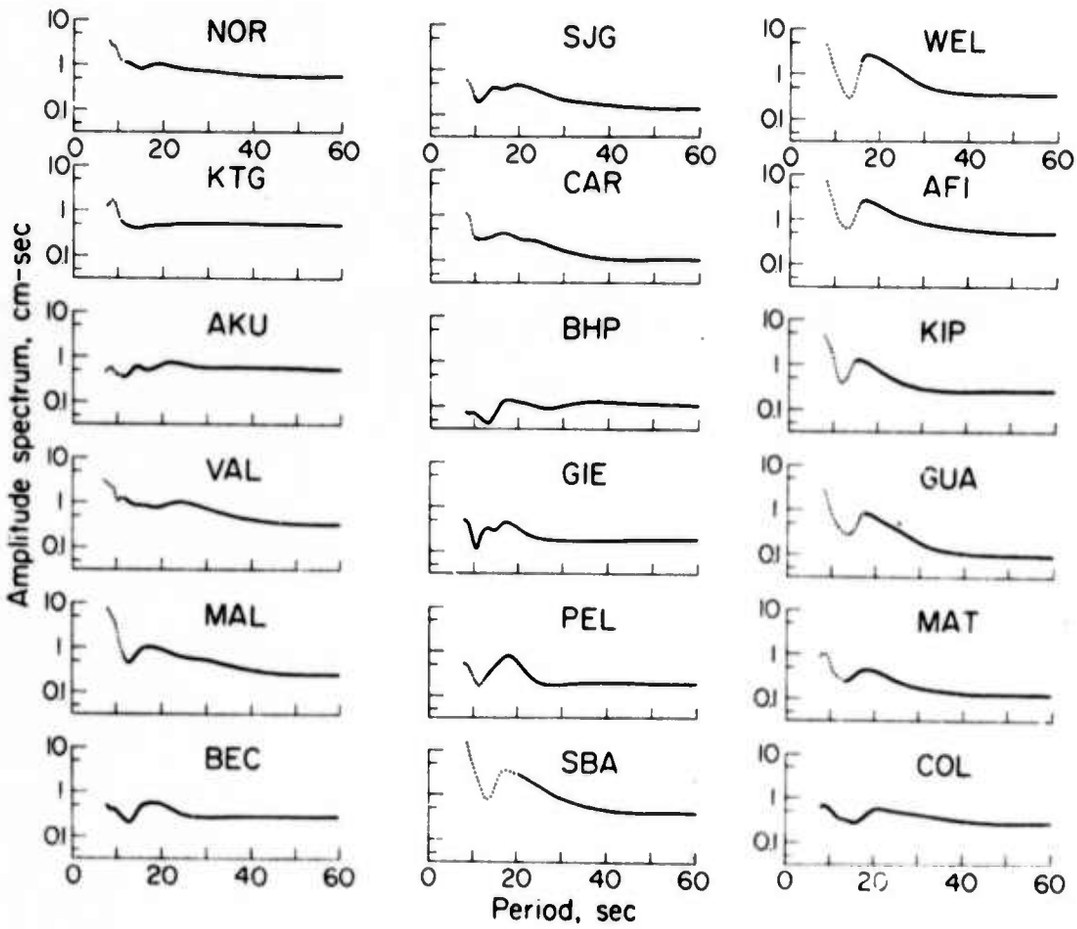

Figure 5.7. Observed spectral amplitudes after all corrections have been applied. Dotted line indicates when the corrections exceed a fator of 10.

Estimated Errors in the Data. Errors to the spectra which we have measured for this event arise from two sources: 1) errors in measuring the spectra at the different stations and 2) errors in applying the corrections to the spectra.

Errors from actually measuring the spectra could arise from digitizing errors and from taking too short a signal to get all the spectral information at certain frequencies. One station, KIP, was redigitized to include a much larger signal and the spectral amplitudes recomputed. The recalculated amplitudes were found to be at most 3-4% different on the average than that originally computed. A value of 3% error was taken as the estimate for this error.

By far, the largest error involved in the application of the spectral corrections arises from the attenuation correction. If we assume that we know the attenuation values to only 25% of the values given in the figure, then the estimated error for this correction would be

$$E_c(\omega) = e^{\frac{\gamma}{4}\Delta}.$$

We next can assume that we know the crustal corrections to only 25%. This turns out to be a small error, except at very short periods, because the original correction is small.

Distribution of Data Information. In Appendix 3, we have derived an operator, **J**, which tells how the information in the data set is distributed. The use of this operator has been demonstrated by Minster et al. (1974), and these authors give a lucid description of its properties. The importance of a particular datum, which is a spectral amplitude at a particular frequency measured at a particular spatial location, depends on both the location and the accuracy of the datum. If we consider each WWSSN station to be a subset of the entire data set, then the relative importance of that station is simply the sum of the importances of the data in that subset. Figure 5.8 shows how the information in the chosen data set is distributed. In this figure, we have summed the relative importances of the frequencies at the individual stations and plotted this importance as a function of the geodetic azimuth of those stations. The results of this plot are somewhat surprising. We see that two stations, COL and KTG, contain a total of 30% of the total information in the data set. In fact, the data set could be reduced by half and only 25% of the total information which constrains the model variables would be lost.

From Appendix 3, we see that the importance of a datum does not depend on the actual value of the datum

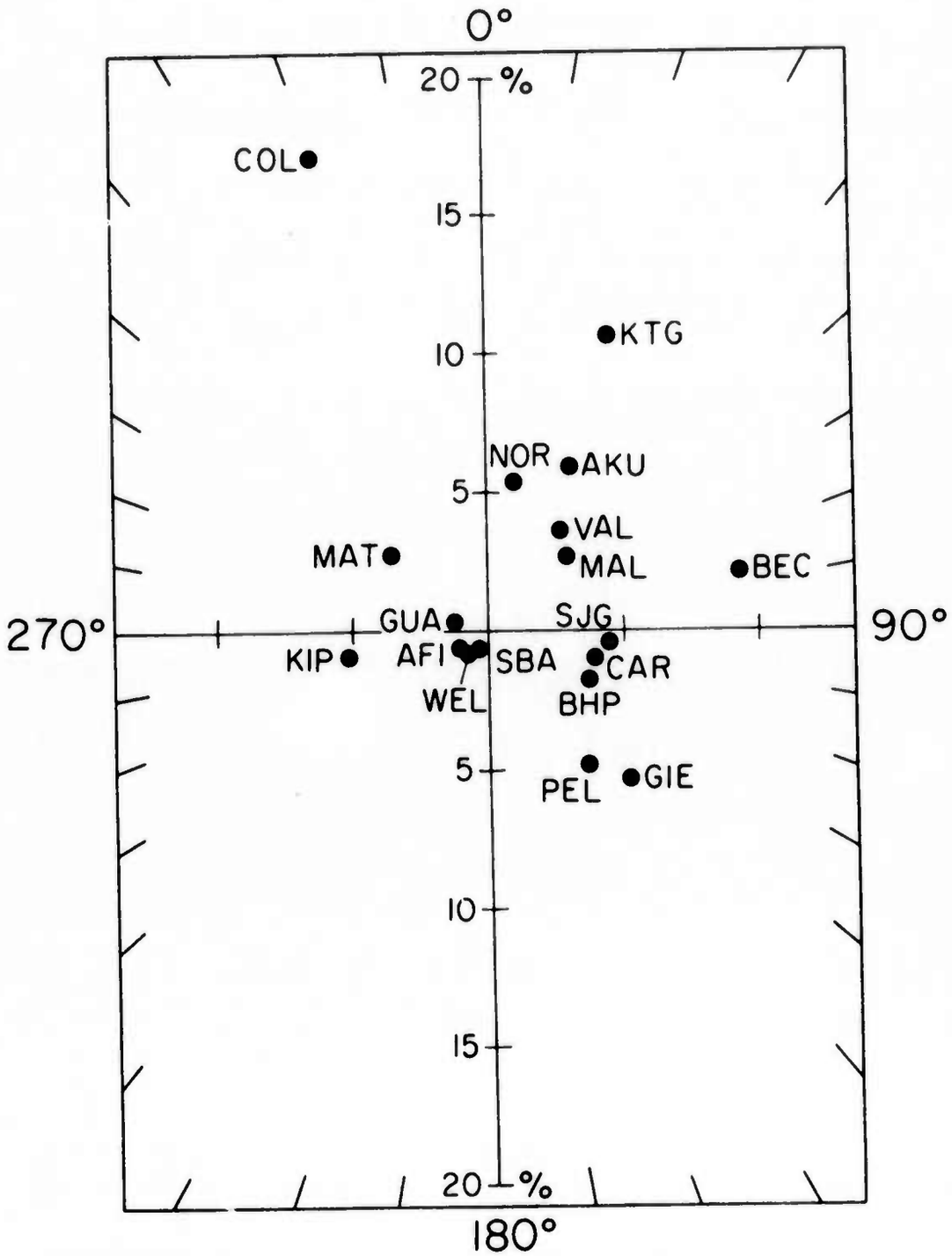

Figure 5.8. Distribution of data information with respect to summed information density at a single station. Information density is normalized such that the total from all stations is 100%.

itself but rather the estimated error in the datum and the model response operator, **A**. The importance values are dependent on the source model only in the sense that **A** is model dependent. Although not done in this case, this type of calculation could be carried out before the data set is gathered to determine an optimum distribution of stations to use.

5.6 Inversion Results.

Fault Model. The ten model parameters which describe the source system were found by the least-squares fit to the observed spectral data measured at the 18 WWSSN stations. The best fit model parameters as determined from the inversion procedure are as follows:

Source #	Depth (km)	Moment (10^{26} dyne-cm)	Slip Angle (λ_1)
1	14.5	0.62	66°
2	10.5	0.20	78°
3	6.25	0.51	82°
4	2.0	0.39	70°

propagation direction (λ_R) = 99°

propagation velocity = 2.95 km/sec.

Figure 5.9 illustrates the degree of fit to the data that this model exhibits. The dashed straight line in the center of each radiation pattern indicates the orientation

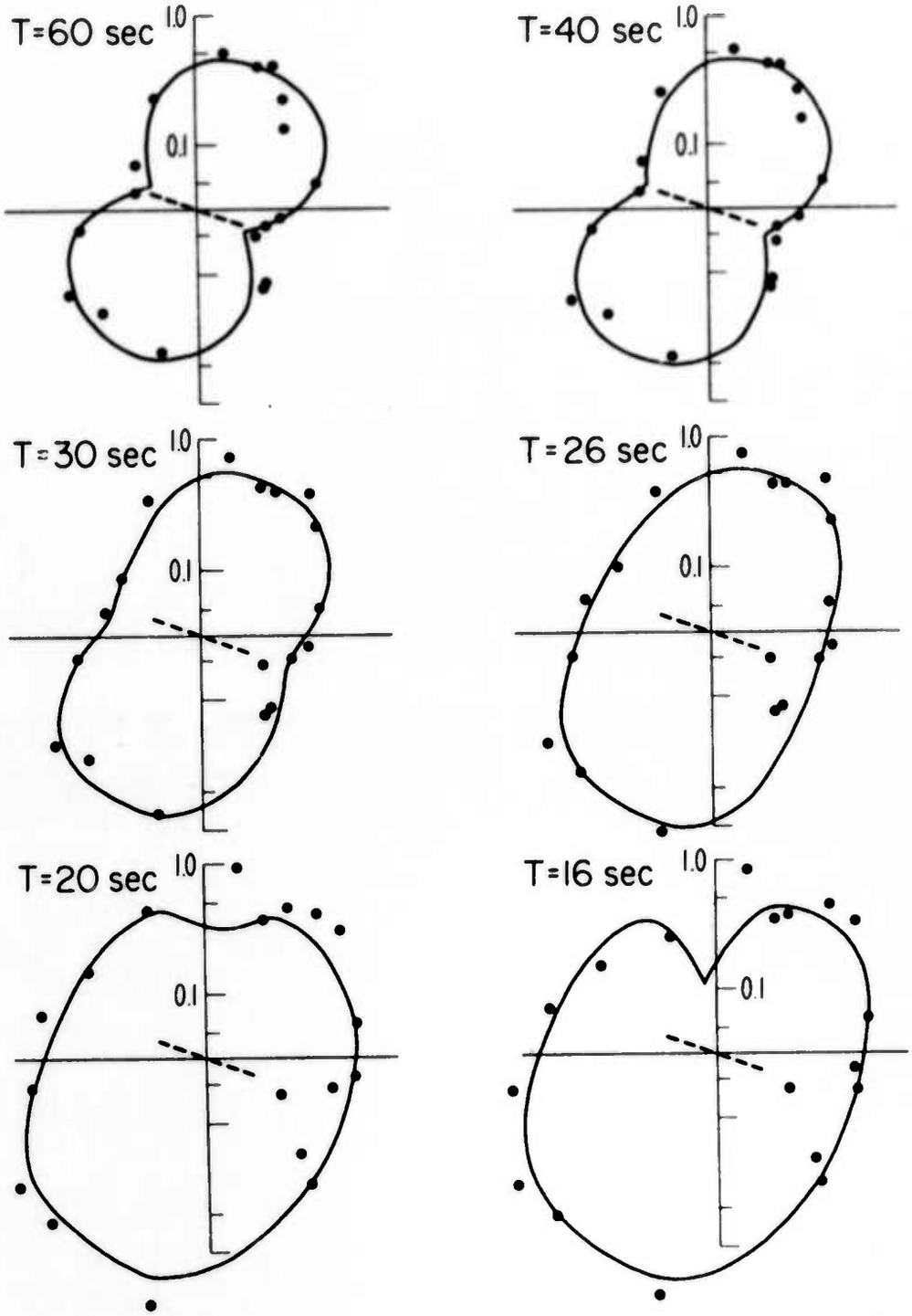

Figure 5.9. Calculated and observed radiation patterns. Orientation of the fault plane (N70°W) is shown by the dashed line in the center of each pattern. The amplitudes of the patterns are in units of cm-sec.

of the strike of the fault system, taken to be in the direction of N70°W. Rupture initiates at a depth of 14.5 km and propagates in the direction of S11°W. The fit to the long period data (40-60 sec) shows that the radiation pattern is a symmetric dipole pattern. These two patterns show very little, if any, signs of fault finiteness. The finiteness of the fault starts to become apparent in the middle two figures. For these periods (26-30 sec), the patterns are symmetric in a direction perpendicular to the direction of propagation but not in the direction of propagation. For the shorter periods (16-20 sec), the effects of the rupture length and non-uniform excitation become very important in shaping the radiation patterns.

Uncertainty in Model. We would now like to estimate the uncertainties in these best fit model parameters. As done in Chapter 2 for the stochastic inverse case, we will calculate these uncertainties at a particular confidence level by mapping the estimated errors in the data into errors in the model. The least-squares solution matrix for unweighted model parameters which performs this mapping is the matrix given by Mathews and Walker (1964, p. 366-367)

$$\mathbf{Q} = \mathbf{A}^{*}\mathbf{C}_{nn}^{-1}\mathbf{A} \quad . \tag{5.10}$$

We note here that this solution does not take into account

the possible weighting of the different model parameters. This is no problem in this case, or in any other case, since the problem can be non-dimensionalized as we have done here. The non-dimensional form of this operator has the same form as that given above.

The bilinear product of the matrix, $\mathbf{Q}$, and some model perturbation, $\mathbf{q}$, yields a confidence region of resolvability. That is,

$$\mathbf{q}^* \mathbf{Q}\, \mathbf{q} = k^2(c) \ . \tag{5.11}$$

This equation defines the hyperellipsoid of uncertainty for a particular model perturbation at a confidence interval, k(c).

By fixing k(c) to a particular value, taken to be 1.96 in this problem, we calculate possible model perturbations for which the equation of the ellipsoid is solved. Any model perturbation vector which lies inside this ellipsoid is unresolvable at the confidence interval, k(c), while any model perturbation vector which protrudes this ellipsoid is resolvable at that confidence level. In the example considered here, we will limit the analysis to two dimensions. With this limitation, we can define an ellipse of uncertainty for combinations of model parameter pairs. As we will see in the examples below, this analysis also allows

the consideration of the coupling between the various model parameters.

The ellipse of uncertainty is shown for various fault model parameter pairs in Figure 5.10. In Figure 5.10, the moments are given in units of 10^{26} dyne-cm, and the angles are expressed in degrees. In Figure 5.10a, we have considered the area of uncertainty when the moments of the two deepest source double couples are allowed to vary. We see that M_{o_1} has an uncertainty of only .05 x 10^{26} dyne-cm when it is allowed to vary alone. Perturbations larger than this value would be resolvable by the data unless the magnitude of the moment on the adjacent double couple (M_{o_2}) was also allowed to vary. The maximum uncertainty that M_{o_1} can take in this coupled system is shown by the projection of the maximum excursion of the ellipse onto the M_{o_1} axis. The maximum uncertainty of M_{o_2} is similarly calculated.

The ratio of the uncertainty measured at the point where the ellipse crosses the axis of a model variable and the maximum uncertainty of that variable defines a coefficient which reflects the coupling of the two variables. We will call this ratio the model co-variance coefficient (MCVC). For a co-variance coefficient equal to 1.0, there is no coupling between parameters. That is, the maximum

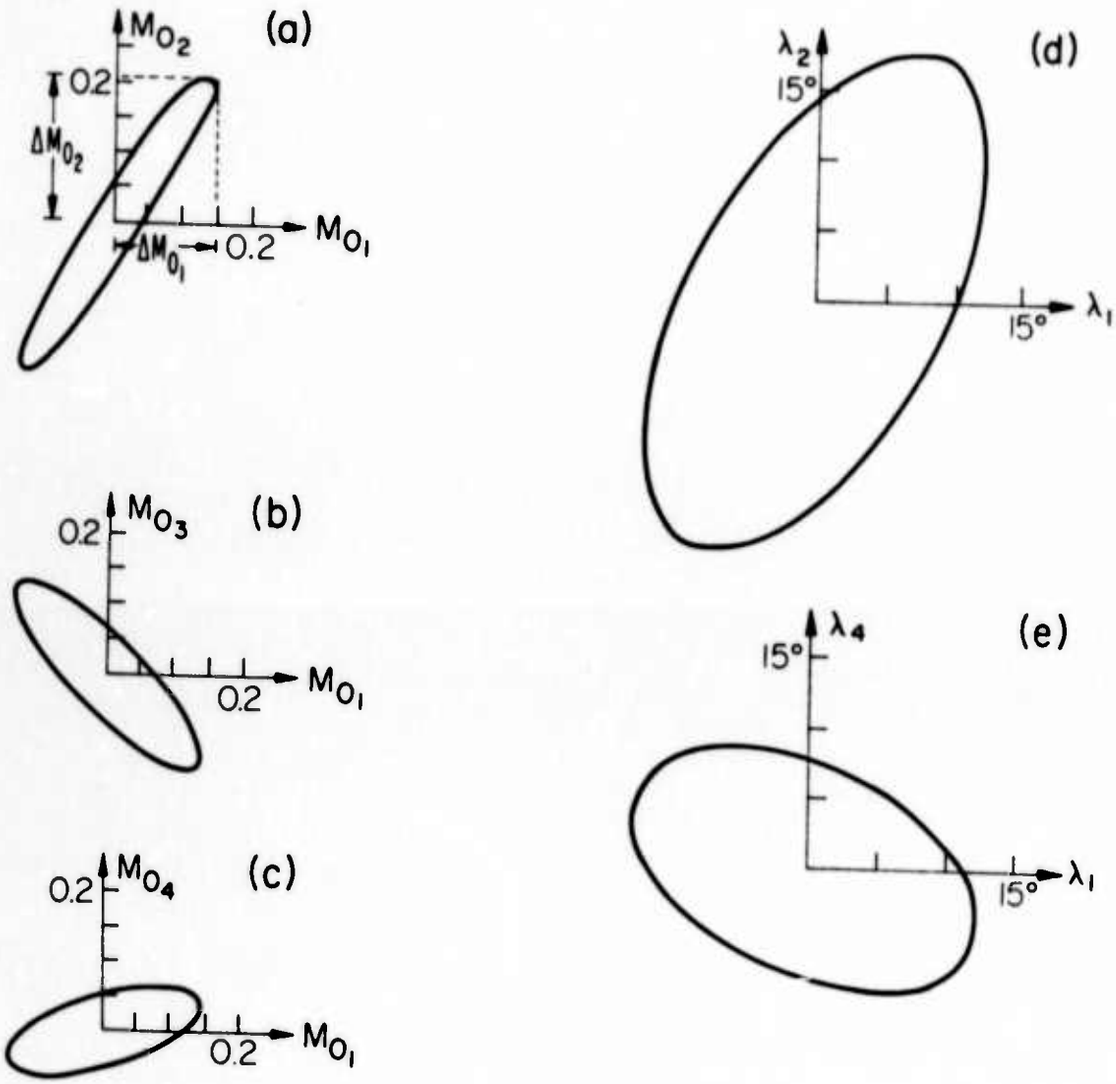

Figure 5.10 (a-e). Uncertainty ellipses for various fault model parameter pairs. Combinations of perturbations which fall inside the ellipses are not detectable by the data at the 95% confidence level. Moments are given in units of 10^{26} dyne-cm; angles are expressed in degrees.

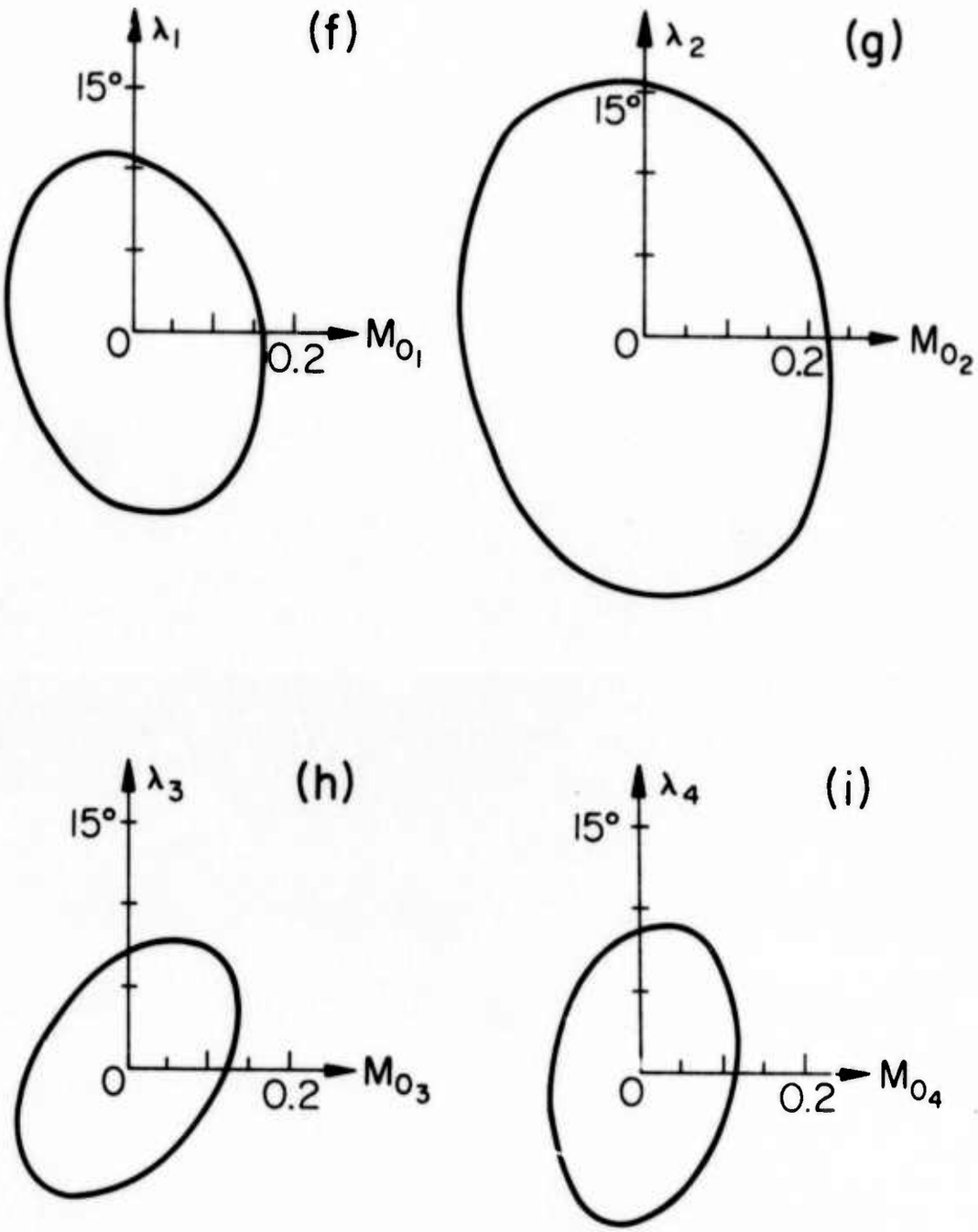

Figure 5.10 (f-i). Uncertainty ellipses for various fault model parameter pairs. Combinations of perturbations which fall inside the ellipses are not detectable by the data at the 95% confidence level. Moments are given in units of 10^{26} dyne-cm; angles are expressed in degrees.

uncertainty of one variable is not dependent on the uncertainty of the other variable. For coefficient values less than 1.0, the coupling increases with decreasing values. Figures 5.10a-c show how the coupling between the individual sources decreases with increasing distance between the sources. We see that there is strong coupling between M_{o_1} and M_{o_2} (MCVC=.30) but very little coupling between M_{o_1} and M_{o_4} (MCVC=.85). In part a of the figure, we see that the coupling is in a positive sense between M_{o_1} and M_{o_2}, i.e., an increase in one moment is traded-off with an increase in the other. Between M_{o_1} and M_{o_3}, the coupling is in the opposite sense, and between M_{o_1} and M_{o_4} the coupling that exists is in a positive direction. Figures 5.10d-e show that adjacent slip angles are slightly coupled, but much less so than their respective moment values. The MCVC for the λ_1-λ_2 pair is .75. As the distance increases between sources, the relative coupling between the slip angles of the sources decreases rapidly. Figures 5.10f-i show how the moment and slip angle for the individual sources are related. These results are somewhat surprising in that the slip angle and moment for individual sources are almost completely decoupled. The MCVCs for these parameter pairs range from .90 to .95.

In these figures, we observe that the maximum coupled

uncertainty a particular variable can acquire is constant from comparison to comparison. This uncertainty is the standard error for that variable. Mathews and Walker (1964) show that this standard error is given by

$$\varepsilon_i = \sqrt{Q_{ii}^{-1}} .$$

Generalizing this expression, we can say that the values of the model parameters are known at a confidence level c when the errors are expressed as

$$\varepsilon_i = \sqrt{Q_{ii}^{-1}}\ k(c) . \qquad (5.12)$$

This is the uncertainty which we will assume for the model variables. These uncertainties at the 95% confidence level are given below:

$$\Delta M_{o_1} = 0.15 \times 10^{26} \text{ dyne-cm}$$

$$\Delta M_{o_2} = 0.21 \times 10^{26} \text{ dyne-cm}$$

$$\Delta M_{o_3} = 0.13 \times 10^{26} \text{ dyne-cm}$$

$$\Delta M_{o_4} = 0.11 \times 10^{26} \text{ dyne-cm}$$

$$\Delta\lambda_1 = 13^\circ$$

$$\Delta\lambda_2 = 18^\circ$$

$\Delta\lambda_3 = 10°$

$\Delta\lambda_4 = 9°$

$\Delta\lambda_R = 5°$

$\Delta V_R = 0.2$ km/sec.

Comparison with Static Solution. We would now like to compare the solution for the fault model of the San Fernando earthquake derived with surface data to that obtained with the static displacements. To do this, we will sum the moments of the individual static fault elements for the elements that fall within a depth range around the location of the double couple sources. We will assume that the actual static moment distribution will be bracketed by the acceptable dislocation models which gave the maximum and minimum moments. The moments for the two models are shown in Figure 5.11. We see here that for the upper 10 km of the fault system there is very good agreement in the static and dynamical solutions. The only significant difference between the two solutions is the moment in the hypocentral region. The surface wave study indicates a moment which is a factor of 2-3 times greater than that predicted by the static data. We recall from the previous chapter that the uncertainties in this area were larger than for the more shallow areas. In the surface wave study, this was not the case. The uncertainty in the hypocentral region was not

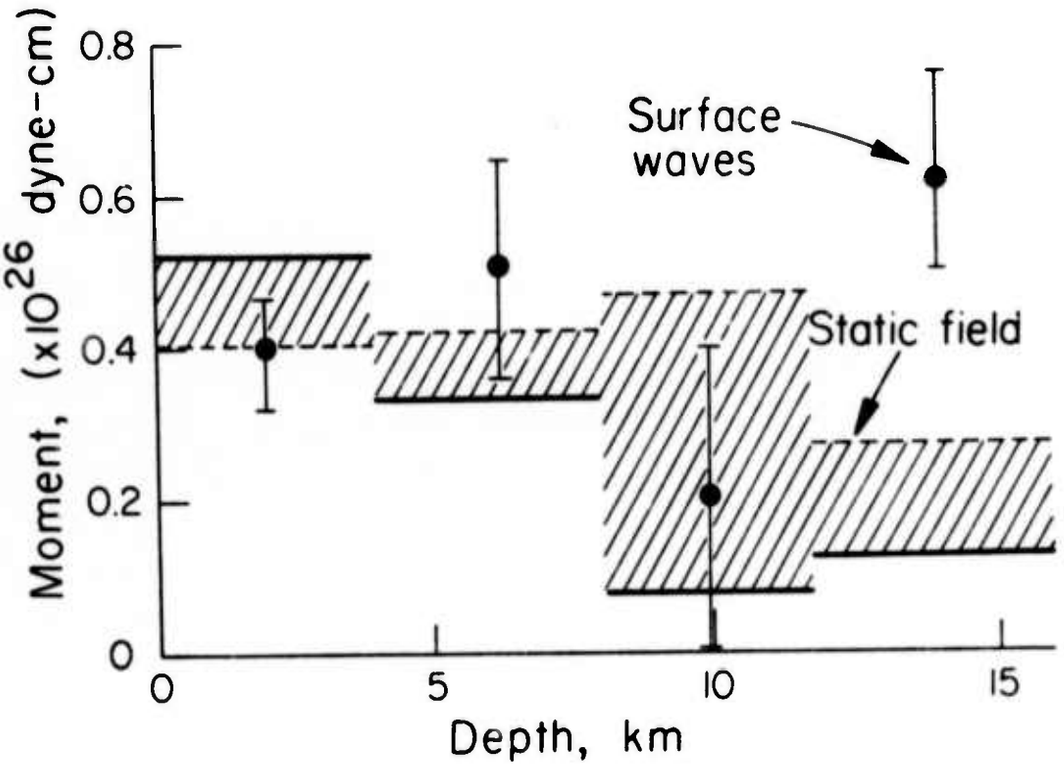

Figure 5.11. Comparison of the moment-depth distribution function found from the static study and the surface wave study. Static moments are averaged over the indicated depth ranges. The static moment distribution from the dislocation model shown in Figure 4.5 and 4.10 is shown as a solid and dashed line respectively.

substantially different from the other areas. If we assume that the fault geometry used in the last chapter is correct, then the surface wave study indicates 5.5 m of displacement over an area of 36 km^2 in the hypocentral region. This compares favorably with that derived by Hanks (1974) of 7.5 m over about the same area. This last calculation was based on still another data set of this event, namely near-field strong motion records.

5.7 Conclusions.

In this chapter, we have seen how theoretical spectral values of surface waves can be calculated numerically for an approximation to a finite source. We have shown that when non-uniform excitation of energy occurs during faulting over some depth-distributed fault surface, the resulting spectral amplitudes can be far different from that of a non-depth-distributed source at the same depth of initiation.

Rayleigh wave data were calculated from a set of 18 WWSSN stations and normalized by correcting for the various source to receiver paths. An inversion scheme was used to find the set of fault model parameters which fit the observed spectral data in a least-squares sense. The best fit solution gave a distributed moment of 1.7×10^{26} dyne-cm, and it was found that both the moment and slip angle for this event varied along the down-dip width of the fault.

The slip angle varied in such a way that the displacements became more predominantly dip slip as the dislocation propagated upward from the point of initial rupture at about 3.0 km/sec. Also indicated by the surface wave data is that the propagation proceeded in a direction 5°-10° away from the normal of the strike of the fault. The fault model solution obtained by the surface wave inversion compares very favorably with that given by the inversion of the static displacement data with the exception of the initial dislocation in the hypocentral region where the static data field gives poor resolution.

Wyss (1971) obtains an average moment from the long period surface waves at two European stations (which were not included in this data set) of 1.9×10^{26} dyne-cm. Canitez and Toksöz (1972) fit the surface wave spectra at 6 stations in the northeast and southeast geodetic azimuths with a single point source at a depth of 14 km. These authors obtain a moment of 0.75×10^{26} dyne-cm and a rake angle of 45°. Obvious reasons for obtaining different values of moment and slip angle by these authors and the present study are 1) the non-depth-distributed source gives rise to a different radiation pattern than a depth-distributed source, and 2) the azimuthal coverage of stations was more limited in the Canitez-Toksöz data set than

in the data set used here. Comparing their data set to that used here, we find that, if the spectra at the stations used in those authors' study were discretized in the same manner as in this chapter, then their data set would have only approximately 40% of the total information which constrains the model variables as was used in this study.

Finally, we feel that the technique of the hybridization of the numerical approximation of a finite fault and the least-squares inversion formalism allows the maximum derivation of information about the source from a set of corrected surface wave observations. Use of the operators associated with the inversion methods provides a powerful tool to determine a priori which data would be most beneficial in determining the source parameters and to estimate the uncertainties in the calculated model parameters and to determine the relative coupling between various parameters. It is hoped that these techniques can be extended to the inversion of other seismic data. The simplest extension would be the inversion of Rayleigh/Love spectral ratios. This type of data would yield far better results than when each is analyzed separately because of the cancellation of error inducing path effects.

BIBLIOGRAPHY

Aki, K., Generation and propagation of G waves from the Niigata earthquake of June 16, 1964, Part 2. Estimation of earthquake moment, released energy, and stress-strain drop from the G wave spectrum, *Bull. Earthquake Res. Inst., Tokyo Univ.*, *44*, 73-88, 1965.

Aki, K., Seismic moment and stress-drop, Paper presented at the Annual Meeting of the Seismological Society of America, Symposium on the San Fernando earthquake of February 9, 1971, Riverside, CA, March 25, 1971.

Alewine, R. W., III, and T. H. Jordan, Generalized inversion of earthquake static displacement fields, *Geophys. J. Roy. Astr. Soc.*, *35*, 357-361, 1973.

Alewine, R. W., III, and P. H. Jungels, Application of stochastic inversion theory and the finite-element method to zero-frequency seismology: The 1964 Alaska earthquake, submitted to *Geophys. J. Roy. Astr. Soc.*, 1973.

Alexander, S. S., Crustal structure in the western United States from multi-mode surface wave dispersion, Ph.D. thesis, California Institute of Technology, Pasadena, 229 pp., 1963.

Algermissen, S. T., Seismological investigation of the Prince William Sound earthquake and aftershocks, *Trans. Am. Geophys. Union*, *45*, 633, 1964.

Algermissen, S. T., Prince William Sound, Alaska earthquake of March 28, 1964, and aftershock sequence, *Geol. Soc. Amer. Spec. Pap.*, *82*, 2, 1965.

Algermissen, S. T., Mechanism of the Prince William Sound earthquake, *ESSA Symposium on Earthquake Prediction*, U. S. Dept. of Commerce, Environmental Science Services Admin., 20-25, 1966.

Algermissen, S. T., W. A. Rinehart, R. W. Sherburne, and W. H. Dillinger, Preshocks and aftershocks, *in*, (K. B. Krauskopf, Ed.), *The Great Alaska Earthquake of 1964, Seismology and Geodesy*, U. S. National Academy of Sciences, Washington, D.C., 313-364, 1972.

Allen, C. R., G. R. Engen, T. C. Hanks, J. M. Nordquist, and W. R. Thatcher, Main shock and larger aftershocks of the San Fernando earthquake, February 9 through March 1, 1971, *U.S. Geol. Surv. Prof. Pap. 733*, 17-20, 1971.

Allen, C. R., T. C. Hanks, and J. Whitcomb, San Fernando earthquake: Seismological studies and their implications, *Calif. Div. Mines and Geol. Bull. 196*, in press, 1973.

Archambeau, C. B., Elastodynamic source theory, Ph.D. thesis, California Institute of Technology, Pasadena, 1964.

Archambeau, C. B., General theory of elastodynamic source fields, *Rev. Geophys.*, *6*, 241-288, 1968.

Archambeau, C. B., The theory of stress wave propagation from explosions in prestressed media, *Geophys. J. Roy. Astr. Soc.*, *29*, 329-366, 1972.

Archambeau, C. B., and C. Sammis, Seismic radiation from explosions in prestressed media and the measurement of tectonic stress in the earth, *Rev. Geophys.*, *8*, 473-499, 1970.

Asada, T., and S. Asano, Crustal structures of Honshu, Japan, *in, The Crust and Upper Mantle of the Japanese Area, Part 1- Geophysics*, Earthquake Res. Inst., Tokyo Univ., 45 pp., 1972.

Bacus, G. E., and J. F. Gilbert, Numerical applications of a formalism for geophysical inverse problems, *Geophys. J. Roy. Astr. Soc.*, *13*, 247-276, 1967.

Bacus, G. E., and J. F. Gilbert, The resolving power of gross earth data, *Geophys. J. Roy. Astr. Soc.*, *16*, 169-205, 1968.

Bacus, G. E., and J. F. Gilbert, Constructing P-velocity models to fit restricted sets of travel-time data, *Bull. Seismol. Soc. Am.*, *59*, 1407-1414, 1969.

Bacus, G. E., and J. F. Gilbert, Uniqueness in the inversion of inaccurate gross earth data, *Phil. Trans. Roy. Soc. London, Ser. A.*, *226*, 123-132, 1970.

Bamford, S. A. D., Applications of simulated data studies to crustal refraction seismology, *Bull. Seismol. Soc. Am.*, *61*, 1013-1031, 1971.

Barnes, D. F., Gravity changes during the Alaska earthquake, *J. Geophys. Res.*, *71*, 451-456, 1966.

Bath, M., Crustal structure of Iceland, *J. Geophys. Res.*, *65*, 1793-1805, 1960.

Benioff, H., Orogenesis and deep crustal structure: additional evidence from seismology, *Geol. Soc. Amer. Bull.*, *65*, 385-400, 1954.

Ben-Menahem, A., Radiation of seismic surface waves from finite moving sources, *Bull. Seismol. Soc. Am.*, *51*, 401-435, 1961.

Ben-Menahem, A., Observed attenuation and Q values of seismic surface waves in the upper mantle, *J. Geophys. Res.*, *70*, 4641-4651, 1965.

Ben-Menahem, A., and A. Gillon, Crustal deforamtion by earthquakes and explosions, *Bull. Seismol. Soc. Am.*, *60*, 193-215, 1970.

Ben-Menahem, A., and D. G. Harkrider, Radiation patterns of seismic surface waves from buried dipolar point sources in a flat stratified earth, *J. Geophys. Res.*, *69*, 2605-2620, 1964.

Ben-Menahem, A., M. Roseman, and M. Israel, Source mechanism of the Alaskan earthquake of 1964 from amplitudes of free oscillations and surface waves, *Phy. Earth and Planet. Interiors*, *5*, 1-29, 1972.

Ben-Menahem, A., and S. J. Singh, Multipolar elastic fields in a layered half-space, *Bull. Seismol. Soc. Am.*, *58*, 1519-1572, 1968a.

Ben-Menahem, A., and S. J. Singh, Eigenvector expansions of Green's dyads with application to geophysical theory, *Geophys. J. Roy. Astr. Soc.*, *16*, 417-452, 1968b.

Ben-Menahem, A., and S. J. Singh, Deformation of a spherical earth by finite dislocations, *in*, (L. Mansinha et al., Ed.), *Earthquake Displacement Fields and the Rotation of the Earth*, 39-42, 1970.

Ben-Menahem, A., S. J. Singh, and F. Solomon, Deformation of a spherical earth model by internal dislocations, *Bull. Seismol. Soc. Am.*, *59*, 813-853, 1969.

Ben-Menahem, A., S. J. Singh, and F. Solomon, Deformation of a homogenous earth model by finite dislocations, *Rev. Geophys.*, *8*, 591-632, 1970.

Berg, E., The Alaska earthquake, its location and seismic setting, *in*, *Science in Alaska, 1964: Proc. 15th Alaskan Sci. Conf., College, Alaska*, Amer. Assoc. Advanc. Sci., 218-232, 1965.

Biehler, S., Geophysical study of the Salton Trough of Southern California, Ph.D. thesis, California Institute of Technology, Pasadena, 1964.

Blundell, D. J., and R. Parks, A study of the crustal structure beneath the Irish Sea, *Geophys. J. Roy. Astr. Soc.*, *17*, 45-62, 1969.

Braslau, D., and P. Lieber, Three dimensional fields due to a Volterra dislocation imbedded in a layered half-space: Analytical representation of a seismic mechanism, *Bull. Seismol. Soc. Am.*, *58*, 613-628, 1968.

Brune, J. N., Surface waves and crustal structure, *in*, (P. J Hart, Ed.), *The Earth's Crust and Upper Mantle, Geophysical Monograph 13*, American Geophysical Union, 230-242, 1969.

Brune, J. N., and C. R. Allen, A low stress-drop, low magnitude earthquake with surface faulting: the Imperial, California, earthquake of March 4, 1966, *Bull. Seismol. Soc. Am.*, *57*, 501-514, 1967.

Brune, J. N., and J. Dorman, Seismic waves and earth structure in the Canadian shield, *Bull. Seismol. Soc. Am.*, *53*, 167-210, 1963.

Bucher, R. L., and R. B. Smith, Crustal structure of the eastern Basin and Range Province and the northern Colorado Plateau from phase velocities of Rayleigh waves, *in*, (J. G. Heacock, Ed.), *The Structure and Physical Properties of the Earth's Crust, Geophys. Monograph 14*, American Geophysical Union, 59-70, 1971.

Burford, R. O., R. O. Castle, J. P. Kinoshita, S. H. Kirby, R. T. Ruthven, and J. C. Savage, Preliminary measurements of tectonic movement, *U. S. Geol. Surv. Prof. Pap. 733*, 80-85, 1971.

Burridge, R., and L. Knopoff, Body force equivalents for seismic dislocations, *Bull. Seismol. Soc. Am., 54*, 1875-1888, 1964.

Canitez, N., and M. N. Toksoz, Focal mechanism and source depth of earthquakes from body and surface wave data, *Bull. Seismol. Soc. Am., 61*, 1369-1379, 1971.

Canitez, N., and M. N. Toksoz, Static and dynamic study of earthquake source mechanism: San Fernando earthquake, *J. Geophys. Res., 77*, 2583-2594, 1972.

Chapman, R. H., Gravity base station network, *Calif. Div. Mines and Geol. Special Report 90*, 49pp., 1966.

Chinnery, M. A., The deformation of the ground around surface faults, *Bull. Seismol. Soc. Am., 51*, 355-372, 1961.

Chinnery, M. A., The stress changes that accompany strike-slip faulting, *Bull. Seismol. Soc. Am., 53*, 921-932, 1963.

Chinnery, M. A., The vertical displacements associated with transcurrent faulting, *J. Geophys. Res., 70*, 4627-4632, 1965.

Chinnery, M. A., Theoretical fault models, *Pub. Dominion Obs., Ottawa, 17*, 211-223, 1969.

Chinnery, M. A., and D. B. Jovanovich, Effect of earth layering on earthquake displacement fields, *Bull. Seismol. Soc. Am., 62*, 1629-1639, 1972.

Chinnery, M. A., and J. A. Petrak, The dislocation fault model with a variable discontinuity, *Tectonophysics*, *5*, 513-529, 1968.

Cisternas, A., Crustal structure of the Andes from Rayleigh wave dispersion, *Bull. Seismol. Soc. Am.*, *51*, 381-388, 1961.

Cohen, T. J., Source-depth determinations using spectral, pseudo-autocorrelation, and cepstral analysis, *Geophys. J. Roy. Astr. Soc.*, *20*, 223-231, 1970.

Corbato, C. E., Bouguer gravity anomalies of the San Fernando Valley, California, *California Univ. Pubs. Geol. Sci.*, *46*, 1-32, 1963.

Dillinger, W., and A. F. Espinosa, Preliminary fault-plane solution for the San Fernando earthquake, *U.S. Geol. Surv. Prof. Pap. 733*, 142-149, 1971.

Dorman, J., M. Ewing, and J. Oliver, Study of shear velocity distribution in the upper mantle by mantle Rayleigh waves, *Bull. Seismol. Soc. Am.*, *50*, 87-115, 1960.

Ellingwood, C. F., and R. O. Williamson, Control resurveys and the San Fernando earthquake (a preliminary analysis), *in, Papers from the 1971 ASP-ACSM Fall Conv.*, Amer. Cong. on Surveying and Mapping, Washington, D. C., 148-178, 1971.

Ewing, J., Seismic model of the Atlantic Ocean, *in*, (P. J. Hart, Ed.), *The Earth's Crust and Upper Mantle, Geophysical Monograph 13*, American Geophysical Union, 220-225, 1969.

Ewing, J., M. Ewing, and R. Leyden, Seismic profiler study of the Blake Plateau, *Bull. Am. Assoc. Petrol. Geol.*, *50*, 1948-1971, 1966.

Ewing, M., R. Houtz, and J. Ewing, South Pacific sediment distribution, *J. Geophys. Res.*, *74*, 2477-2493, 1969.

Ewing, M., and F. Press, Determination of crustal structure from phase velocity of Rayleigh waves, 3, The United States, *Bull. Geol. Soc. Amer.*, *70*, 229-244, 1959.

Fisher, R. L., and R. W. Raitt, Topography and structure of the Peru-Chile trench, *Deep-Sea Res.*, *9*, 423-443, 1962.

Fitch, T. J., and C. H. Scholtz, Mechanism of underthrusting in southwest Japan: a model of covergent plate interaction, *J. Geophys. Res.*, *76*, 7260-7292, 1971.

Flinn, E. A., T. J. Cohen, and D. W. McCowan, Detection and analysis of multiple seismic events, *Bull. Seismol. Soc. Am.*, *63*, 1921-1936, 1973.

Franklin, J. N., Well-posed stochastic extensions of ill-posed linear problems, *J. Math. Anal. Appl.*, *31*, 682-716, 1970.

Grantz, A., G. Plafker, and J. E. Case, Tectonics of Alaska's Good Friday earthquake, *Program, 1964 Ann. Meeting, Geol. Soc. Amer.*, *77*, 1964a.

Grantz, A., G. Plafker, and R. Kachadoorian, Alaska's Good Friday earthquake, March 27, 1964, *U.S. Geol. Surv. Circ. 491*, 1964b.

Gregersen, S., Surface wave dispersion and crustal structure in Greenland, *Geophys. J. Roy. Astr. Soc.*, *22*, 29-39, 1970.

Gutenberg, B., Travel times of principal P and S phases over small distances in southern California, *Bull. Seismol. Soc. Am.*, *34*, 13-32, 1944.

Gutenberg, B., Amplitudes of surface waves and magnitudes of shallow earthquakes, *Bull. Seismol. Soc. Am.*, *35*, 3-12, 1945.

Gutenberg, B., and C. F. Richter, On seismic waves (third paper), *Ger. Beitr. zur Geophys.*, *47*, 73-131, 1936.

Hagiwara, T., A note on the theory of the electromagnetic seismograph, *Bull. Earthquake Res. Inst., Tokyo Univ.*, *36*, 139-164, 1958.

Hagiwara, Y., and H. Tajima, Secular changes in gravity, *in, Publications for the 50th anniversary of the great Kanto earthquake, 1923*, Earthquake Res. Inst., Tokyo, Univ., 311-327, 1973.

Hales, A. L., and T. Asada, Crustal structures in coastal Alaska, *in*, (J. S. Steinhart and T. J. Smith, Ed.), *The Earth beneath the Continents, Geophysical Monograph 10*, 420-432, 1966.

Hanks, T. C., A contribution to the determination and interpretation of seismic source parameters, Ph.D. thesis, California Institute of Technology, Pasadena, 184 pp., 1972.

Hanks, T. C., The faulting mechanism of the San Fernando earthquake, submitted to *J. Geophys. Res.*, 1974.

Hanks, T. C., T. H. Jordan, and J. B. Minster, Precise locations of aftershocks of the San Fernando earthquake, 2300 (GMT) February 10 - 1700 February 11, 1971, *U.S. Geol. Surv. Prof. Pap. 733*, 21-23, 1971.

Harada, Y., Geodetic work in Japan with special reference to the Matsushiro earthquakes, *Trans. Amer. Geophys. Union, 50*, 390-391, 1968.

Harding, S. T., and S. T. Algermissen, Focal mechanism of the Prince William Sound, Alaska, earthquake of March 28, 1964, *Bull. Seismol. Soc. Am.*, *59*, 799-811, 1969.

Harkrider, D. G., Surface waves in multilayered media I. Rayleigh and Love waves from buried sources in a multilayered elastic half-space, *Bull. Seismol. Soc. Am.*, *54*, 627-679, 1964.

Harkrider, D. G., Surface waves in multilayered elastic media. Part II. Higher mode spectra and spectral ratios from point sources in plane-layered earth models, *Bull. Seismol. Soc. Am.*, *60*, 1937-19[illegible], 1970.

Harkrider, D. G., and D. L. Anderson, Surface wave energy from point sources in plane-layered earth models, *J. Geophys. Res.*, *71*, 2967-2980, 1966.

Harkrider, D. G., A. Hales, and F. Press, On detecting soft layers in the mantle with Rayleigh waves, *Bull. Seismol. Soc. Am.*, *53*, 539-548, 1963.

Harrison, J. C., and C. E. Corbato, The Mt. Wilson calibration range--new geodetic measurements in the western United States and some submarine gravity measurements in the northeastern Pacific Ocean, *Trans. Amer. Geophys. Union*, *46*, 212-214, 1965.

Haskell, N. A., The dispersion of surface waves in multilayered media, *Bull. Seismol. Soc. Am.*, *43*, 17-34, 1953.

Hastie, L. M., and J. C. Savage, A dislocation model for the 1964 Alaska earthquake, *Bull. Seismol. Soc. Am.*, *60*, 1389-1392, 1970.

Heezen, B. C., Inland and marginal seas, *in*, (A. R. Ritsema, Ed.), *The Upper Mantle*, *Tectonophysics*, *13*, 293-308, 1972.

Honda, H., and T. Miura, On the strain produced in a semi-infinite elastic solid by statical surface forces, with some applications to seismology, *Geophys. Mag.*, *9*, 61-81, 1935.

Hunt, T. M., Gravity changes associated with the 1968 Inanguhua earthquake, *New Zealand J. Geol. and Geophys.*, *13*, 1050-1051, 1970.

Isacks, B., J. Oliver, and L. R. Sykes, Seismology and the new global tectonics, *J. Geophys. Res.*, *73*, 5855-5899, 1968.

James, D. E., Andean crustal and upper mantle structure, *J. Geophys. Res.*, *76*, 3246-3271, 1971.

Jenkins, W. M., *Matrix and Digital Computer Methods in Structural Analysis*, McGraw-Hill, 1969.

Jordan, T. H., Estimation of the radial variation of seismic velocities and density in the earth, Ph.D. thesis, California Institute of Technology, Pasadena, 199 pp., 1972.

Jordan, T. H., and J. B. Minster, Applications of a stochastic inverse to the geophysical inverse problem, *in*, (L. Colin, Ed.), *The Mathematics of Profile Inversion*, Marcell Dekker, Inc., 1972.

Jungels, P. H., Models of tectonic processes associated with earthquakes, Ph.D. thesis, California Institute of Technology, Pasadena, 198 pp., 1973.

Jungels, P. H., and G. A. Frazier, Finite element analysis of the residual displacements for an earthquake rupture: Source parameters for the San Fernando earthquake, *J. Geophys. Res.*, *78*, 5062-5083, 1973.

Kamb, B., L. T. Silver, M. Abrams, B. Carter, T. Jordan, and B. Minster, Pattern of faulting and nature of fault movement in the San Fernando earthquake, *U.S. Geol. Surv. Prof. Pap. 733*, 41-54, 1971.

Kaminuma, K., The crust and upper mantle structure in Japan, Part 2, Crustal structure in Japan from phase velocity of Rayleigh waves, *Bull. Earthquake Res. Inst., Tokyo Univ.*, *44*, 495-510, 1966.

Kanamori, H., The Alaska earthquake of 1964: Radiation of long-period surface waves and source mechanism, *J. Geophys. Res.*, *75*, 5029-5040, 1970.

Kanamori, H., Velocity and Q of Mantle waves, *Phys. Earth Planet. Interiors*, *2*, 259-275, 1970.

Kasahara, K., The nature of seismic origins as inferred from seismological and geodetic observations, I, *Bull. Earthquake Res. Inst., Tokyo Univ.*, *35*, 473-532, 1957.

Kasahara, K., Physical conditions of earthquake faults, II, (A model of strike-slip faults with various dip angles), *Bull. Earthquake Res. Inst., Tokyo Univ.*, *37*, 39-51, 1959.

Kasahara, K., The source region of the Matsushiro swarm earthquakes, *Bull. Earthquake Res. Inst., Tokyo Univ.*, *48*, 581-602, 1970.

Katz, S., and M. Ewing, Seismic refraction measurements in the Atlantic Ocean, Part VII, Atlantic Ocean Basin west of Bermuda, *Bull. Geol. Soc. Amer.*, *67*, 475-487, 1956.

Knopoff, L., Energy release in earthquakes, *Geophys. J. Roy. Astr. Soc.*, *1*, 44-52, 1958.

Kovach, R. L., and F. Press, Rayleigh wave dispersion and crustal structure in the eastern Pacific and Indian Oceans, *Geophys. J. Roy. Astr. Soc.*, *4*, 202-216, 1961.

Kurita, T., Inferences of a layered structure from S wave spectra, Part 2. Study of the structure in selected regions of Japan, *J. Phys. Earth*, *19*, 111-130, 1971.

Lahr, J. C., M. Wyss, and J. A. Hileman, Repeated surveys of small scale figures established across surface fault ruptures following the earthquake, *U.S. Geol. Surv. Prof. Pap. 733*, 86-88, 1971.

Lambert, D. G., E. A. Flinn, and C. B. Archambeau, A comparitave study of the elastic wave radiation from earthquakes and underground explosions, *Geophys. J. Roy. Astr. Soc.*, *29*, 403-432, 1972.

Latham, G., and A. Nowroozi, Waves, weather and ocean bottom microseisms, *J. Geophys. Res.*, *73*, 3945-3956, 1968.

Linville, A. F., Rayleigh wave multipath analysis using a complex cepstrum technique, Special Report No. 2, Long-period array processing development, Texas Instruments Inc., Dallas, Texas, 1971.

Love, A. E. H., *A Treatise on the Mathematical Theory of Elasticity*, 4th Edition, Dover Publications, New York, 1944.

Malloy, R. J., Crustal uplift southwest of Montague Island, Alaska, *Science*, *146*, 1048-1049, 1964.

Malloy, R. J., Seafloor upheaval, *Geo-Marine Technology*, *1*, 22-26, 1965.

Malloy, R. J., and G. F. Merrill, Vertical crustal movement of the sea floor associated with the Prince William Sound, Alaska, earthquake, *in*, (L. E. Leipold, Ed.), *The Prince William Sound, Alaska, Earthquake of 1964 and aftershocks*, U.S. Dept. of Commerce, Envir. Sci. Serv. Admin., Pub. 10-3, II, 327-338, 1969.

Mansinha, L., and D. E. Smylie, The displacement fields of inclined faults, *Bull. Seismol. Soc. Am.*, *61*, 1433-1440, 1971.

Martin, H. C., *Introduction to Matrix Methods of Structural Analysis*, McGraw-Hill, 1966.

Maruyama, T., On the force equivalents of dynamical elastic dislocations with reference to the earthquake source mechanism, *Bull. Earthquake Res. Inst., Tokyo Univ.*, *41*, 467-486, 1963.

Maruyama, T., Statical elastic dislocations in an infinite and semi-infinite medium, *Bull. Earthquake Res. Inst., Tokyo Univ.*, *42*, 289-368, 1964.

Mathews, J., and R. L. Walker, *Mathematical Methods of Physics*, W. A. Benjamin, Inc., 1964.

Matumoto, T., and R. A. Page, Microaftershocks following the Alaska earthquake of March 28, 1964: Determination of hypocenters and crustal velocities in the Kenai Peninsula-Prince William Sound area, *in*, (L. E. Leipold, Ed.), *The Prince William Sound, Alaska, Earthquake of 1964 and Aftershocks*, U.S. Dept. of Commerce, Envir. Sci. Serv. Admin., Pub. 10-3, II, 157-183, 1969.

McEvilly, T. V., Central U. S. crust-upper mantle structure from Love and Rayleigh wave phase velocity inversion, *Bull. Seismol. Soc. Am.*, *54*, 1997-2015, 1964.

McGarr, A., Amplitude variations of Rayleigh waves--propagation across a continental margin, *Bull. Seismol. Soc. Am.*, *59*, 1281-1305, 1969.

McGarr, A., and L. E. Alsop, Transmission and reflection of Rayleigh waves at vertical boundaries, *J. Geophys. Res.*, *72*, 2169-2180, 1967.

McGinley, J. R., A comparison of observed permanent tilts and strains with those calculated from displacement dislocations in elastic earth models, Ph.D. thesis, California Institute of Technology, Pasadena, 290 pp., 1969.

Mikumo, T., A study on crustal structure in Japan by the use of seismic and gravity data, *Bull. Earthquake Res. Inst., Tokyo Univ., 44*, 965-1007, 1966.

Mikumo, T., Faulting process of the San Fernando earthquake of February 9, 1971, inferred from static and dynamic near-field displacements, *Bull. Seismol. Soc. Am., 63*, 249-269, 1973.

Mindlin, R. D., Force at a point in the interior of a semi-infinite solid, *Physics, 7*, 195-202, 1936.

Mindlin, R. D., and D. H. Cheng, Nuclei of strain in the semi-infinite solid, *J. Appl. Physics, 21*, 926-930, 1950.

Minster, J. B., Elastodynamics of Failure in a Continuum, Ph.D. thesis, California Institute of Technology, Pasadena, 530 pp., 1974.

Minster, J. B., T. H. Jordan, P. Molnar, and E. Haines, Numerical modeling of instantaneous plate tectonics, submitted to *Geophys. J. Roy. Astr. Soc.*, 1974.

Mitchell, B. J., Radiation and attenuation of Rayleigh waves from the Southeastern Missouri earthquake of October 21, 1965, *J. Geophys. Res., 78*, 886-899, 1973.

Mitchell, B. J., and M. Landisman, Electromagnetic seismograph constants by least-squares inversion, *Bull. Seismol. Soc. Am., 59*, 1335-1348, 1969.

Nason, R. D., Instrumental monitoring of postearthquake fault movements, *U.S. Geol. Surv. Prof. Pap. 733*, 89-90, 1971.

Noble, B., *Applied Linear Algebra*, Prentice-Hall, Inc., Englewood Cliffs, N.J., 1969.

Nuttli, O. W., Seismic wave attenuation and magnitude relations for eastern North America, *J. Geophys. Res., 78*, 876-885, 1973.

Oakeshott, G. B., Geology and mineral deposits of the San Fernando Quadrangle, Los Angeles County, California, *Calif. Div. Mines and Geol. Bull. 172*, 147 pp., 1958.

Officer, C. B., M. Ewing, and P. Wuenshel, Seismic refraction measurements in the Atlantic Ocean, Part IV, Bermuda, Bermuda rise and Nares Basin, *Bull. Geol. Soc. Amer.*, *63*, 777-808, 1952.

Oliver, H. W., S. L. Robbins, R. B. Grannell, R. W. Alewine, and S. Biehler, Surface and subsurface movements determined by remeasuring gravity, *Calif. Div. Mines and Geol. Bull. 196*, Chapt. 10, in press, 1973.

Palmer, D. F., and T. L. Henyey, San Fernando earthquake of 9 February 1971: Pattern of faulting, *Science*, *172*, 712-715, 1971.

Parkin, E. J., Horizontal displacements, pt. 2 of *Alaskan surveys to determine crustal movement*, U.S. Coast and Geodetic Surv., 11 pp., 1966.

Payo, G., Crustal phases across the Iberian Peninsula region, *Ann. Geofis.*, *17*, 523-532, 1964.

Payo, G., Structure of the crust and upper mantle in the Iberian shield by means of a long period triangular array, *Geophys. J. Roy. Astr. Soc.*, *20*, 493-508, 1970.

Piermattei, R., and A. Nowroozi, Dispersion of Rayleigh waves for purely oceanic paths in the Pacific, *Bull. Seismol. Soc. Am.*, *59*, 1905-1926, 1969.

Plafker, G., Tectonic deformation associated with the 1964 Alaska earthquake, *Science*, *148*, 1675-1687, 1965.

Plafker, G., Surface faults on Montague Island associated with the 1964 Alaska earthquake, *U.S. Geol. Surv. Prof. Pap. 543-G*, 42 pp., 1967.

Plafker, G., Tectonics of the March 27, Alaska earthquake, *U.S. Geol. Surv. Prof. Pap. 543-I*, 74 pp., 1969.

Plafker, G., Alaskan earthquake of 1964 and Chilean earthquake of 1960: Implications for arc tectonics, *J. Geophys. Res.*, *77*, 901-925, 1972.

Plafker, G., and M. Rubin, Vertical tectonic displacements in South-Central Alaska during and prior to the great 1964 earthquake, *J. Geosci., Osaka City Univ., 10*, 1-14, 1967.

Pope, A. J., Strain analysis of horizontal crustal movements in Alaska based on triangulation surveys before and after the earthquake, *in*, (K. B. Krauskopf, Ed.), *The Great Alaska Earthquake of 1964, Seismology and Geodesy*, U.S. National Academy of Sciences, Washington, D.C., 435-447, 1972.

Press, F., Displacements, strains, and tilts at teleseismic distances, *J. Geophys. Res., 70*, 2395-2412, 1965.

Press, F., Earth models obtained by Monte Carlo inversion, *J. Geophys. Res., 73*, 5223-5234, 1968.

Press, F., Zero frequency seismology, *in*, (P. J. Hart, Ed.), *The Earth's Crust and Upper Mantle, Geophysical Monograph 13*, American Geophysical Union, 171-173, 1969.

Press, F., Earth models consistent with geophysical data, *Phys. Earth and Planet. Interiors, 3*, 3-22, 1970.

Press, F., The earth's interior as inferred from a family of models, *in*, (E. C. Robertson, Ed.), *The Nature of the Solid Earth*, McGraw-Hill, 1972.

Press, F., and D. Jackson, Alaskan earthquake, 27 March 1964: Vertical extent of faulting and elastic strain energy release, *Science, 147*, 867-868, 1965.

Proctor, R. J., R. Crook, M. H. McKeown, and R. L. Moresco, Relation of known faults to surface ruptures, 1971 San Fernando earthquake, southern California, *Geol. Soc. Amer. Bull., 83*, 1601-1618, 1972.

Przemieniecki, J. S., *Theory of Matrix Structural Analysis*, McGraw-Hill, 1968.

Raitt, R. W., Seismic refraction studies of the Pacific Ocean basin, Part I: Crustal thickness of the central equatorial Pacific, *Bull. Geol. Soc. Amer., 67*, 1623-1640, 1956.

Reimnitz, E., Quaternary history and sedimentation of the Copper River delta and vicinity, Ph.D. thesis, University of California, San Diego, 1966.

Rice, D. A., Gravity observations in Alaska, 1964-1965, including some repeat observations, *in*, (L. E. Leipold, Ed.), *The Prince William Sound, Alaska, Earthquake of 1964 and aftershocks*, U.S. Dept. of Commerce, Envir. Sci. Serv. Admin., Pub. 10-3, III, 5-20, 1969.

Robbins, S. L., R. B. Grannell, R. W. Alewine, S. Biehler, and H. W. Oliver, Descriptions, sketch maps, and selected pictures of 87 gravity stations reoccupied after the San Fernando earthquake of February 9, 1971, *U.S. Geol. Surv. Open File Report*, 72 pp., 1973.

Saito, M., and H. Takeuchi, Surface waves across the Pacific, *Bull. Seismol. Soc. Am.*, *56*, 1067-1091, 1966.

Santo, T. A., Division of the Pacific area into seven regions in each of which Rayleigh waves have the same group velocities, *Bull. Earthquake Res. Inst., Tokyo Univ.*, *41*, 719-741, 1963.

Sato, R., Crustal deformation due to a dislocation in a multilayered medium, *J. Phys. Earth*, *19*, 31-46, 1971.

Sato, R., Stress drop for a finite fault, *J. Phys. Earth*, *20*, 397-407, 1972.

Savage, J. C., R. O. Burford, and W. T. Kinoshita, Earth movements from geodetic measurements, *Calif. Div. Mines and Geol. Bull. 196*, in press, 1973.

Savage, J. C., and L. M. Hastie, Surface deformation associated with dip-slip faulting, *J. Geophys. Res.*, *71*, 4897-4904, 1966.

Savage, J. C., and L. M. Hastie, A dislocation model for the Fairview Peak, Nevada, earthquake, *Bull. Seismol. Soc. Am.*, *59*, 1937-1948, 1969.

Schafer, R. W., Echo removal by discrete generalized linear filtering, Ph.D. thesis, Massachusetts Institute of Technology, Cambridge, 1969.

Sezawa, K., The tilting of the surface of a semi-infinite solid due to internal nuclei of strain, *Bull. Earthquake Res. Inst., Tokyo Univ.*, *7*, 1-14, 1929.

Sherburne, R. W., S. T. Algermissen, and S. T. Harding, The hypocenter, origin time, and magnitude of the Prince William Sound earthquake of March 28, 1964, *in*, (L. E. Leipold, Ed.), *The Prince William Sound, Alaska, Earthquake of 1964 and Aftershocks*, U.S. Dept. of Commerce, Envir. Sci. Serv. Admin., Pub. 10-3, II, 49-70, 1969.

Shor, G., Seismic refraction studies off the coast of Alaska (1956-1957), *Bull. Seismol. Soc. Am.*, *42*, 37-57, 1962.

Singh, S. J., Static deformation of a multilayered half-space by internal sources, *J. Geophys. Res.*, *75*, 3257-3263, 1970.

Singh, S. J., Deformation of a multilayered half-space by stress dislocations and concentrated forces, *Bull. Seismol. Soc. Am.*, *61*, 1625-1638, 1971.

Singh, S. J., and A. Ben-Menahem, Displacements and strain fields due to faulting in a sphere, *Phys. Earth Planet. Interiors*, *2*, 77-87, 1969.

Soeda, K., On the deformation produced in a semi-infinite elastic solid by an internal source of stress, *Kenshin Ziho*, *13*, 263-291, 1944.

Starr, A. T., Slip in a crystal and rupture in a solid due to shear, *Cambridge Phil. Soc. Proc.*, *24*, 489-500, 1928.

Stauder, W., Tensional character of earthquake foci beneath the Aleutian Trench with relation to sea-floor spreading, *J. Geophys. Res.*, *73*, 7693-7701, 1968.

Stauder, W., and G. A. Bollinger, The focal mechanism of the Alaska earthquake of March 28, 1964, and of its aftershock sequence, *J. Geophys. Res.*, *71*, 5283-5296, 1966.

Steketee, J. A., On Volterra's dislocations in a semi-infinite elastic medium, *Can. J. Phys.*, *36*, 192-205, 1958a.

Steketee, J. A., Some geophysical applications of the elasticity theory of dislocations, *Can. J. Phys.*, *36*, 1168-1198, 1958b.

Stonley, R., The structural development of the Gulf of Alaska sedimentary province in southern Alaska, *Geol. Soc. London Quart. J.*, *123*, pt. 1, 25-57, 1966.

Sykes, L. R., Aftershock zones of great earthquakes, seismicity gaps, and earthquake prediction for Alaska and the Aleutians, *J. Geophys. Res.*, *76*, 8021-8041, 1971.

Sylvester, A. G., and D. D. Pollard, Afterslip on the Sylmar segment, *Calif. Div. Mines and Geol. Bull. 196*, in press, 1973.

Talwani, M., X. Le Pichon, and M. Ewing, Crustal structure of the mid-ocean ridges; 2. Computed model from gravity and seismic refraction data, *J. Geophys. Res.*, *70*, 341-352, 1965.

Thomson, W. T., Transmission of elastic waves through a stratified medium, *J. Appl. Phys.*, *21*, 89-93, 1950.

Tobin, D. G., and L. R. Sykes, Relationship of hypocenters of earthquakes to the geology of Alaska, *J. Geophys. Res.*, *71*, 1659-1667, 1966.

Toksöz, M. N., A. Ben-Menahem, and D. G. Harkrider, Source mechanism of the Alaska earthquake from long period seismic surface waves, *Trans. Am. Geophys. Union*, *46*, 154, 1965.

Tryggvason, E., Crustal structure of the Iceland region from dispersion of surface waves, *Bull. Seismol. Soc. Am.*, *52*, 359-388, 1962.

Tryggvason, E., Dissipation of Rayleigh wave energy, *J. Geophys. Res.*, *70*, 1449-1455, 1965.

Tryggvason, E., Surface deformation and crustal structure in the Myrdalsjokull area of south Iceland, *J. Geophys. Res.*, *78*, 2488-2497, 1973.

Tryggvason, E., and M. Bath, Upper crustal structure of Iceland, *J. Geophys. Res.*, *66*, 1913-1925, 1961.

Tsai, Y., Use of LP surface waves for source characterization, *Geophys. J. Roy. Astr. Soc.*, *31*, 111-130, 1972.

Tsai, Y., and K. Aki, Simultaneous determination of the seismic moment and attenuation of seismic surface waves, *Bull. Seismol. Soc. Am.*, *59*, 275-287, 1969.

Tsai, Y., and K. Aki, Precise focal depth determination from amplitude spectra of surface waves, *J. Geophys. Res.*, *75*, 5729-5743, 1970.

Tsai, Y., and K. Aki, Amplitude spectra of surface waves from small earthquakes and underground nuclear explosions, *J. Geophys. Res.*, *76*, 3940-3952, 1971.

Tsuboi, C., A. Jitsuakwa, H. Tazima, and A. Okada, Gravity survey along the line of precise levels throughout Japan by means of a Worden gravimeter, *Bull. Earthquake Res. Inst., Tokyo Univ., Suppl. Vol. IV, Part 1*, 1-45, 1953.

Tsubokawa, I., A. Okada, H. Tajima, I. Murata, K. Nagasawa, S. Izutuya, and Y. Ito, Leveling resurvey associated with the area of the Matsushiro earthquake swarms, *Bull. Earthquake Res. Inst., Tokyo Univ.*, *45*, 265-288, 1967.

Turnbull, L. S., D. F. Sun, and S. S. Alexander, Determination of seismic source parameters for several earthquakes using frequency dependent Rayleigh and Love wave radiation patterns, *Trans. Amer. Geophys. Union*, *54*, 1133, 1973.

U.S. Geological Survey Staff, Surface faulting, *U.S. Geol. Surv. Prof. Pap. 733*, 55-76, 1971.

Volterra, V., Sur l'equilibre des corps elastiques multiplement connexes, *Ann. Sci. École Norm. Superieure, Paris, 24*, 401-517, 1907.

von Hake, C., and W. K. Cloud, *United States Earthquakes, 1964*, U.S. Dept. of Commerce, Envir. Sci. Serv. Admin., Coast and Geodetic Surv., Washington, D.C., 91 pp., 1966.

von Huene, R. E., R. J. Malloy, G. G. Shor, and P. St. Amand, Geologic structures in the aftershock region of the 1964 Alaskan earthquake, *J. Geophys. Res., 72*, 3649-3660, 1967.

Vvedenshaya, A. V., The determination of displacement fields by means of dislocation theory, *Bull. Acad. Sci. USSR, Geophys. Ser. 3, English Transl.*, 277-284, 1956.

Vvedenskaya, A. V., Displacements in the surface of a fracture, accompanied by slip, *Bull. Acad. Sci. USSR, Geophys. Ser. 2, English Transl.*, 102-105, 1958.

Wason, H. R., and S. J. Singh, Static deformation of a multilayered sphere by internal sources, *Geophys. J. Roy. Astr. Soc., 27*, 1-14, 1972.

Wentworth, C., and R. Yerkes, Geological setting and larger aftershocks of the San Fernando area, California, *U.S. Geol. Surv. Prof. Pap. 733*, 6-16, 1971.

Wesson, R. L., W. H. K. Lee, and J. F. Gibbs, Aftershocks of the earthquake, *U.S. Geol. Surv. Prof. Pap. 733*, 24-29, 1971.

Wesson, R. L., and D. H. Wilson, Faulting in the San Fernando earthquake of February 9, 1971, *Trans. Amer. Geophys. Union, 53*, 449, 1972.

Whipple, F. J. W., On the theory of the strain in an elastic solid bounded by a plane where there is a nucleus of strain at an internal point, and on the relation of the theory to seismology, *Mon. Not. Roy. Astr. Soc., Geophys. Suppl., 3*, 380-388, 1936.

Whitcomb, J., Fault plane solution of the February 9, 1971, San Fernando earthquake and some aftershocks, *U.S. Geol. Surv. Prof. Pap. 733*, 30-32, 1971.

Whitcomb, J. H., The 1971 San Fernando earthquake series focal mechanism and tectonics, Part II, Ph.D. thesis, California Institute of Technology, Pasadena, 1973.

Whitcomb, J. H., C. R. Allen, J. D. Garmany, and J. A. Hileman, San Fernando earthquake series, 1971: Focal mechanisms and tectonics, *Rev. Geophys.*, *11*, 693-730, 1973.

Whitten, C. A., Crustal movements associated with the Alaskan earthquake, *Trans. Amer. Geophys. Union*, *45*, 633, 1964.

Whitten, C. A., Cartographic and geodetic effects of the Alaskan earthquake, *Geol. Soc. Amer. Spec. Pap.*, *82*, 822, 1965.

Wiggins, R. A., The general linear inverse problem: Implication of surface waves and free oscillations for earth structure, *Rev. Geophys.*, *10*, 251-285, 1972.

Wood, H. O., and C. Richter, A second study of blasting in southern California, *Bull. Seismol. Soc. Am.*, *23*, 95-110, 1933.

Wu, F. T., Parkfield earthquake of June 28, 1966: Magnitude and source mechanism, *Bull. Seismol. Soc. Am.*, *58*, 689-709, 1968.

Wyss, M., Preliminary source parameter determination of the San Fernando earthquake, *U.S. Geol. Surv. Prof. Pap. 733*, 38-40, 1971.

Wyss, M., and J. N. Brune, The Alaska earthquake of 28 March 1964: A complex multiple rupture, *Bull. Seismol. Soc. Am.*, *57*, 1017-1023, 1967.

Wyss, M., and T. C. Hanks, The source parameters of the San Fernando earthquake inferred from teleseismic body waves, *Bull. Seismol. Soc. Am.*, *62*, 591-602, 1972.

Yamakawa, N., On the strain produced in a semi-infinite elastic solid by an interior source of stress, *Zisin*, *8*, 84-98, 1955.

Yamakawa, N., Stress fields in focal regions, *J. Phys. Earth*, *19*, 347-355, 1971.

Zienkiewicz, O. C., *The Finite Element Method in Engineering Science*, McGraw-Hill, 1971.

APPENDICES

Appendix 3

Derivation of Least-Squares Inversion Operators

In this appendix, we will derive the least-squares inverse and the associated operators for three cases. For convenience with respect to manuscript preparation, matrices will be given here in regular typed form, not boldface as in the rest of this thesis. This practice should cause no confusion in this case.

Case I: Least-Squares Inverse with no weighting of the model components and no inclusion of the data variances.

We define the forward problem to be

$$A\,\delta m = \delta d_o \,. \tag{A3.1}$$

where δd_o is the observed data vector, δm is the true model, and A is the operator which maps a function from the model space to the data space. We define the vector $b=\overline{\delta m}$ to be the best estimate of the model, δm, that we can obtain.

In this case, we wish to minimize the fit to the data such that

$$\varepsilon_1^2(b) = ||\delta d_o - \overline{\delta d}||^2 \tag{A3.2}$$

is minimized. Here we have $||Z||^2 = Z^*Z$, and $\overline{\delta d}$ is the calculated fit to the data given by

$$A\, b = \overline{\delta d} \ . \tag{A3.3}$$

Substituting (A3.3) into (A3.2) and expanding, we get

$$\varepsilon_1^2(b) = \delta d_o{}^* \delta d_o - \delta d_o{}^* A\, b - b^* A^* \delta d_o + b^* A^* A\, b \ . \tag{A3.4}$$

Now performing a first order perturbation in δb of (A3.4) and setting to zero implies

$$b = \overline{\delta m} = (A^*A)^\dagger A^* \delta d_o \ , \tag{A3.5}$$

which is the result we are seeking.

Case II: Least-Squares Inverse with no weighting of model components and with the inclusion of the data variance.

Here we have the same forward problem as before, however, each datum, d_{o_i}, has associated with it some variance, σ_i^2. If we assume that the data are unbiased and are statistically independent, then we can write the variances in diagonal form

$$C_{nn} = \begin{bmatrix} \sigma_1^2 & . & . & . & . & 0 \\ . & \sigma_2^2 & & & & . \\ . & & & & & . \\ . & & & . & & . \\ . & & & & . & . \\ 0 & . & . & . & . & \sigma_n^2 \end{bmatrix}$$

We want to minimize the fit to the data in a least-squares sense such that

$$\varepsilon_1^2(b) = ||\delta d_o - \overline{\delta d}||^2_{C_{nn}} \qquad \text{(A3.6)}$$

is minimized. This weighted norm, $||\cdot||_{C_{nn}}$, is defined by

$$||Z||^2_{C_{nn}} = Z^* C_{nn}^{-1} Z \ .$$

Substituting (A3.3) into (A3.6) and expanding, we get

$$\varepsilon_1^2(b) = \delta d_o{}^* C_{nn}^{-1} \delta d_o - \delta d_o{}^* C_{nn}^{-1} A\, b - (Ab)^* C_{nn}^{-1} \delta d_o + (Ab)^* C_{nn}^{-1} (Ab)$$

Performing the first order perturbation of δb on this last equation and setting the result to zero, we obtain

$$b = \overline{\delta m} = (A^* C_{nn}^{-1} A)^\dagger A^* C_{nn}^{-1} \delta d_o \ . \qquad \text{(A3.7)}$$

Case III: Least-Squares Inverse with weighting of the model components and with the inclusion of the data variance.

For some problems, it might be useful to consider a set of non-zero positive weights for the model components. This weighting, or model correlation coefficients, can be defined in the following manner,

$$C_{ss} = \begin{bmatrix} W_1 & . & . & . & . & 0 \\ . & W_2 & & & & . \\ . & & . & & & . \\ . & & & . & & . \\ . & & & & . & . \\ 0 & . & . & . & . & W_M \end{bmatrix} .$$

The error induced through the use of this correlation coefficients is given as the following,

$$\varepsilon_2^2(b) = b^* C_{ss}^{-1} b \ . \qquad \text{(A3.8)}$$

The error of the fit to the data is still given by equation (A3.6). For this case, we want to minimize some quadratic sum of these two errors.

$$\varepsilon^2(b) = \varepsilon_1^2(b)\cos\theta + \varepsilon_2^2(b)\sin\theta \ .$$

This minimization of $\varepsilon^2(b)$ proceeds as before giving

$$b = \overline{\delta m} = Q^{\dagger}(\theta)A^{*}C_{nn}^{-1}\delta d_o \qquad \text{(A3.9)}$$

where $Q^{\dagger}(\theta) = (A^{*}C_{nn}^{-1}A + \tan\theta C_{ss}^{-1})^{\dagger}$.

Substitution of (A3.9) into (A3.3) enables us to write

$$\overline{\delta d} = J\,\delta d_o \ .$$

J is called the data importance matrix and is given by

$$J = A\,Q^{\dagger}(\theta)A^{*}C_{nn}^{-1} \ .$$

The data importance matrix tells how the information in the data set is distributed (Wiggins, 1972). This operator serves the same role in the least-squares inverse as does the model response operator (equation 2.29) in the stochastic inverse. The data importance matrix gives us information as to how the model components as a whole "see" how large an effect individual data values have on the estimation of a model. Minster et al. (1974) show that the trace of this operator is invariant and given to be the number of independent linear combinations of the

data. For the inversion problem to be determinant, this sum must equal the number of independent model parameters.

In both the inversion procedures discussed in this thesis, we have neglected an obvious operator. We will call this operator the perturbation relaxation operator. These operators are defined below.

$$\overline{\delta d} = P_{S.}\,\delta d_o \qquad \text{(Stochastic inverse)}$$

$$\overline{\delta m} = P_{L.S.}\,\delta m \qquad \text{(Least-squares inverse)}$$

where

$$P_{S.} = AWA^{*}(AWA^{*}+C_{nn}\tan\theta)^{\dagger}$$

$$P_{L.S.} = (A^{*}C_{nn}^{-1}A+C_{ss}^{-1}\tan\theta)^{\dagger}(AC_{nn}^{-1}A)$$

These operators show simply that in the stochastic inverse case, when C_{nn} has large values for certain data, these data will be essentially neglected in the fit for the sake of fitting other better determined data. In the least-squares inverse case, when C_{ss} has a very small value for certain model components, the model will try to fit the data by ignoring the contributions from these particular model components. Also, we see that for C_{nn} and C_{ss} fixed,

the point along the trade-off curve influences the perturbation sizes in the iterative inversion scheme.

Appendix 4

Spectral Summation of Two Sources in the Frequency Domain

Consider the addition of two seismic sources by spectral summation. The first source is represented by an amplitude and a phase spectrum of the form $A_1(\omega)\, e^{i\phi_1(\omega)}$. The phase spectra $\phi_1(\omega)$ contains information about both the source and the propagation path. To this spectra we wish to add an additional source represented by $A_2(\omega)\, e^{i[\phi_2(\omega) + \Delta\phi_2(\omega)]}$, where $A_2(\omega)$ is the amplitude spectra of the secondary source, $\phi_2(\omega)$ is the phase spectra of the secondary source, and $\Delta\phi_2(\omega)$ is the additional phase of the secondary source caused by a spatial or temporal offset of the second source from the first source. Propagation effects for traveling a slightly different path from origin to receiver are taken into account with this term. If we let z be the total of the two sources, then we can write,

$$z = Z(\omega)\, e^{i\psi(\omega)} = A_1(\omega)\, e^{i\phi_1(\omega)} + A_2(\omega)\, e^{i[\phi_2(\omega) + \Delta\phi_2(\omega)]}. \qquad \text{(A4.1)}$$

Thus,

$$Z(\omega) = \{A_1^2(\omega)+A_2^2(\omega)+2A_1(\omega)A_2(\omega)\cos[\phi_1(\omega)-\phi_2(\omega)-\Delta\phi_2(\omega)]\}^{1/2} \tag{A4.2}$$

and

$$\psi(\omega) = \tan^{-1} \frac{A_1(\omega)\sin[\phi_1(\omega)]+A_2(\omega)\sin[\phi_2(\omega)+\Delta\phi_2(\omega)]}{A_1(\omega)\cos[\phi_1(\omega)]+A_2(\omega)\cos[\phi_2(\omega)+\Delta\phi_2(\omega)]} . \tag{A4.3}$$

The phase delay of the single original source is given by

$$\tau_{p_1} = \frac{\phi_1(\omega)}{\omega} , \tag{A4.4}$$

and the new phase delay of the summed signal is

$$\tau_{p_z} = \frac{\psi(\omega)}{\omega} . \tag{A4.5}$$

The group delay of the summed signal is given by

$$\tau_{g_z} = \frac{\partial\psi(\omega)}{\partial\omega} . \tag{A4.6}$$

In practice in order to avoid as much as possible the difficulties encountered by the multivaluedness of the

trigonometric functions, we wish to compute only the additional group delay the additional source has over the group delay of the single original source. If we define this additional group delay by $\delta\tau_g$, then

$$\delta\tau_g = \tau_{g_z} - \tau_{g_1} , \tag{A4.7}$$

where τ_{g_1} is the group delay of the original signal. By defining $\frac{\partial\phi_2(\omega)}{\partial\omega} = \tau_{g_2}$ and $\frac{\partial\Delta\phi_2(\omega)}{\partial\omega} = \tau_{g_{2s}}$, we have by equation (A4.6)

$$\tau_{g_z} = \frac{A_1^2(\omega)\tau_{g_1} + A_2^2(\omega)\frac{\Gamma_+\Gamma_-}{2} + \Gamma_+ A_1(\omega)A_2(\omega)\cos(\alpha)}{A_1^2(\omega)+A_2^2(\omega)+2A_1(\omega)A_2(\omega)\cos(\alpha)} \tag{A4.8}$$

where

$$\alpha = \phi_2 + \Delta\phi_2 - \phi_1$$

$$\Gamma_+ = \tau_{g_1} + \tau_{g_2} + \tau_{g_{2s}}$$

$$\Gamma_- = \tau_{g_2} + \tau_{g_{2s}} - \tau_{g_1}$$

Substituting this expression into equation (A4.7) we get,

$$\delta\tau_g = \frac{A_2^2(\omega)\ \Gamma_- + A_1(\omega)A_2(\omega)\ \cos(\alpha)\ \Gamma_-}{A_1^2(\omega)+A_2^2(\omega)+2A_1(\omega)A_2(\omega)\cos(\alpha)} \tag{A4.9}$$

The additional phase delay caused by the spatial and temporal offset of the secondary source is given by

$$\tau_{p_{2s}} = \frac{\Delta\phi_2(\omega)}{\omega} = \frac{\hat{R}-R}{C(\omega)} + T_{d_2} . \qquad (A4.10)$$

Here R is the distance from the hypocenter of the first signal to the observer and $\hat{R}$ is the distance from the hypocenter of the second signal to the observer. $C(\omega)$ is the phase velocity of the medium. T_{d_2} is the delay in time after the initiation of the first source before the origin of the second source. This time delay can be expressed as an apparent rupture velocity given by $T_{d_2} = \frac{R_s}{V_R}$, where R_S is the separation distance for the two events.

Differentiation of $(\tau_{p_{2s}} \cdot \omega)$ with respect to ω yields the secondary group delay, $\tau_{g_{2s}}$ given by

$$\tau_{g_{2s}} = \frac{\hat{R}-R}{U(\omega)} + T_{d_2} , \qquad (A4.11)$$

where $U(\omega)$ is the group velocity of the medium.

It is seen that calculation of the group delay does not involve any inverse trigonometric functions so that the multivaluedness of the functions is not important. However, this is not the case for the calculation of $\psi(\omega)$. In practice, the values of $\psi(\omega)$ are numerically differenced

to obtain an approximate expression for the group delay. If this approximate group delay is more than one period different from the exact calculated group delay, then a period is added to the phase delay, τ_{p_z}, and the approximate group delay is recalculated. By starting with the phase and group delays of the long period end of the spectrum, the true phase can be unwound from that calculated numerically.

For the addition of many different sources, each offset in time and space with respect to one another, the above calculations are repeated for each source, with the original amplitude and phase spectrum replaced by the partial sum spectra after each individual summation.

Appendix 5

Velocity-Density Models for Local Crustal Corrections

This appendix lists the multi-layered velocity-density models of the crust and upper mantle used in the computation of the local crustal corrections for the WWSSN stations used in the surface wave study in Chapter 5.

The following symbols are employed in the tables:

D = layer thickness in km

Alpha = compressional velocity in km/sec

Beta = shear velocity in km/sec

Rho = density in gram/cm^3.

References for the origin of the data used in the models are given below each table.

San Fernando Crust over Gutenberg Continent

D	Alpha	Beta	Rho
0.50	2.50	1.20	2.10
3.00	3.80	2.50	2.50
2.00	5.50	3.20	2.60
14.50	6.06	3.40	3.00
15.00	6.70	3.80	3.00
13.00	7.96	4.60	3.37
25.00	7.85	4.50	3.39
50.00	7.37	4.21	3.40
75.00	8.00	4.41	3.45
50.00	8.20	4.50	3.47
100.00	8.40	4.60	3.50
100.00	9.00	4.95	3.63
100.00	9.63	5.31	3.89

Source: Jungels (1973), Gutenberg (1944), Wood and Richter (1933), Harkrider *et al.* (1963).

Greenlandic Shield with Ice Cap

D	Alpha	Beta	Rho
2.50	3.93	1.94	0.91
16.50	6.25	3.74	2.80
23.70	6.60	3.85	2.85
37.30	8.05	4.67	3.30
25.00	8.10	4.72	3.30
100.00	8.20	4.54	3.44
100.00	8.30	4.51	3.53
80.00	8.70	4.76	3.60
100.00	9.30	5.12	3.76

Source: Gregersen (1970), Brune and Dorman (1963).

Iceland

D	Alpha	Beta	Rho
4.50	4.70	2.70	2.60
3.50	6.30	3.60	2.80
10.00	6.71	3.90	3.08
10.00	7.38	4.30	3.15
50.00	8.00	4.68	3.30
160.00	7.90	4.40	3.35
100.00	8.20	4.58	3.40
200.00	8.20	4.68	3.40

Source: Tryggvasor. (1962), Båth (1960), Tyggvason and Båth (1961), Tryggvason (1973).

Irish Continental Shelf

D	Alpha	Beta	Rho
0.50	1.52	0.00	1.03
1.50	2.20	1.57	2.55
2.00	5.40	3.18	2.70
20.00	6.10	3.55	2.82
6.00	7.30	4.21	3.10
50.00	8.10	4.61	3.30
100.00	8.10	4.40	3.40
100.00	8.10	4.60	3.55
200.00	8.10	4.89	3.60

Source: Blundell and Parks (1969), Bamford (1971).

Iberian Shield

D	Alpha	Beta	Rho
2.00	3.40	2.00	2.30
18.00	5.90	3.50	2.80
10.00	6.60	3.70	2.90
20.00	7.60	4.50	3.30
30.00	8.10	4.70	3.35
100.00	8.15	4.20	3.40
100.00	8.49	4.77	3.53
100.00	8.81	4.89	3.60
200.00	8.81	4.89	3.60

Source: Payo (1970), Payo (1964).

Mid-Atlantic Ocean

D	Alpha	Beta	Rho
4.50	1.51	0.00	1.03
0.05	1.52	0.15	1.65
0.10	1.60	0.19	1.70
0.10	1.71	0.37	1.79
0.10	1.80	0.53	1.86
2.00	5.00	2.85	2.66
4.50	6.69	3.90	3.06
50.00	3.00	4.68	3.30
160.00	7.90	4.60	3.35
200.00	8.20	4.68	3.40

Source: Ewing (1969), Talwani et al. (1965), Ewing et al. (1966), Katz and Ewing (1956), Officer et al. (1952).

Western America Tectonic

D	Alpha	Beta	Rho
2.50	3.00	1.73	2.40
24.50	6.20	3.58	2.83
13.00	6.80	3.87	2.99
45.00	7.80	4.25	3.30
50.00	8.20	4.38	3.43
100.00	8.20	4.38	3.52
100.00	8.20	4.50	3.57
100.00	8.20	4.70	3.62

Source: Kanamori (1970), Bucher and Smith (1971), Alexander (1963), Ewing and Press (1959), Heezen (1972).

-300-

Pacific Ocean East

D	Alpha	Beta	Rho
3.80	1.51	0.00	1.03
0.01	1.52	0.15	1.65
0.10	1.60	0.19	1.70
0.10	1.71	0.37	1.79
0.10	1.80	0.53	1.86
1.30	5.07	2.88	2.67
5.00	7.20	3.98	2.90
50.00	8.00	4.68	3.30
60.00	7.90	4.60	3.35
100.00	7.90	4.60	3.35
200.00	8.20	4.68	3.40

Source: Piernattei and Nowroozi (1969), Santo (1963), Saito and Takeuchi (1966), Dorman et al. (1960), Raitt (1956), Ewing et al. (1969), Latham and Nowroozi (1968), Kovach and Press (1961).

Pacific Ocean West

D	Alpha	Beta	Rho
5.50	1.51	0.00	1.03
0.10	1.60	0.30	1.65
0.70	5.07	2.88	2.67
4.50	7.20	3.98	2.90
50.00	8.20	4.72	3.30
60.00	7.90	4.40	3.35
100.00	7.90	4.40	3.35
200.00	8.50	4.74	3.40

Source: Piermattei and Nowroozi (1969), Santo (1963), Saito and Takeuchi (1966), Dorman et al. (1960), Raitt (1956), Ewing et al. (1969), Latham and Nowroozi (1968).

Andean

D	Alpha	Beta	Rho
5.00	5.00	2.88	2.67
15.00	6.00	3.46	2.87
25.00	6.60	3.58	2.99
100.00	7.90	4.45	3.30
100.00	8.00	4.40	3.32
100.00	8.00	4.40	3.32
100.00	8.20	4.67	3.38
100.00	8.20	4.68	3.38

Source: James (1971), Fisher and Raitt (1962), Cisternas (1961).

Central Japan

D	Alpha	Beta	Rho
1.00	2.50	1.47	2.50
5.00	5.50	3.18	2.70
16.00	6.00	3.40	2.80
10.00	6.50	3.70	3.00
30.00	7.70	4.37	3.20
100.00	8.00	4.50	3.30
200.00	8.00	4.50	3.30

Source: Kaminuma (1966), Mikumo (1966), Asada and Asano (1972), Kurita (1971).

IV. UPPER-MANTLE SHEAR STRUCTURE

Donald V. Helmberger and Gladys R. Engen

Seismological Laboratory

California Institute of Technology

Pasadena, California 91109

Abstract

This is an attempt at constructing a preliminary shear velocity model compatible with both travel times and waveforms of observed seismograms. Transversely polarized LRSM and WWSS observations are used in this study. SV signatures are demonstrated to be inadequate in identifying triplications because of contamination by PL-coupled shear waves and other P-SV interactions. Well located west coast earthquakes, modeled as shear dislocations, are used as sources. The observed SH travel times are considerably slower than the JB values out to 30 degrees. Select profiles of observed waveforms in conjunction with the travel-times provide the data for model determinations. This is accomplished by fitting the observed waveforms with synthetics.

Synthetics are computed for a number of current models as preliminary attempts at fitting the data. Models containing large, sharp transitions predict strong second arrivals beyond 30°. Models containing low velocity zones between 400 and 700 km predict complicated waveshapes between 20 and 25°. None of the above features are apparent in observed SH waveforms. The final model is relatively smooth and exhibits the same characteristics as the HWB P-model, except that the percentage velocity jump is much less at 400 km and slightly larger at 500 km. The 600 km transition is subdued similar to the P-model.

*Contribution No. 2460 , Division of Geological and Planetary Sciences, California Institute of Technology, Pasadena, California 91109.

INTRODUCTION

Considerable effort in recent years has gone into interpreting upper mantle structure in terms of mineralogic and chemical compositions. A fundamental contribution to this subject was given by Anderson [1967] who suggested that the smooth transition over the 413 to 1000 km depth interval described by the Jeffreys model was incorrect and, that instead, the velocity increased rapidly over two regions near depths of 400 and 600 km. He interpreted these transitions in terms of an olivine-to-spinel phase change at 400 km and a spinel-to-post spinel near 600 km.

More recently, McGetchin and Silver [1970] and others demonstrated the likelihood of other coexisting minerals such as garnet and pryoxene. The rather complicated problem of predicting the changes of seismic properties across phase boundaries involving a multi-mineral assemblage has been attempted by Ahrens [1973]. By varying the temperature and the iron content, assuming a uniform distribution with depth, he was able to match a number of detailed P-models; however, the corresponding predicted S-models bear little resemblance to shear models determined by seismic observations (see Figure 1). Of course, this shear profile can be easily altered in a seemingly infinite number of ways, changing the Fe content as a function of depth being an obvious example. It appears that much of this ambiguity can be eliminated by inverting detailed observed profiles of P and S together. For this reason, we think a serious review of existing shear models is in order.

There are essentially two types of seismic observations used in

shear model determinations, namely, eigenperiods from free oscillations and travel-times of body phases. Earth structure from free oscillations has been studied extensively (see for example Jordan and Anderson, 1973, and Dziewonski and Gilbert, 1972]. These methods are quite successful in determining the gross structure of the earth but probably lack the resolving power necessary for detailed upper mantle modeling. Shear models based on body phases are relatively rare, some major contributors are Kovach and Robinson [1969], Robinson and Kovach [1971], Ibrahim and Nuttli [1967] and Nuttli [1972].

In the Kovach and Robinson [1969] study shear waveforms are not used except to measure the apparent velocity of the starting pulse across the TFO LRSM array. We repeated many of their measurements and found good agreement, but it should be realized that $dt/d\Delta$ values of only the first arrivals does not lead to unique models [for example, see STAN2 of Kovach and Robinson [1969], or Wiggins [1970]. Attempts at measuring the $dT/d\Delta$ values for second arrivals were not particularly successful as pointed out by the above authors.

On the other hand, Ibrahim and Nuttli [1967] and Nuttli [1972] used particle motion diagrams to determine the onset of the multi-arrivals produced by the various triplications. The method is successful in identifying signals, however, it appears, as demonstrated later, that many such arrivals are not true upper mantle shear arrivals but are PL-coupled shear waves and other P-SV crustal arrivals. We will avoid these problems by working exclusively with the SH component although this creates considerable observational difficulties.

4.

SYNTHESIZING BODY WAVES

In order to interpret the rather complicated seismograms we must separate the various contributions due to upper mantle structure from other effects such as source complexity. To facilitate this task we calculate synthetic seismograms assuming various types of sources. The problem can be somewhat simplified by computing the SH component and performing the synthesizing in two stages. First, we compute a step function response of a layered model neglecting the radiation field and surface effects [see Helmberger [1973a] and Gilbert and Helmberger [197]]. Secondly, we generate an effective source function which includes the surface interaction for an event at a given depth and vertical radiation field by assuming a particular ray parameter as discussed by Helmberger [1974]. This procedure allows us to store the relatively expensive step function response and test various source configurations by convolution. Note that this procedure is not particularly accurate for cases where the vertical radiation pattern is varying rapidly at ray parameters appropriate for upper mantle triplications. We will attempt to avoid such sources in this study by relying mostly on strike-slip events. The effective source for the strike-slip and dip-slip cases as a function of epicentral depth is given in Figure 2. The synthetics for depth = 6 km, SH6, are appropriate for the Borrego Mountain Event [see Helmberger, 1974]. Synthetic responses for models STAN3, IN, and US26 are given in Figures 3, 4, and 5 using SH6 as the effective source.

The general features of these profiles are controlled by the relative jumps in velocity at the two transition zones. In Figure 4 the response is almost completely dominated by the two generalized rays

describing this interaction. The reflections are indicated by the peaks and the refractions by the preceding ramps. These two responses cross near 24°. In STAN3, the transition zones are much more subdued and, consequently, the reflected pulses are less obvious. The responses cross near 20° and produce a rather strong synthetic, a very important feature as we will see shortly. The US26 model is a reinterpretation of the travel-time data of Ibrahim and Nuttli [1967] to produce a shear model with transition zones compatible with Johnson's [1967] P velocity structure. The low velocity zone starting at 500 km is required to fit the triplication data. The synthetics from this model are similar to those from model IN. Models STAN3 and IN although derived from essentially the same data bank, differ in travel times, triplication points and waveshape. In fact, their predicted waveshapes are remarkably discordant.

OBSERVATIONS

The observations used in this study are the long-period LRSM and WWSS responses to earthquakes and nuclear events. Figures 6 and 7 show the locations of the various stations and events. Most of the data is relevant to Western United States although we included the Arctic event to sample some of the expected lateral variation. Depth coverage is from about 150 to 1500 km. The region sampled is predominantly that used in the P-wave inversion discussed by Helmberger and Wiggins [1971], and Wiggins and Helmberger [1973].

Samples of the WWSS observations used are given in Figures 8, 9 and 10. Some of the data in Figure 9 has been rotated into SH whereas in Figures 8 and 10 the observations are predominantly SH by choice of

station component. Complete seismograms of some sample LRSM observations, showing the SH pulse emerging from the Love wave are displayed in Figures 11 and 12. Before giving a detailed account of the data we will first discuss the arguments against using SV type motions.

Due to a fortunate set of circumstances the observations from the Borrego Mountain earthquake as recorded in southeastern Canada are naturally polarized into SH(NS) and SV(EW) (Figure 13). As expected from knowledge of the radiation pattern of this strike slip event, we find the first downgoing peak of the SV component to be roughly half the amplitude of SH at SCB and slightly less at STJ. There is good agreement between the SH pulses and the synthetics in Figure 2, SH6. The glich occurring in the 1st peak can be interpreted as the reflection, sS, from the surface [Helmberger, 1974]. Unlike the SH pulses which do not appear to change shape with distances, the SV waveform is elongated and shows a complex behavior as a function of distance, becoming somewhat simpler at $\Delta = 49°$. We interpret this interesting behavior as primarily due to shear-coupled PL waves and not the result of an upper mantle triplication as previous workers have suggested.

Extensive literature exists on the theory of PL waves [see for example Phinney, 1961; Su and Dorman, 1965]. Most PL waves are produced by the coupling between P and SV waves in the crustal waveguide. The type discussed have followed the SV wave, displaying prograde particle motion, and are sometimes called shear-coupled PL waves after Chander et al. [1968]. Particle motion diagrams along with the product trace (Z*EW) used by Ibrahim and Nuttli [1967] and Robinson and Kovach [1971] for arrival identifications are displayed in Figure 13. The onset of the PL phase can be determined by the start of the prograde motion which is especially easy to identify on the SCB record. Arrows mark the beginning of PL on the

various traces. Note the change of period as a function of distance. This type of dispersion has been studied by Chander et al. [1968] and can be used to establish the range at which the PL-coupling occurs. Using their figure on phase velocity versus period indicates that for the SCB observation the coupling occurred near 20°. The PL onset at this range is about 20 sec behind the first arrival and falls on the travel time branch associated with the bottom transition zone as defined by Ibrahim and Nuttli [1967], thus the confusion. In fact, a number of workers have pointed out that for some reason the arrival from the bottom transition is most easily identified on the vertical or radial component, for example see Figure 8 of Kovach and Robinson [1969].

There are other difficulties with working with SV waveshapes such as converted P waves arriving before the direct SV [see Kanasewich et al., 1974]. This feature can be seen in Figure 13 where the S onset is unclear. There is also the problem of waveform distortion caused by receiver function complexity near 20°. That is, when the reciprocal of the SV ray parameter approaches the surface compressional velocity one obtains a complex interaction. The result is a waveshape distortion that is a function of receiver geology and, obviously, difficult to assess. For the above reasons we will rely entirely on SH although this made the data search much more demanding.

Table 1 lists the travel times and events used in this study. The times have been corrected for source depth and instrumental delay. That is, we found that the WWSS instrument has about a two second lag in its transient response compared to three seconds for the LRSM instrument. These values were determined from Figure 2 so they also contain the correction for an assumed Q and source description. The data are plotted in Figure 14. We included the SH data from NTS events as given by Nuttli [1969] and found good agreement.

The data from the Arctic event plot near the Borrego observations at large ranges but plot progressively early moving towards smaller ranges

8.

Figure 14). This feature suggests shallow lateral variations as might be caused by the absence of a low velocity zone. This conclusion is substantiated by the presence of a very strong Sn or high frequency S for ranges less than 20° for shield observations. The waveforms beyond 20° are dominated by deep structure and appear similar to the other observations.

SHEAR MODEL

Our search technique for finding acceptable models was essentially trial and error with the goals of fitting the travel times of Figure 14 and observed high quality SH waveforms. We were guided in this search by similarities in previously generated synthetic seismograms and observed waveforms. For instance, the synthetic at $\Delta = 14°$ for model STAN3 (Figure 3) looks similar to the observations at $\Delta = 15.6°$ displayed in Figure 12. From this comparison, one can roughly determine the relative position of the triplications by examining the step function response of S. Proceeding in this fashion we obtained the models given in Figure 15. The corresponding travel time triplications for the preferred model SHR14 are given in Figure 14 for comparison with the first arrivals. The synthetics are displayed in Figures 16 and 17.

Some of the general features of our final model SHR14 are quite similar to those of STAN3. The two major triplications associated with the 400 and 650 km transition zones still exist although considerably subdued. Reflections from these two zones cross at 20°. The small triplication produced by the velocity jump near 500 km in conjunction with the constructive interference caused by the above cross-over produces extremely strong shear waves near 20°. Note the amplitudes near 20° are nearly an order of magnitude greater than at 30°.

Beyond 20°, the synthetics are dominated by the first arrival with some interference near 28° and with little sign of a second arrival beyond 30°.

The major features of the data that dictate this model are most easily discussed with respect to Figure 14, where the major triplication points and branch crossings are labelled. By fitting the observed waveforms we verify the relative positions of these critical points and associated models. We will devote the remainder of this section to such a detailed comparison.

Comparing the synthetics generated in Figure 16 with observations requires a great deal of patch work due to the lack of a complete profile of data. This situation requires using short profiles of observations with particular source functions; one such comparison is given in Figure 18. By fitting these observations we hope to determine the position of branch DB with respect to branch AB. This determination is especially important since the apparent velocities as measured by first arrivals between BE are considerably higher than the branch DB indicates. First, we note that the two LRSM observations in Figure 11 are very much alike, and that they also agree with the synthetics of Figure 16. We assume that our SH6 source function is appropriate and group these two events together at shorter ranges as given in Figure 18. The dashed line in this figure is the same as branch AB in the travel time plot. The scatter in time picks as given in that plot can be easily seen by examining the observations in Figure 18. There are also considerable differences in waveshapes although some of this effect is probably instrumental as in the case of HRAZ. These distortions or waveshape instabilities could be

caused by lateral structure or perhaps vertical radiation at the source. We will be primarily concerned with the first 50 secs of waveform since the latter portion of the recordings are influenced by shallow structure (Love waves, see Figure 12). It is rather difficult to establish the goodness of fit of the synthetics to the observations without a formal comparison but we will characterize the fit by the relative separation between the major positive peaks as a function of distance. A traced overlay is useful for this purpose. The fit is good although the synthetic first arrival at 16° appears small. Part of this disagreement is caused by inadequate ray modeling in that we neglected the vertical radiation pattern which would enhance the first arrival about 10%.

The waveshapes of the WWSS observations are considerably more interesting than the LRSM examples of Figure 18 although they are rather sparse (see Figures 9 and 10). Most of these events are strike-slip as determined in the literature and can be compared directly with the synthetics of Figure 16. However, their source time histories are expected to be somewhat different due to variations in source depth and dislocation history. The match of the synthetic to observed shapes of Figure 10 is particularly convincing. The interference in the first peak of the synthetic near 17° is observed as well as the apparent pulse broadening. It should also be noted that the SH amplitudes increase rapidly approaching 20° as can be seen by comparing the SH pulse directly with the Love wave onset. It is not uncommon to observe the SH wave stronger than the surface waves near 20°. This strong focusing of energy allows relatively small earthquakes, magnitudes less than 5, to be examined at this range,

for example see the MNN observation of magnitude 5 at 21.4° in Figure 9. Strong amplitudes near 20° can also be observed in Nuttli [1969] data (see his Figure 6). The synthetics from model SHR14 display these features very well. This is not the case for the models IN and US26. STAN 3 predicts strong amplitudes near 20° but the shapes are somewhat discordant, especially at 17°.

Another comparison of LRSM observations with synthetics is given in Figure 19. We assumed a dip-slip source DS14 (see Figure 2) since this effective source looked the most like the observed record at 21° and is compatible with the P wave radiation. We explain the elongated signal at 26° as a combination of branches BC and CD.

Beyond 20° it becomes much more difficult to obtain quality data due to the shear coupled PL wave as discussed earlier. We have to rely on source-receiver geometry to resolve SH and SV since rotating does not seem too effective. The latter portion of the BLC waveshape (Figure 9) is dotted because of possible contamination by strong SV motion (PL problem). The front portion of the recording indicating interference appears accurate since this shape is reproduced by many events such as the observed shape at AAM from the Borrego event. The interference at this range is the only indication of the presence of a triplication. This feature is used to fix the branch HI. Faced with the lack of quality waveshapes at these ranges we attempted to explore the domain of possible models that satisfy the travel time data, the 28° interference, and waveshapes beyond 30° (lack of second arrivals). The model ED42 given in Figure 15 is an attempt at including a low velocity zone between 400 and 600 km. The interference at 28° is relatively easy to produce; however, to fit

the travel times requires that the 600 km transition be very large which produces strong second arrivals beyond 30°. One can suppress this feature by making the first arrival stronger (see Figure 17). The increase in velocity occurring at 850 km produces this effect from 28 to 32° but the problem recurs at 35° (see Figure 20). Synthetics for some other models are included for comparison. We don't feel that the data supports much of a second arrival at these ranges (see Figure 8). This model also predicts complicated waveforms from 20 to 24° as does the models US26 and IN. The first arrival is essentially diffracted energy and is thus small compared to the strong arrival returning from the 600 km transition.

On the other hand, most observations in the range 20 to 24° appear quite simple, for example, see MNN in Figure 9. This observation is especially clear since it occurs on a P-SV radiation node. There is little evidence of any motion on all three components other than SH and Love. However, a small first arrival could still be lost in the background noise. To resolve the question we examined relatively strong signals as displayed in Figure 21. The OXF observation of the Borrego event which is well located has a back azimuth of 274°. The trace goes off scale as expected but there does not appear to be a significant precursor. The same is true for the 5 July event as recorded at MNN. This event is also on a P-SV radiation node. A detailed search for this small arrival proved fruitless. For this reason, we conclude that the strong arrival occurring within the first few seconds of onset at these ranges is coming from the 600 km transition and that, therefore, the velocity must increase below 500 km. Any decrease would move this strong arrival back in time as demonstrated in Figure 17.

DISCUSSION

At this point it seems useful to compare the travel times predicted by the proposed models and discuss the various disagreements with respect to inadequate inversion techniques versus problems of lateral variation. The reduced travel times relative to the Jeffreys-Bullen [1958] tables are displayed in Figure 22 assuming a surface focus. The difference between IN and SHR14 in travel times is due to interpretation of seismograms as mentioned earlier. There does not appear to be any significant difference in S travel times as given by Nuttli [1969] even though we used different events. We think the reason for this is that he used explosions which are well located and we used mainly well located and timed earthquakes such as Borrego Mountain, San Fernando, and Truckee. The travel times predicted from the STAN3 model are substantially faster. However, the change of slope was the actual measurement and the rapid increases at 20 and 24° are also apparent in SHR14. The difference between 17° and 19° is due to the disagreement in branch crossings at B (see Figure 14). The above differences are mostly disagreements in data handling and probably not caused by lateral variation. On the other hand, the travel time difference between SHR14 and the Jeffreys-Bullen [1958] tables could easily be caused by regional structure. That is, the travel times appropriate for midwestern United States may be anomalous compared to Europe and other continental shield regions as suggested by the results from the Arctic event (Figures 8 and 14). There is also the problem of distinguishing between Sn and S when processing shield observations for ranges less than 20°. This may be the reason why the major transition zone at 400 km was not discovered earlier.

RESULTS

We have attempted to determine a shear model that fits both travel times and waveshapes, essentially by trial and error. Fitting fine structure by this method is extremely difficult and somewhat inefficient. For this reason we have tried to produce a starting model for formal inversion now being developed by exploring the possible domains of solutions available. We think SHR14 is a promising candidate. A slightly smoothed version along with a P-model, essentially L14 proposed by Helmberger and Wiggins [1971] that has transition zones in roughly the same locations, is given in Figure 23. We also included a mod 1 proposed by Jordan and Anderson [1967] for comparison. The model parameters are given in Table 2.

In summary, we will review the major structural features of our model that predict realistic seismograms fitting the data. However, due to the data distribution we have determined some parts of the model considerably better than others. We will attempt to convey the features which we think are well constrained by this study. First, the structure near the surface is taken from Stewart and Pakiser [1962] who have observed both $P_n(8.2)$ and $S_n(4.45)$ on the same profile of the Gnome explosion. These velocities are in agreement with measurements made in southern California using quarry blasts presently being investigated. The structure of the low velocity zone, LVZ, is taken from Helmberger [1973]. But since the structure of the LVZ is highly variable in western United States [York and Helmberger, 1973], this model can only be considered as representative. Fortunately, the details of the LVZ

do not greatly influence our upper mantle structure except by slight vertical shifting. The velocity below 200 km is fixed by the ($dT/d\Delta$) values, essentially the slope of the branch AB in Figure 14. This branch appears to start at about 13°, in that the first arrival contains higher frequency than the corresponding Love wave with these high phase velocities (see Figure 9). At larger ranges, the AB branch bends downward indicating a positive velocity gradient. This feature suggests relatively strong first arrivals which can be seen in Figure 18. The overall fit of the synthetics to observed waveforms over the range 14 to 19° is quite good which leads us to conclude that the model from 200 to 450 km is reasonably accurate. (We will postpone questions about how accurate to a later date.) The transition at 500 km is based mostly on amplitude and waveshape data. Since the velocity must increase substantially below 450 km to obey the first arrival times (see Figure 14) we simply added this structure to produce the proper waveshapes and produce the large amplitudes near 20°. At larger ranges the apparent velocity increases rather abruptly (see Figure 14) at about 23°. Similar values were obtained by Kovach and Robinson [1969] as is evident from the slope of the reduced travel time curve displayed in Figure 22. The magnitude of the 600 km transition zone can be determined by the jump in velocity whereas its smoothness can be ascertained by the lack of prominent second arrivals as indicated in Figure 8. At greater depths the velocity approaches B1.

In conclusion, a preliminary model of both compressional and shear velocities is presented. The importance of the seismic parameter,

determined from these velocities, in assessing phase changes versus compositional changes is obvious. We expect the model to be altered somewhat with the addition of wide-band array measurements and better inversion techniques. Nevertheless, a mineralogic interpretation of these combined profiles should prove interesting.

Acknowledments

This research was supported by NSF Grant No. GP 40752, and the Advanced Research Projects Agency at the Department of Defense and was monitored by the Air Force Office of Scientific Research under contracts F44620-72-C-0078 and F44620-72-C-0083.

REFERENCES

Anderson, D. L., Phase changes in the upper mantle, Science, 157, 1165-1173, 1967.

Ahrens, T. J., Petrologic properties of the upper 670 km of the earth's mantle: geophysical implications, Phys. Earth Planet. Interiors, 7, 167-186, 1973.

Chander, R., L. E. Alsop, and J. Oliver, On the synthesis of shear-coupled PL waves, Bull. Seism. Soc. Amer., 58, 1849-1877, 1968.

Dziewonski, A. M., and F. Gilbert, Observations of normal modes from 84 recordings of the Alaskan earthquake of 28 March 1964, Geophys. J. Roy. Astr. Soc., 27, 393-446, 1972.

Gilbert, F. J. and D. V. Helmberger, Generalized ray theory for a layered sphere, Geophys. J. Roy. Astr. Soc., 27, 57-80, 1972.

Helmberger, D. V., Numerical seismograms of long-period body waves from seventeen to forty degrees, Bull. Seismol. Soc. Amer., 63, 633-646, 1973.

Helmberger, D. V., On the structure of the low-velocity zone, Geophys. J. R. Astr. Soc., 34, 251-263, 1973b.

Helmberger, D. V., Generalized ray theory for shear dislocations, Bull. Seismol. Soc. Am., in press.

Helmberger, D. and R. A. Wiggins, Upper mantle structure of Midwestern United States, J. Geophys. Res., 76, 3229-3245,

Ibrahim, A. K., and O. W. Nuttli, Travel-time curves and upper mantle structure from long period S waves, Bull. Seism. Soc. Am., 57, 1063-1092, 1967.

Jeffreys, H., and K. E. Bullen, Seismological Tables, Brit. Assoc., Gray-Milne Trust, 1958.

18.

Johnson, L. R., Array measurements of P velocities in the upper mantle, J. Geophys. Res., 72, 6309-6325, 1967.

Jordan, T. H., and D. L. Anderson, Earth structure from free oscillations and travel times, Geophys. J. Roy. Astr. Soc., in press, 1973.

Julian, B. R., and D.L. Anderson, Travel times, apparent velocities and amplitudes of body waves, Bull. Seismol. Soc. Amer., 58, 339-366, 1968.

Kanasewich, E. R., T. Alpaslan, and F. Hron, The importance of S-wave precursors in shear-wave studies, Bull. Seismol. Soc. Amer., 63, 2167-2176, 1974.

Kovach, R. L., and R. Robinson, Upper mantle structure in the Basin and Range Province, Western North America from the apparent velocities of S waves, Bull. Seismol. Soc. Amer., 59, 1653-1665, 1969.

McGetchen, T. R., and L. T. Silver, Compositional relations in minerals from kimberlite and related rocks in the Moses Rock Dike, San Juan County, Utah, Am. Mineralogist, 55, 1738-1771, 1970.

Nuttli, O. W., Travel times and amplitudes of S waves from nuclear explosions in Nevada, Bull. Seismol. Soc. Amer., 59, 385-398, 1969.

Phinney, R. A., Propagation of leaking interface waves, Bull. Seismol. Soc. Amer., 51, 527-555, 1961.

Robinson, Russell and R. L. Kovach, Shear wave velocities in the earth's mantle, Phys. Earth Planet. Interiors, 5, 30-44, 1972.

Stewart, S. W., and L. C. Pakiser, Crustal structure in Eastern New Mexico interpreted from the Gnome explosion, Bull. Seismol. Soc. Amer., 52, 1017-1030, 1962.

Su, S. S. and J. Dorman, The use of leaking modes in seismogram interpretation and in studies of crust-mantle structure, Bull. Seismol. Soc. Amer., 55, 989-1021, 1965.

[illegible], R. A. and D. Helmberger, Upper mantle structure of Western United States, J. Geophys. Res., 78, 1870-1880, 1973.

Wiggins, R. A., Monte Carlo inversion of body-wave observations, J. Geophys. Res., 74, 3171-3181, 1969.

York, J. E. and D. Helmberger, Low-velocity zone variation in the southwestern United States, J. Geophys. Res., 78, 1883-1886, 1973.

Table 1.

	Date	Location Lat.	Long.	Origin Time h m s	Station	Distance Δ,deg	Travel Time (min & sec)
1	22 Aug 63	42.0 N	126.2 W	09/27/9.3	MNN	24.05	9' 35"
					MDS	26.69	10' 21"
2	31 Mar 64	50.8 N	130.2 W	09/01/30	GOL	20.60	8' 37"
					MDS	28.63	10' 42"
3	5 July 64	26.2 N	110.2 W	19/7/59	BOZ	19.25	8' 8.5"
					COR	21.05	8' 44"
					LON	22.35	9' 11"
					MNN	23.04	9' 19"
					ATL	23.48	9 28"
4	13 July 64	44.7 N	129.9 W	06/47/54	MNN	24.25	9' 40"
5	[illegible] Sept 64	43.5 N	127.5 W	13/59/37	KNUT	12.94	5' 34"
					SGAZ	13.49	5' 46"
					JRAZ	14.81	6' 22"
					LGAZ	15.37	6' 35"
					HRAZ	15.69	6' 45"
					GEAZ	16.42	7' 1"
					RTNM	18.92	7' 59"
6	1 Oct 64	45.7 N	122.8 W	12/31/24.6	JRAZ	14.44	6' 11"
					LGAZ	14.99	6' 25"
					GEAZ	16.04	6' 51"
					RTNM	18.49	7' 50"
					LUB	21.87	8' 59"

Table 1 (continued)

	Date	Location Lat.	Location Long.	Origin Time h m s	Station	Distance Δ,deg	Travel Time (min & sec)
7	22 [illegible]	31.9 N	117.1 W	20/54/35.3	MNN	22.70	9' 12"
					FLO	22.81	9' 15"
					MDS	24.38	9' 40"
8	22 Sept 66	59.4 N	120.1 W	16/41/1.7	FSJ	15.31	6' 40"
					JCT	18.80	7' 59"
					FFC	19.60	8' 4"
					MDS	23.04	9' 19"
9	23 Nov 67	80.2 N	1. W	13/42/02	UME	17.48	7' 17"
					KON	20.90	8' 33"
					NUR	21.16	8' 39"
					FBC	24.29	9' 36"
					CMC	27.75	10' 31"
					BLC	28.33	10' 43"
					YKC	32.78	11' 53"
					LOR	33.10	11' 58"
					FCC	33.27	11' 57"
					STJ	37.17	13' 8"
					PTO	39.29	13' 25"
					TOL	40.46	13' 50"
					SES	43.99	14' 38"
					PHC	45.93	15' 12"
					PNT	46.27	15' 16"

Table 1 (continued)

No.	Date	Location Lat.	Location Long.	Origin Time h m s	Station	Distance Δ,deg	Travel Time (min & sec)
1[illegible]	28 Dec 67	44.2 N	128.8 W	06/26/16	DUG	12.52	5' 24"
					SES	13.56	5' 48"
					EDM	13.61	5' 50"
					GOL	17.98	7' 36"
					TUC	18.43	7' 50"
					ALQ	19.5	8' 13"
					YKC	20.12	8' 18"
					COL	23.30	9' 22"
					LUB	23.37	9' 27"
					CMC	24.77	9' 45"
[illegible]	9 Apr 68	33.1 N	116.1 W	02/28/59	LON	14.30	6' 9"
					OXF	22.21	9' 5"
					ATL	26.51	10' 13"
					AAM	27.13	10' 22"
					BLA	29.35	10' 59"
					SCB	30.55	11' 21"
					SCP	31.31	11' 36"
					OTT	33.26	12' 1"
					BLC	33.62	12' 12.5
					OGD	33.78	12' 12.5"
					WES	36.25	12' 51.5"
					SFA	36.83	12' 56"
					SCH	40.55	13' 50"
					HAL	41.81	14' 12"

Table 1 (continued)

No.	Date	Location Lat.	Long.	Origin Time h m s	Station	Distance Δ, deg	Travel Time (min & sec)
12	26 Nov 70	43.78 N	127.45 W	3/11/43	GOL	16.96	7' 17"
					ALQ	18.44	7' 49"
					JCT	25.59	10' 2"
					FLO	28.14	10' 40"
					OXF	30.69	11' 24"
13	9 Feb 71	34.41 N	118.40 W	17/00/42	DAL	18.06	7' 38"
					FLO	22.88	9' 15"
					SHA	23.87	9' 34.5"
14	9 Aug 71	49.6 N	129.5 W	5/50/5.8	LHC	26.16	10' 5"

Table II

Depth	V_p	V_s	ϕ	σ
25	6.80	3.69	28.09	.291
50	8.20	4.45	40.84	.291
75	7.81	4.30	36.34	.282
100	7.92	4.43	36.56	.272
125	8.02	4.44	38.04	.279
150	8.14	4.46	39.74	.285
175	8.24	4.48	41.14	.290
200	8.32	4.50	42.22	.293
225	8.36	4.52	42.65	.293
250	8.41	4.54	43.25	.294
275	8.45	4.56	43.68	.294
300	8.49	4.58	44.11	.294
325	8.53	4.62	44.30	.292
350	8.57	4.65	44.62	.291
375	8.63	4.72	44.77	.286
400	9.10	4.98	49.74	.286
425	9.53	5.12	55.87	.297
450	9.57	5.17	55.95	.293
475	9.62	5.18	56.77	.295
500	9.71	5.23	57.81	.295
525	9.92	5.39	59.67	.290
550	10.07	5.43	62.09	.295
575	10.13	5.43	63.31	.299
600	10.19	5.48	63.80	.296

Table II (continued)

Depth	V_p	V_s	ϕ	σ
625	10.29	5.59	64.22	.290
650	10.41	5.76	64.13	.279
675	10.74	5.94	68.30	.279
700	10.93	6.07	70.34	.277
725	10.98	6.09	71.11	.277
750	11.02	6.12	71.50	.277
775	11.06	6.15	71.90	.276
800	11.11	6.19	72.35	.274
825	11.15	6.23	72.57	.273
850	11.19	6.26	72.97	.272
875	11.23	6.29	73.36	.271
900	11.27	6.32	73.76	.270
925	11.31	6.34	74.32	.270
950	11.35	6.36	74.89	.271
975	11.39	6.38	75.46	.271
1000	11.44	6.40	76.26	.272
1025	11.49	6.42	77.07	.273
1060	11.53	6.43	77.82	.274

FIGURE CAPTIONS

Figure 1. Comparison of models proposed from shear wave observations with a predicted shear profile based on theoretical mineralogic considerations.

Figure 2. Effective source function containing surface interaction as a function of epicentral depth; contains time history, instrument and absorption.

Figure 3. Synthetic profile based on STAN3 assuming SH6 as the effective source function.

Figure 4. Synthetic profile based on IN assuming SH6 as the effective source function.

Figure 5. Synthetic profile based on US26 assuming SH6 as the effective source function.

Figure 6. Map locating stations and events. Events are identified in Table 1 according to date (see Table 1).

Figure 7. Map locating an event in the Greenland Sea relative to stations using an Arctic projection.

Figure 8. Profile of observations from events 23 Nov 67 (Arctic) and 9 Apr 68 (Borrego).

Figure 9. Sample recording of WWSS observations of simple events. Note that FBC and BLC are of the Arctic event.

Figure 10. Examples of large amplitude arrivals near 20°.

Figure 11. LRSM observations of two simple events off Oregon as recorded by the same station.

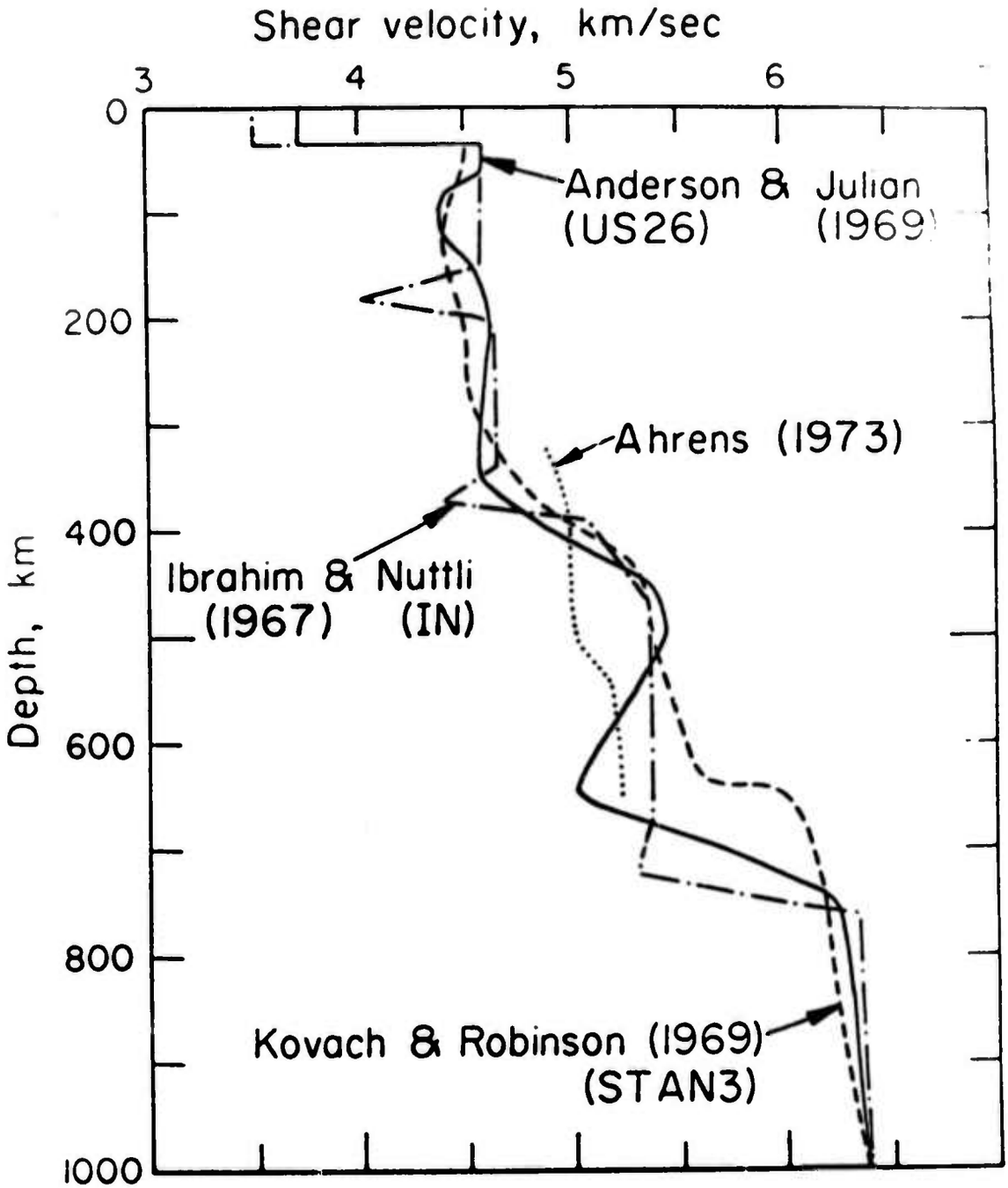
Shear velocity, km/sec
3
4
5
6
0
200
400
600
800
1000
Depth, km
Anderson & Julian
(US26)
(1969)
Ahrens (1973)
Ibrahim & Nuttli
(1967)
(IN)
Kovach & Robinson (1969)
(STAN3)

Fig. 1

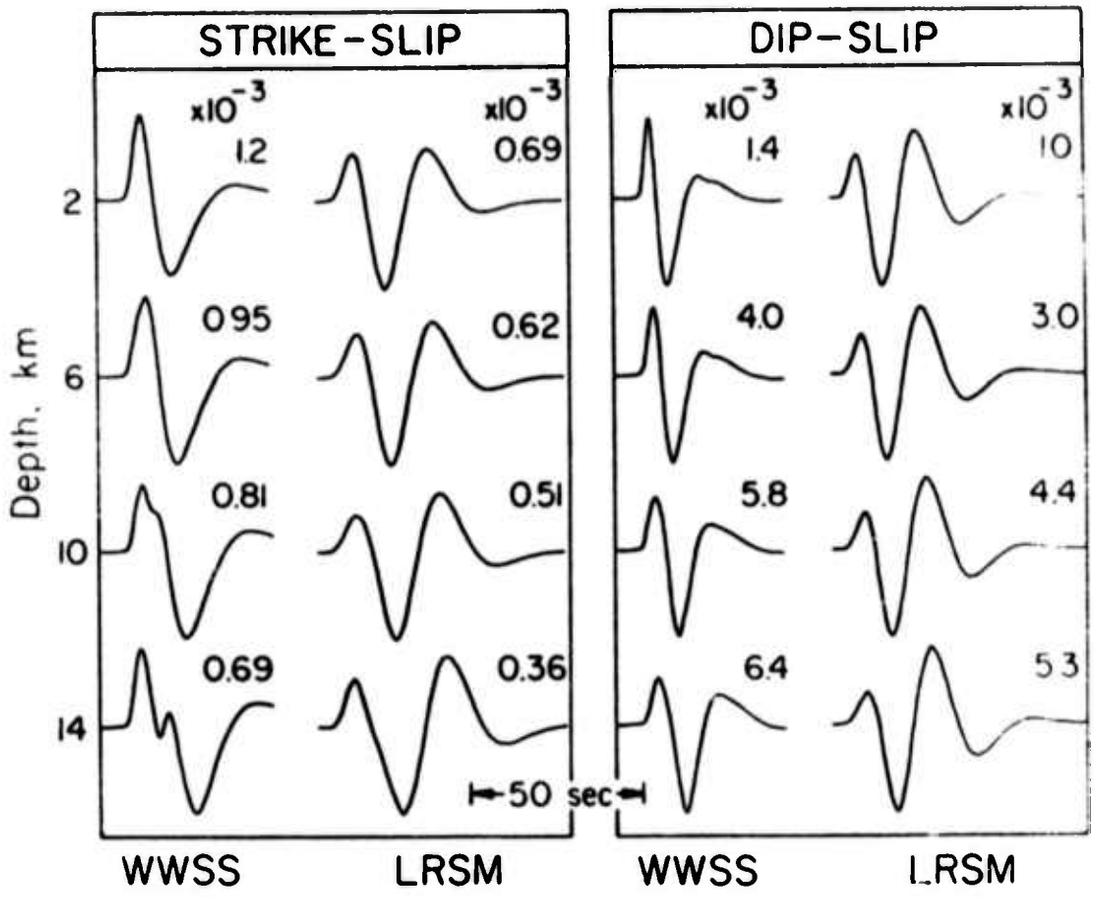
STRIKE-SLIP
DIP-SLIP
x10^-3
1.2
0.69
1.4
10
0.95
0.62
4.0
3.0
0.81
0.51
5.8
4.4
0.69
0.36
6.4
5.3
Depth, km
2
6
10
14
50 sec
WWSS
LRSM
WWSS
LRSM

Fig. 2

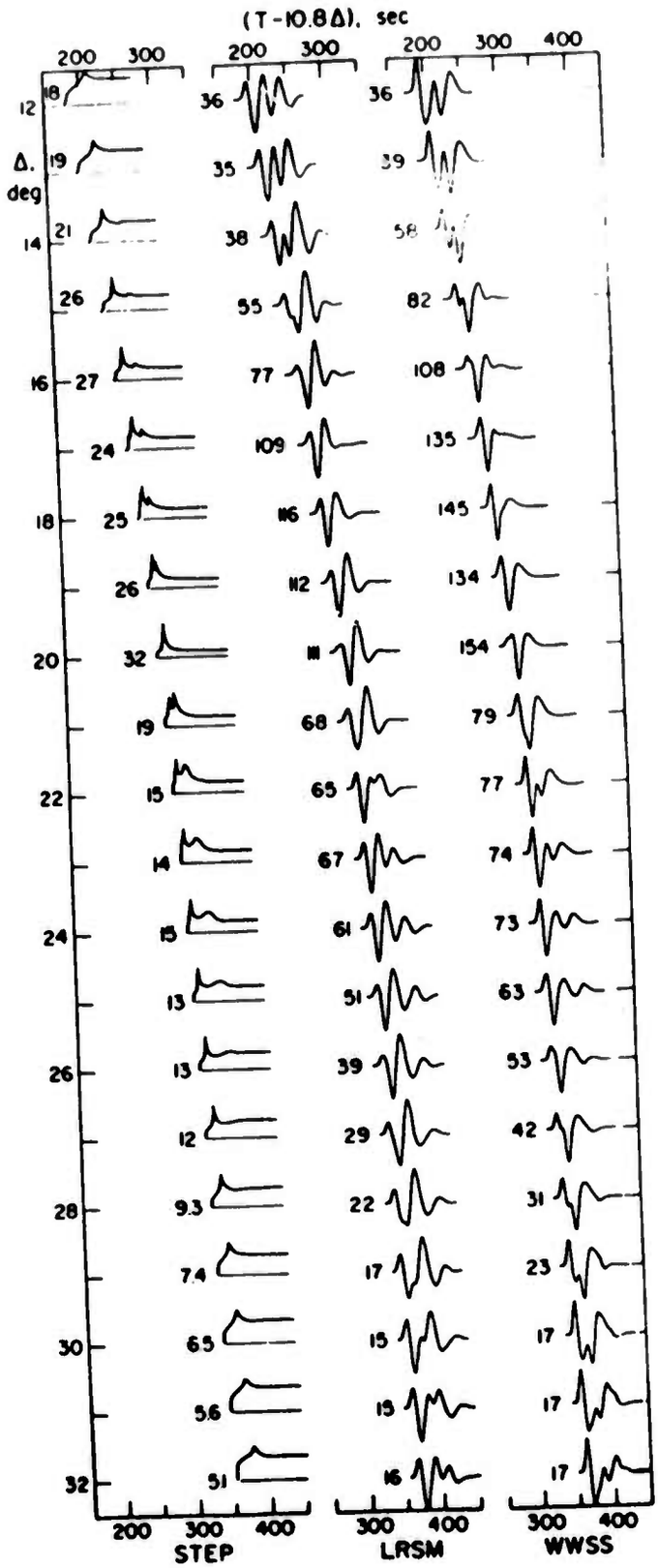
(T-10.8Δ), sec
200 300
200 300
200 300 400
Δ, deg
12
14
16
18
20
22
24
26
28
30
32
18
19
21
26
27
24
25
26
32
19
15
14
15
13
13
12
9.3
7.4
6.5
5.6
5.1
36
35
38
55
77
109
116
112
111
68
65
67
61
51
39
29
22
17
15
13
16
36
39
58
82
108
135
145
134
154
79
77
74
73
63
53
42
31
23
17
17
17
200 300 400
STEP
300 400
LRSM
300 400
WWSS

Fig. 3

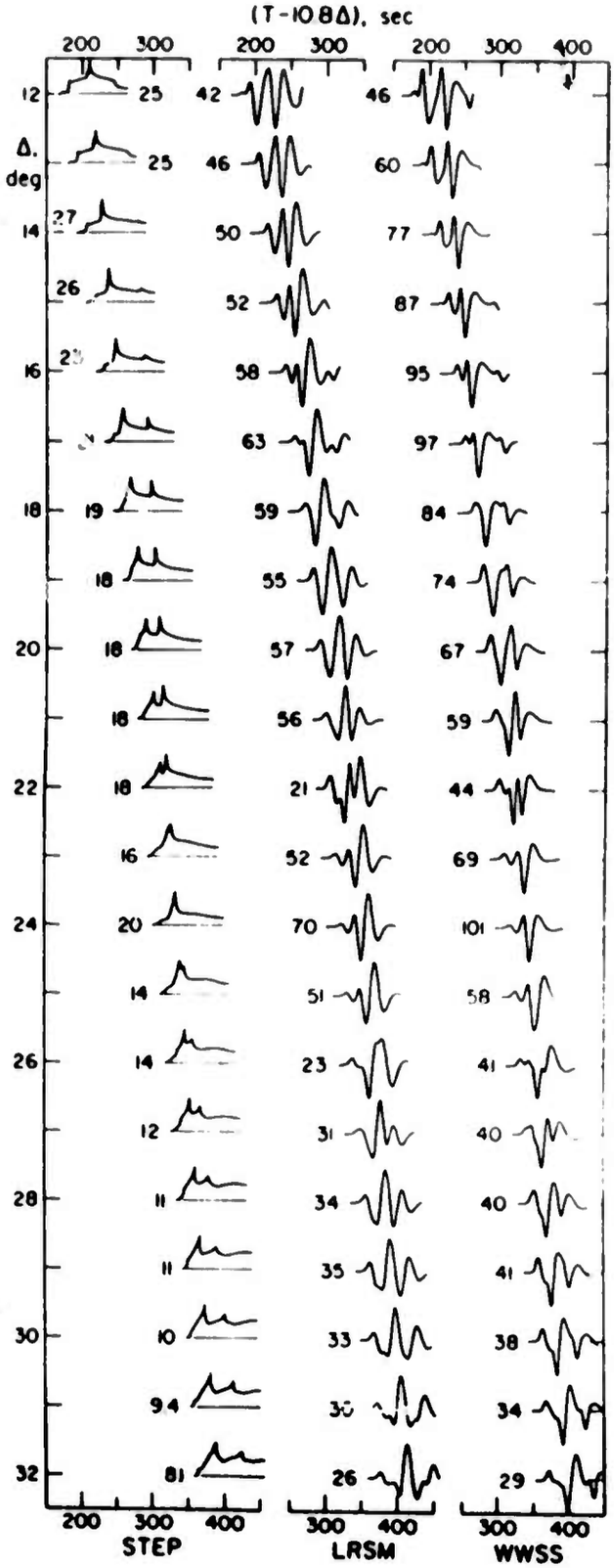
(T-10.8Δ), sec
200 300
200 300
200 300 400
Δ, deg
12
14
16
18
20
22
24
26
28
30
32
25
25
27
26
23
19
18
18
18
16
20
14
14
12
11
11
10
9.4
8.1
42
46
50
52
58
63
59
55
57
56
21
52
70
51
23
31
34
35
33
30
26
46
60
77
87
95
97
84
74
67
59
44
69
101
58
41
40
40
41
38
34
29
200 300 400
STEP
300 400
LRSM
300 400
WWSS

Fig. 4

WWSS
LRSM
STEP
(T-10.8Δ), sec
Δ, deg

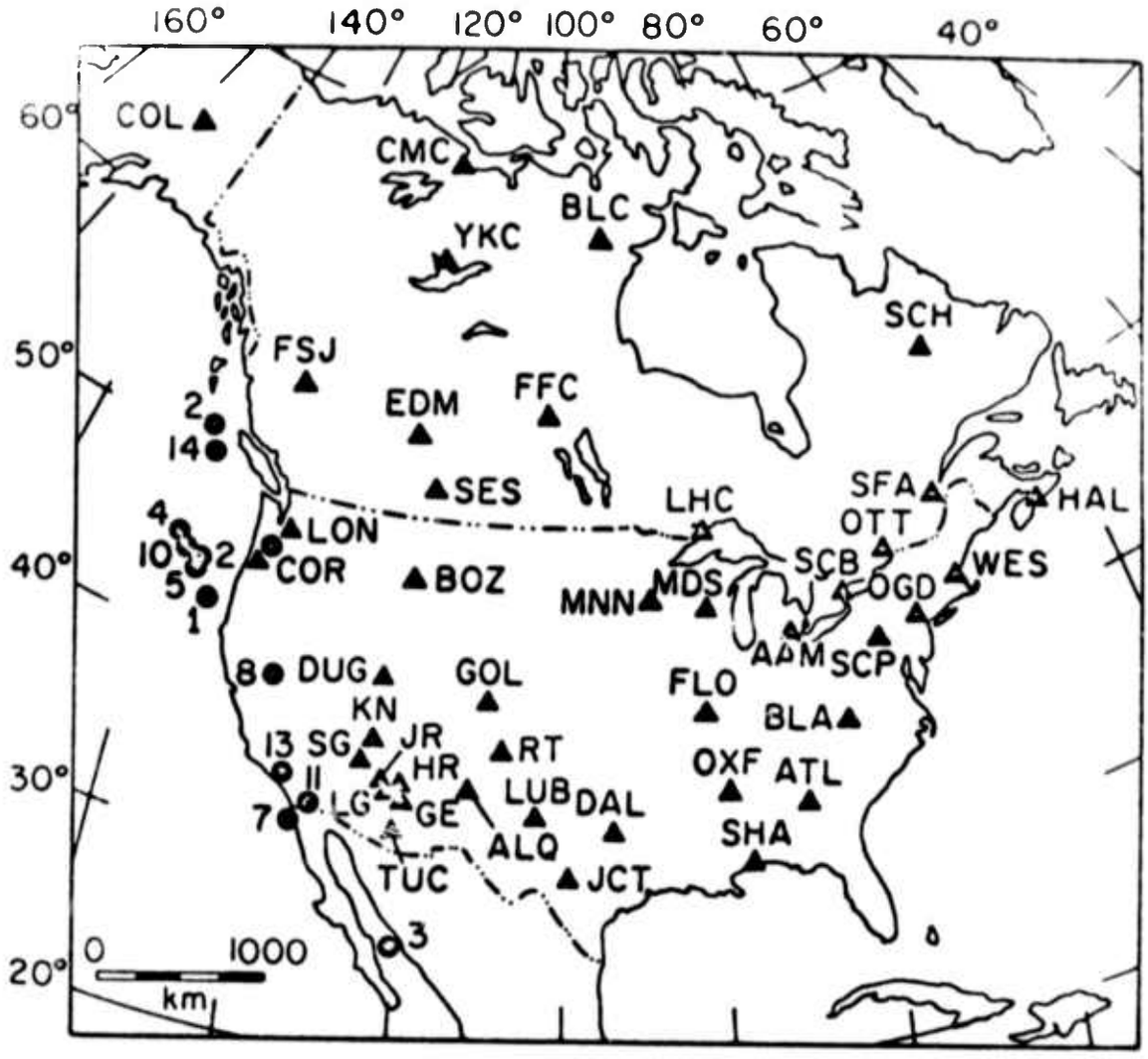
160°
140°
120°
100°
80°
60°
40°
60°
50°
40°
30°
20°
COL
CMC
BLC
YKC
SCH
FSJ
EDM
FFC
SES
LHC
SFA
HAL
OTT
LON
COR
BOZ
SCB
WES
OGD
MNN
MDS
AAM
SCP
DUG
GOL
FLO
KN
BLA
SG
JR
RT
HR
OXF
ATL
LG
GE
LUB
DAL
ALQ
SHA
TUC
JCT
1
2
3
4
5
7
8
10
11
13
14
0
1000
km

Fig. 6

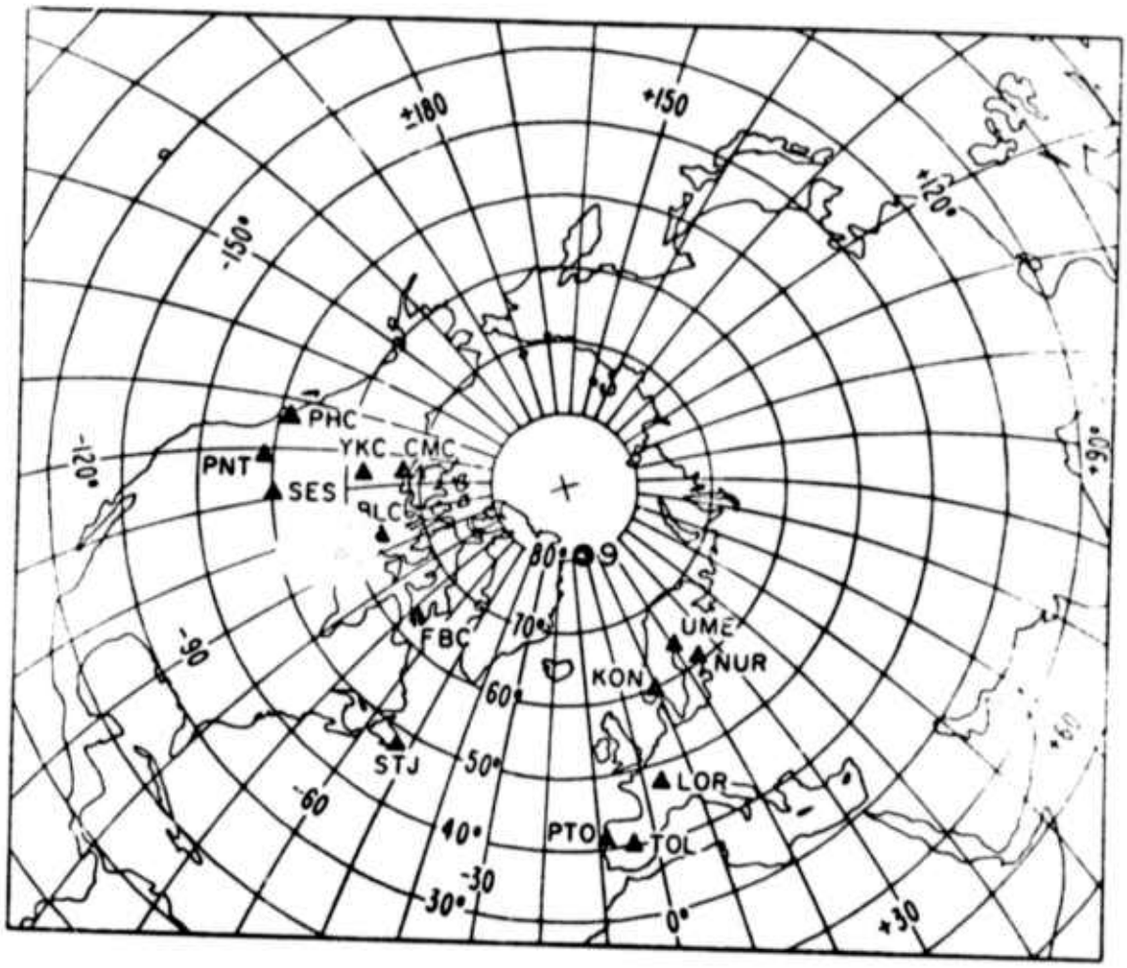
±180
+150
+120
-150
-120
+90
-90
-60
+60
-30
+30
0
80
70
60
50
40
30
PHC
YKC
CMC
PNT
SES
ALC
FBC
STJ
KON
UME
NUR
LOR
PTO
TOL

Fig. 7

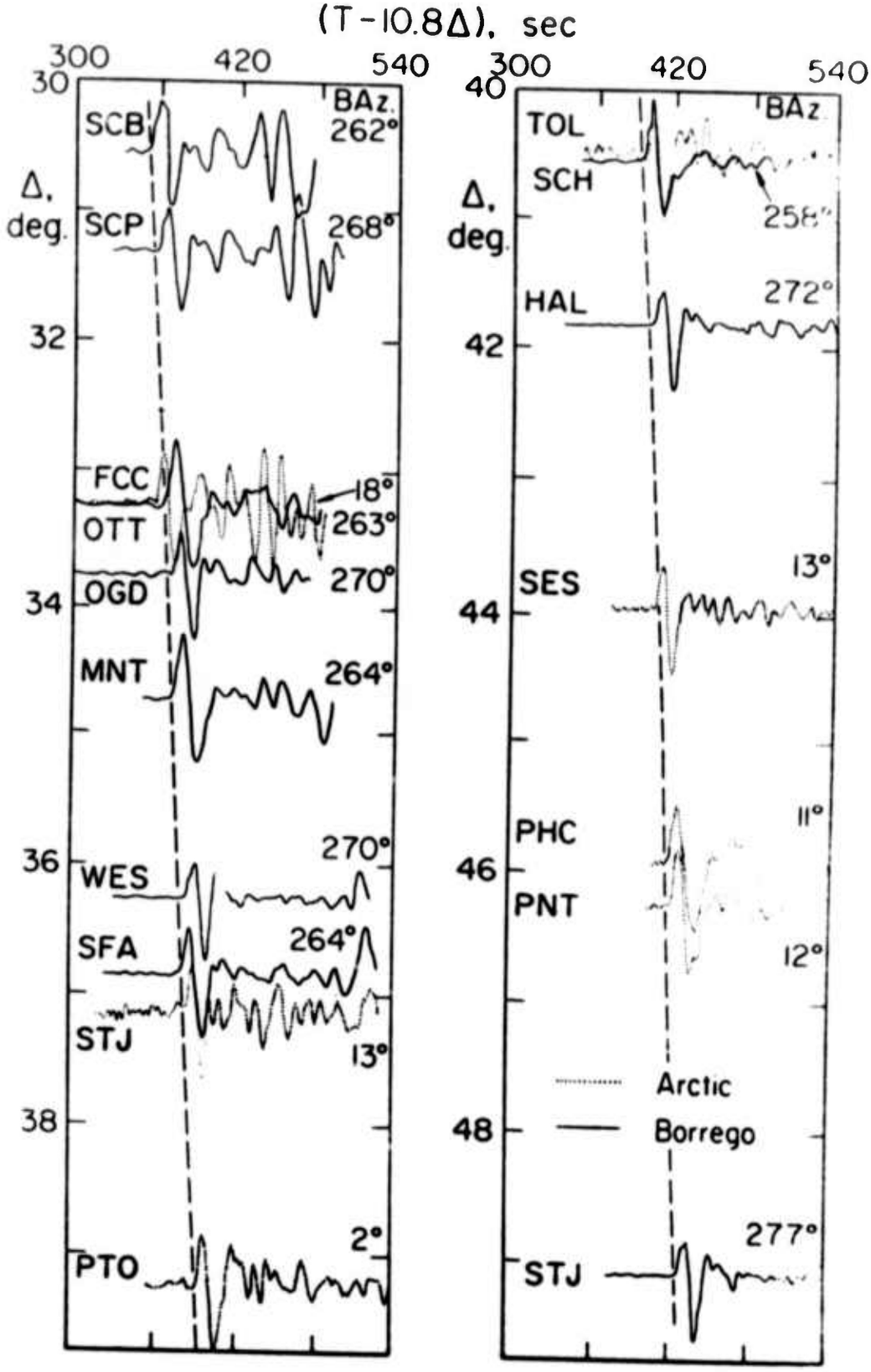
(T-10.8Δ), sec
300
420
540
Δ, deg.
30
32
34
36
38
BAz.
SCB
262°
SCP
268°
FCC
18°
OTT
263°
OGD
270°
MNT
264°
WES
270°
SFA
264°
STJ
13°
PTO
2°
40
42
44
46
48
TOL
SCH
HAL
272°
SES
13°
PHC
11°
PNT
12°
Arctic
Borrego
277°
STJ

Fig. 8

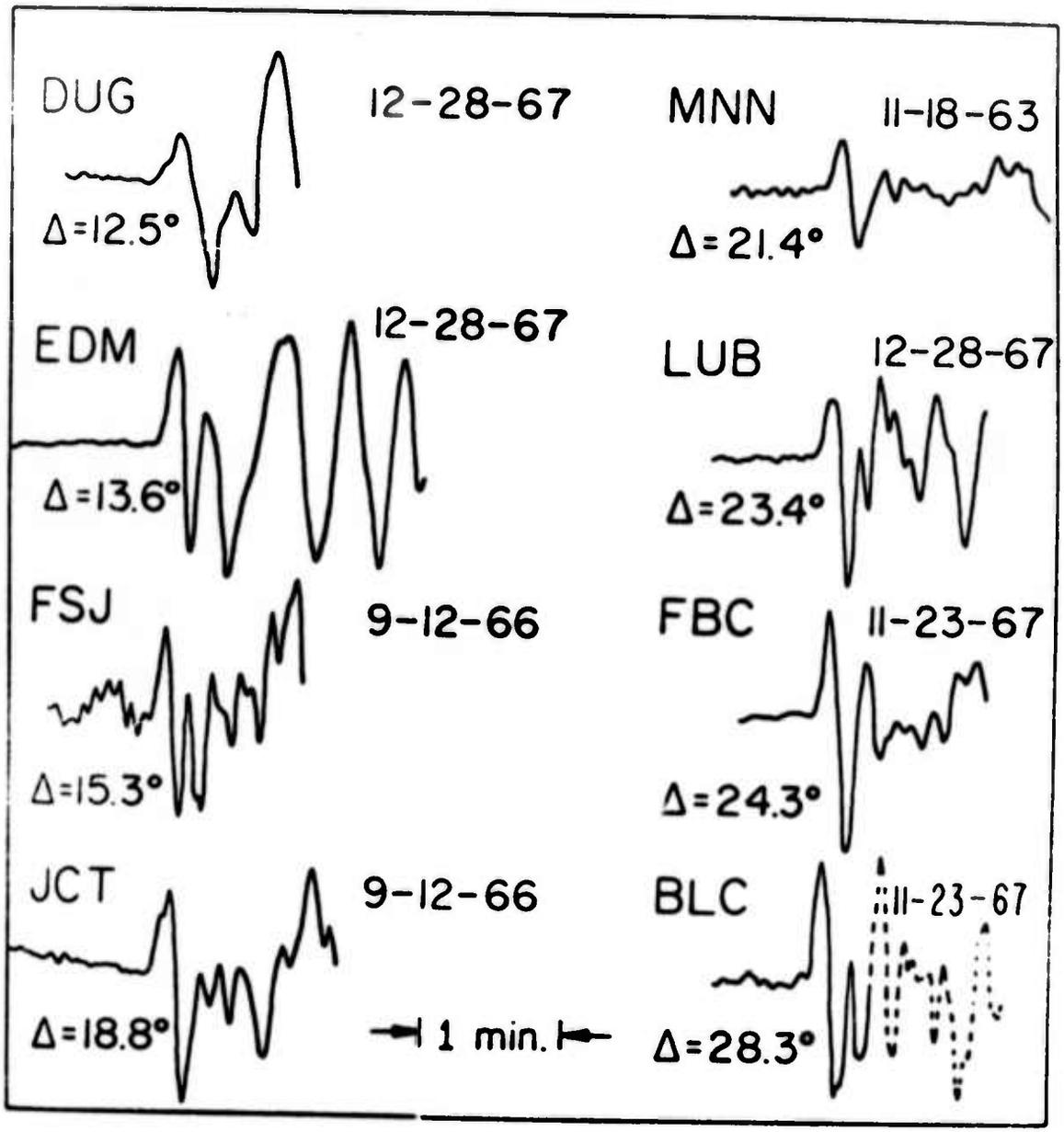
DUG
12-28-67
Δ=12.5°
MNN
11-18-63
Δ=21.4°
EDM
12-28-67
Δ=13.6°
LUB
12-28-67
Δ=23.4°
FSJ
9-12-66
Δ=15.3°
FBC
11-23-67
Δ=24.3°
JCT
9-12-66
Δ=18.8°
1 min.
BLC
11-23-67
Δ=28.3°

Fig. 9

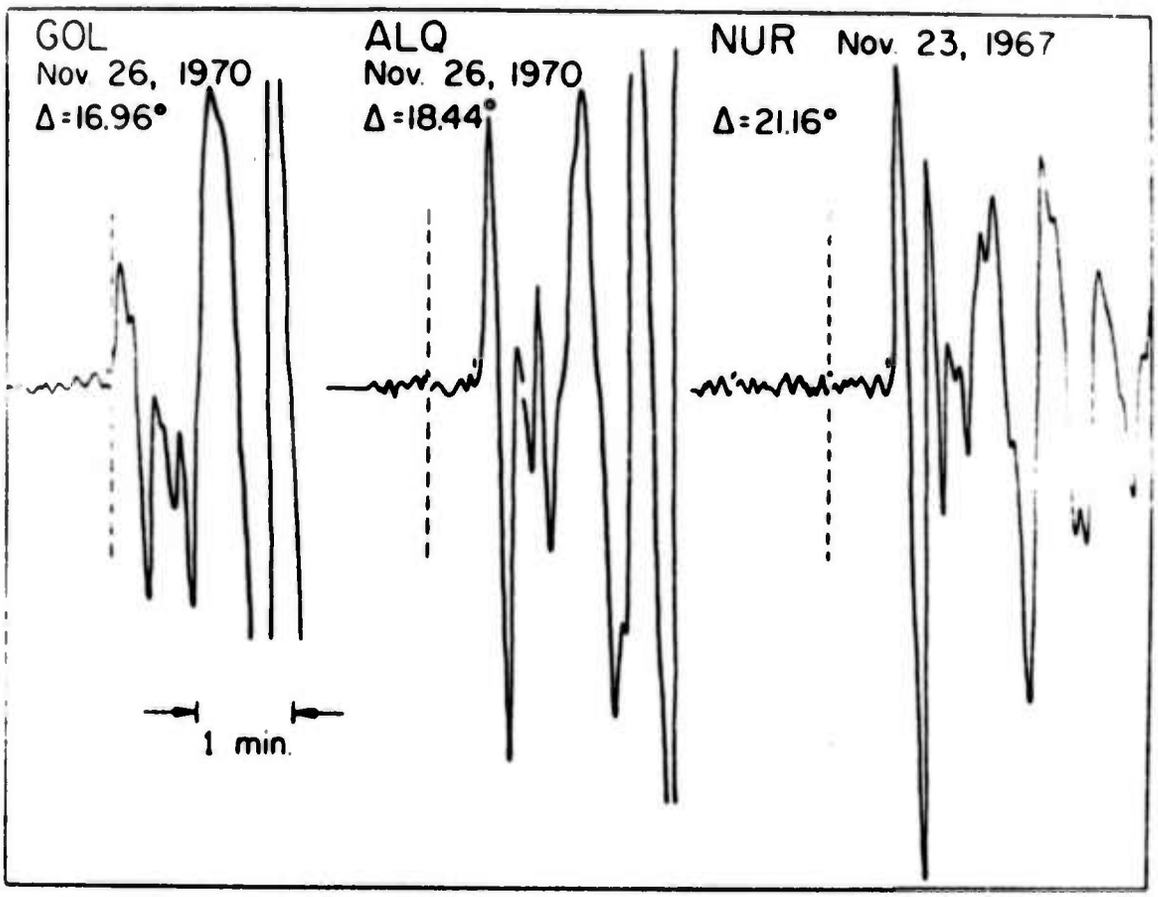
GOL
Nov 26, 1970
Δ=16.96°
ALQ
Nov. 26, 1970
Δ=18.44°
NUR Nov. 23, 1967
Δ=21.16°
1 min.

Fig. 10

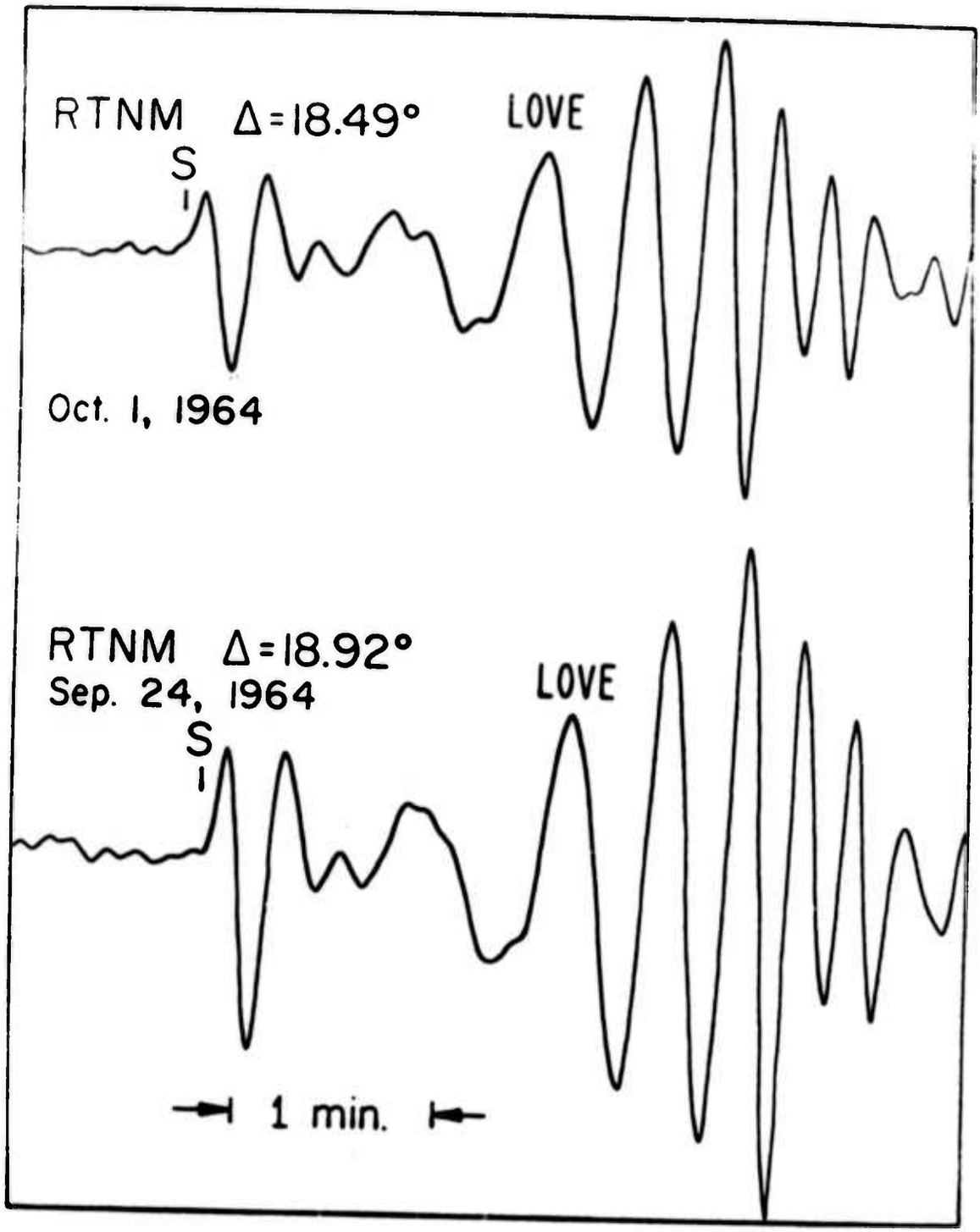

Fig. 11

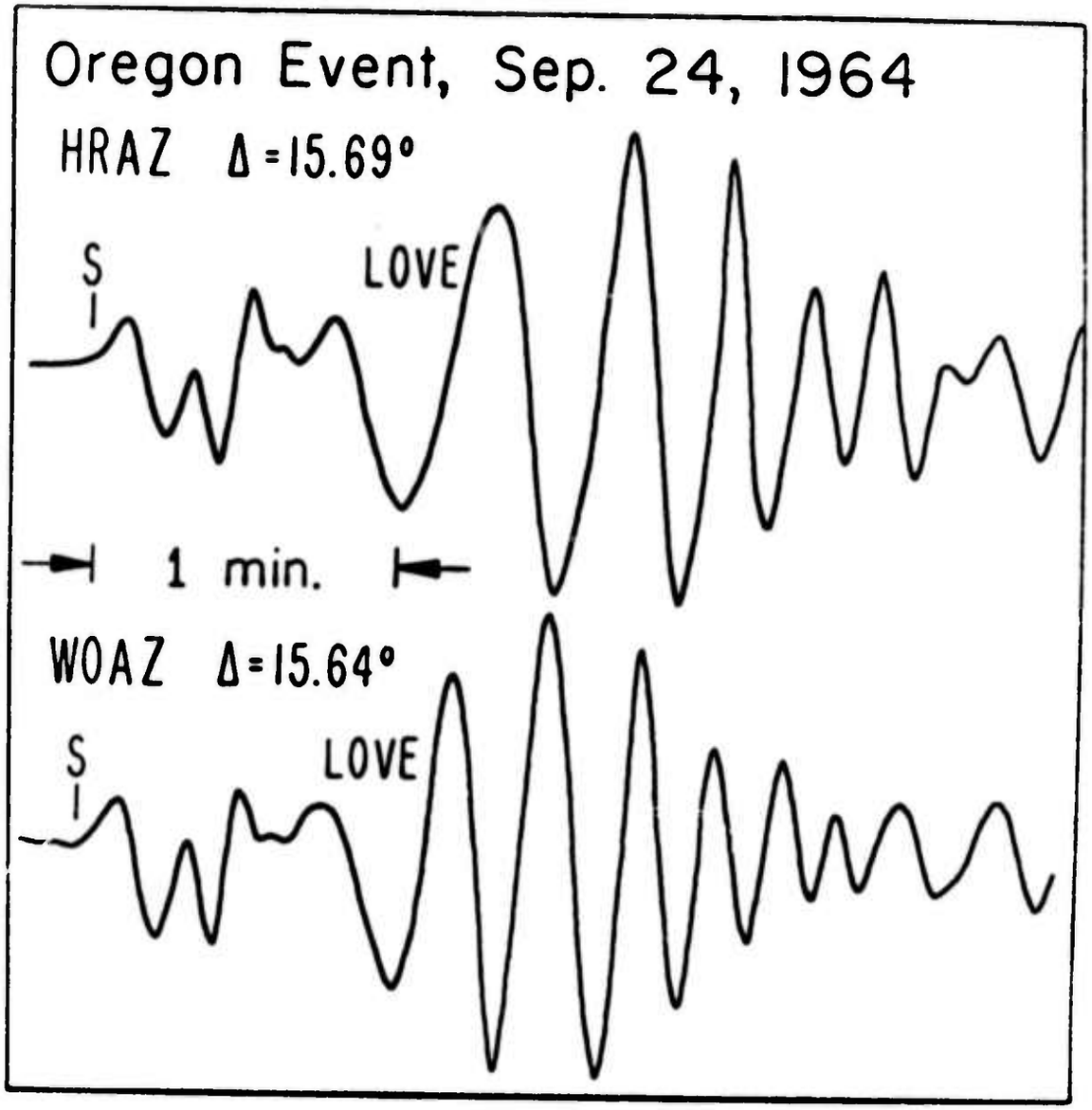
Oregon Event, Sep. 24, 1964
HRAZ Δ=15.69°
S
I
LOVE
1 min.
WOAZ Δ=15.64°
S
I
LOVE

Fig. 12

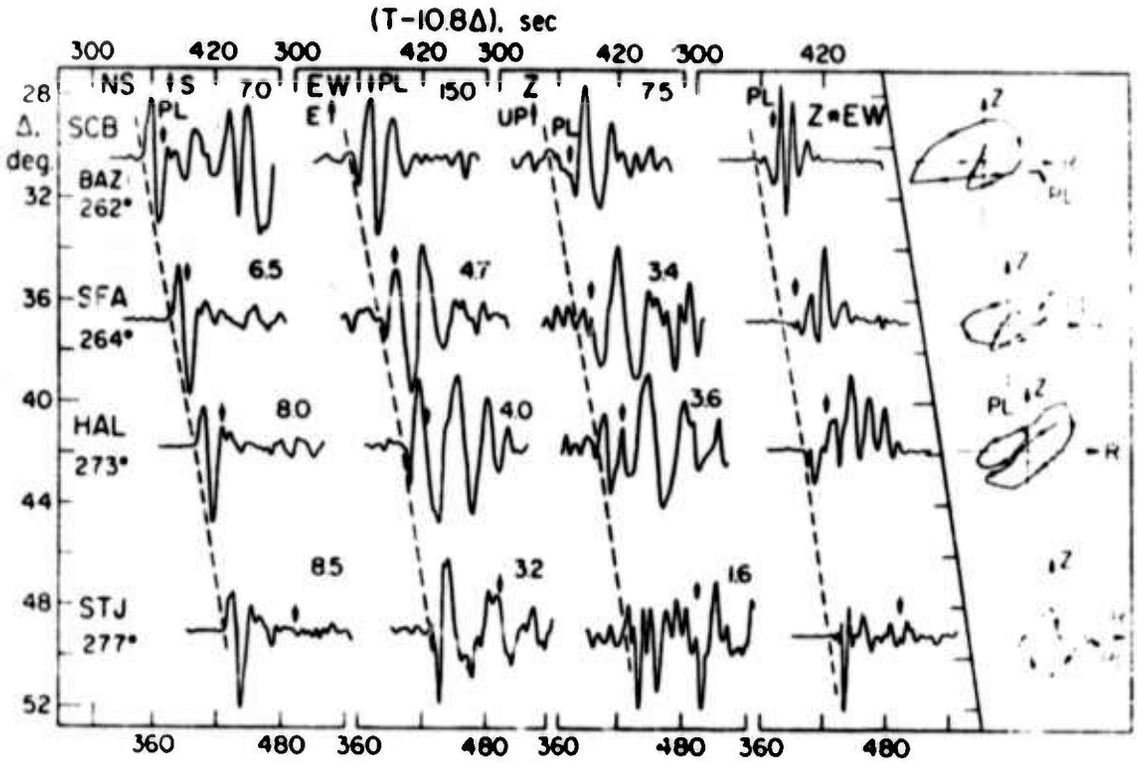
(T-10.8Δ), sec
300
420
300
420
300
420
300
420
28
Δ, deg
32
36
40
44
48
52
NS
S
70
EW
E
PL
150
Z
UP
75
PL
Z=EW
SCB
BAZ 262°
SFA 264°
HAL 273°
STJ 277°
6.5
4.7
3.4
8.0
4.0
3.6
8.5
3.2
1.6
360
480
360
480
360
480
360
480

Fig. 13

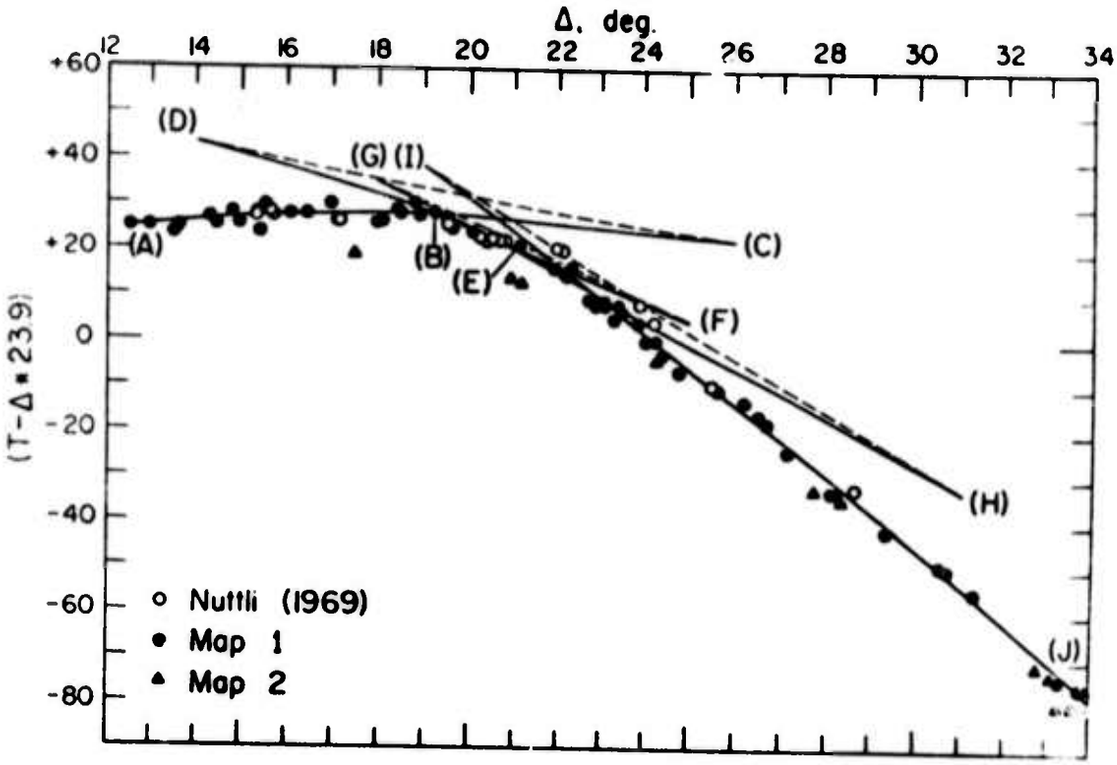
Δ, deg.
12
14
16
18
20
22
24
26
28
30
32
34
+60
+40
+20
0
-20
-40
-60
-80
(T-Δ*239)
(A)
(B)
(C)
(D)
(E)
(F)
(G)
(H)
(I)
(J)
Nuttli (1969)
Map 1
Map 2

Fig. 14

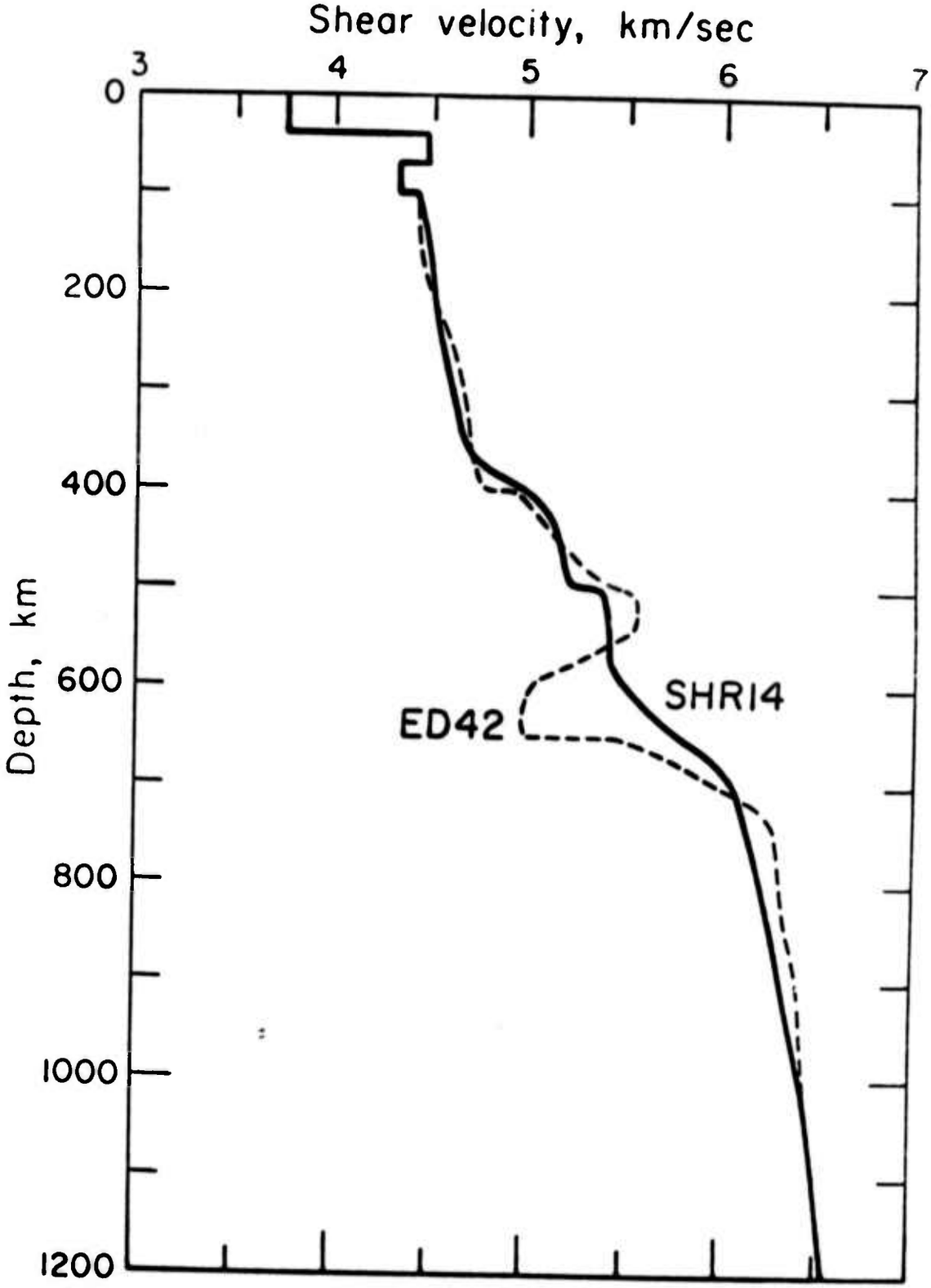
Shear velocity, km/sec
3
4
5
6
7
0
200
400
600
800
1000
1200
Depth, km
ED42
SHR14

Fig. 15

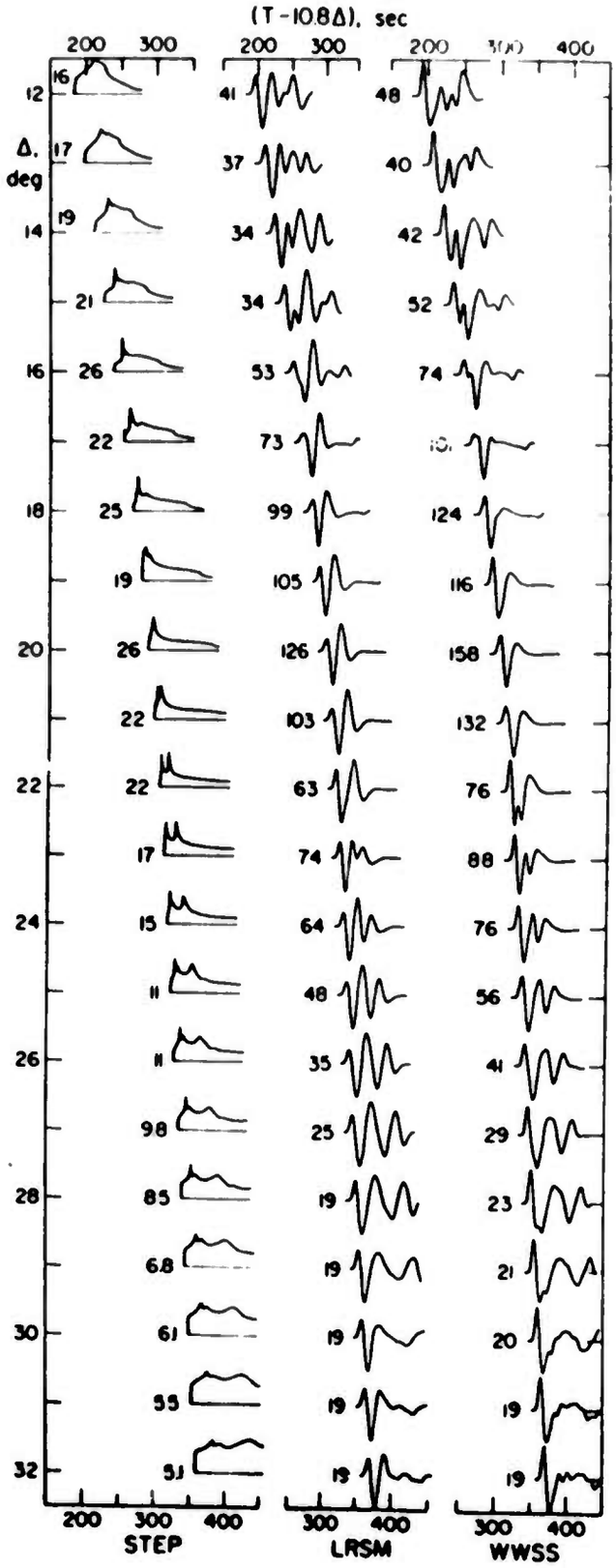
(T-10.8Δ), sec
200 300
200 300
200 300 400
Δ, deg
12
14
16
18
20
22
24
26
28
30
32
16 41 48
17 37 40
19 34 42
21 34 52
26 53 74
22 73
25 99 124
19 105 116
26 126 158
22 103 132
22 22 63 76
17 74 88
15 64 76
11 48 56
11 35 41
98 25 29
85 19 23
68 19 21
61 19 20
55 19 19
51 19 19
200 300 400
STEP
300 400
LRSM
300 400
WWSS

Fig. 16

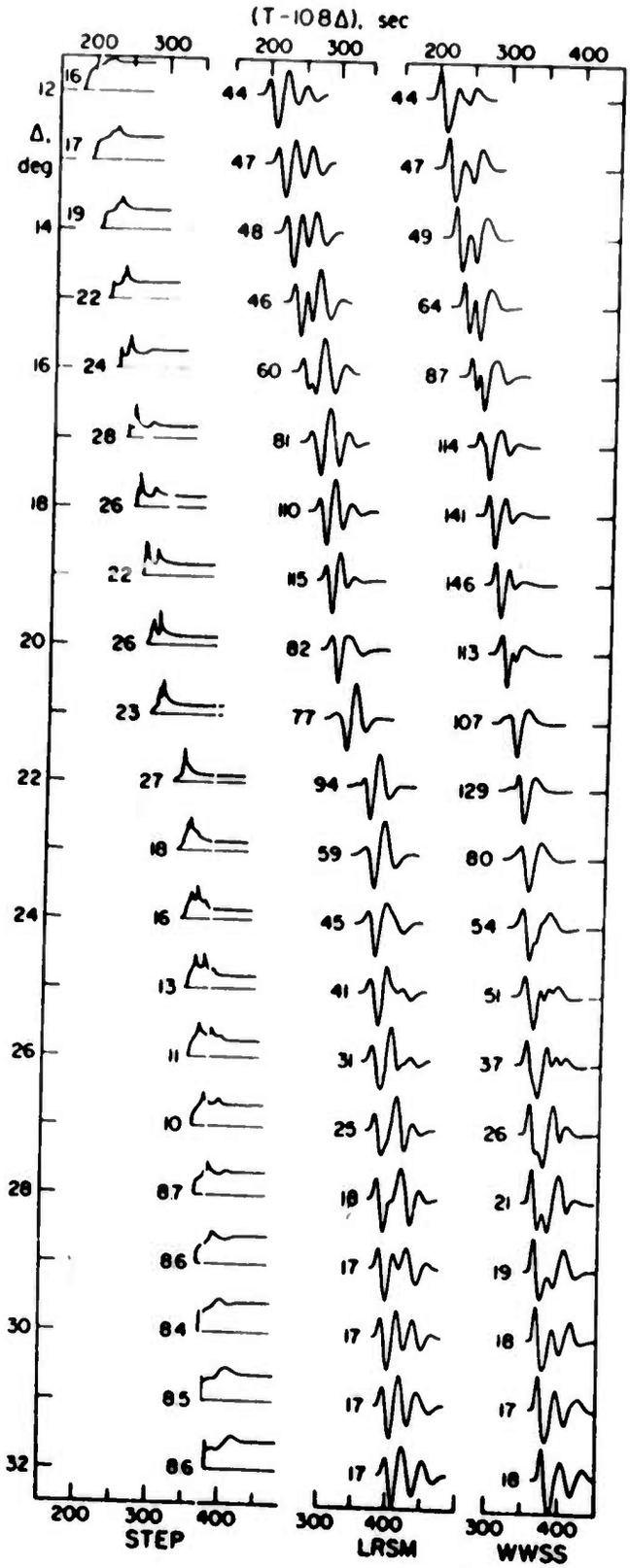
(T-10Δ), sec
200 300
200 300
200 300 400
Δ, deg
12
14
16
18
20
22
24
26
28
30
32
16
17
19
22
24
28
26
22
26
23
27
18
16
13
11
10
8.7
8.6
8.4
8.5
8.6
44
47
48
46
60
81
110
115
82
77
94
59
45
41
31
25
18
17
17
17
44
47
49
64
87
114
141
146
113
107
129
80
54
51
37
26
21
19
18
17
18
200 300 400
STEP
300 400
LRSM
300 400
WWSS

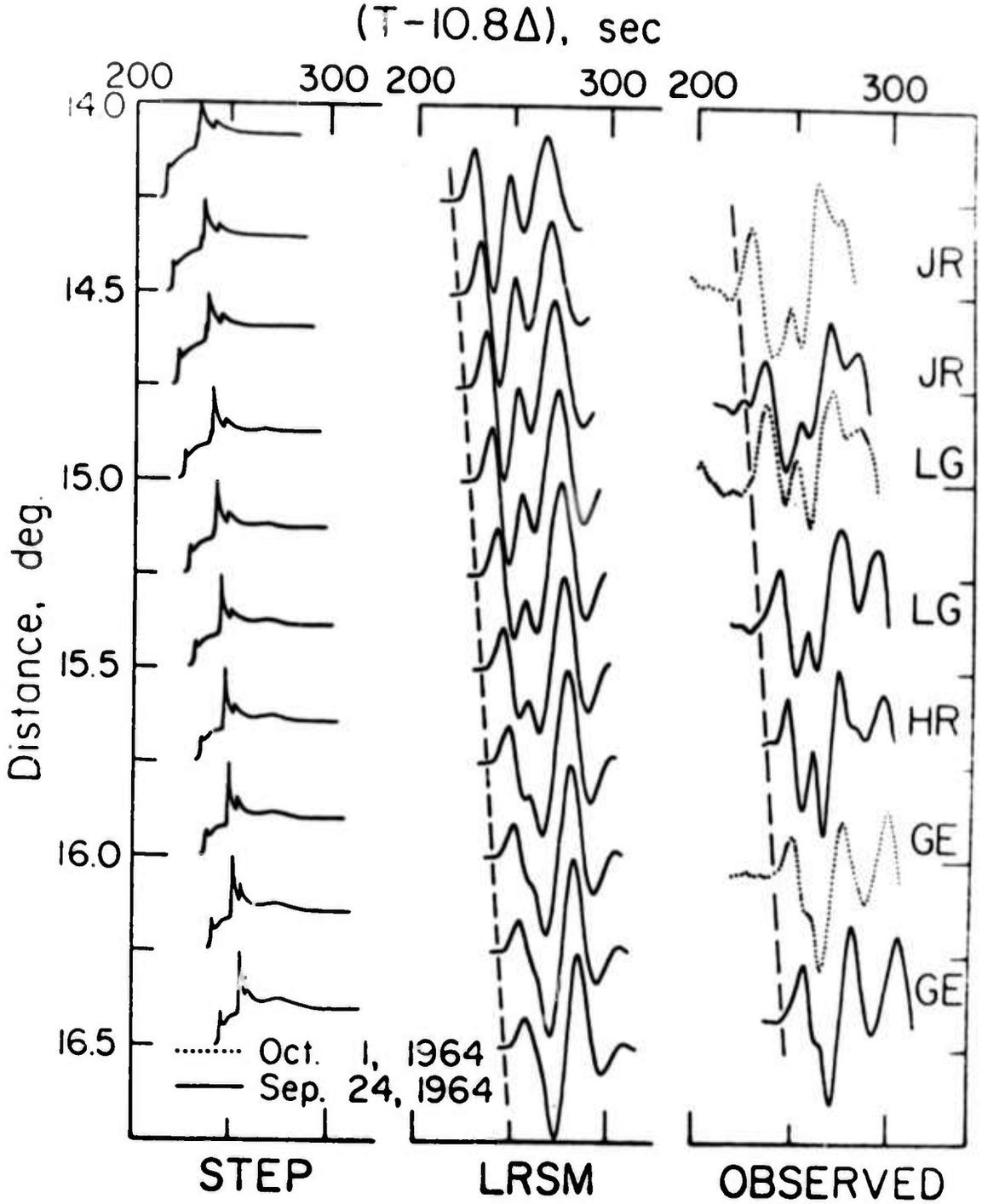
(T-10.8Δ), sec
200
300
200
300
200
300
14.0
14.5
15.0
15.5
16.0
16.5
Distance, deg.
JR
JR
LG
LG
HR
GE
GE
Oct. 1, 1964
Sep. 24, 1964
STEP
LRSM
OBSERVED

Fig. 18

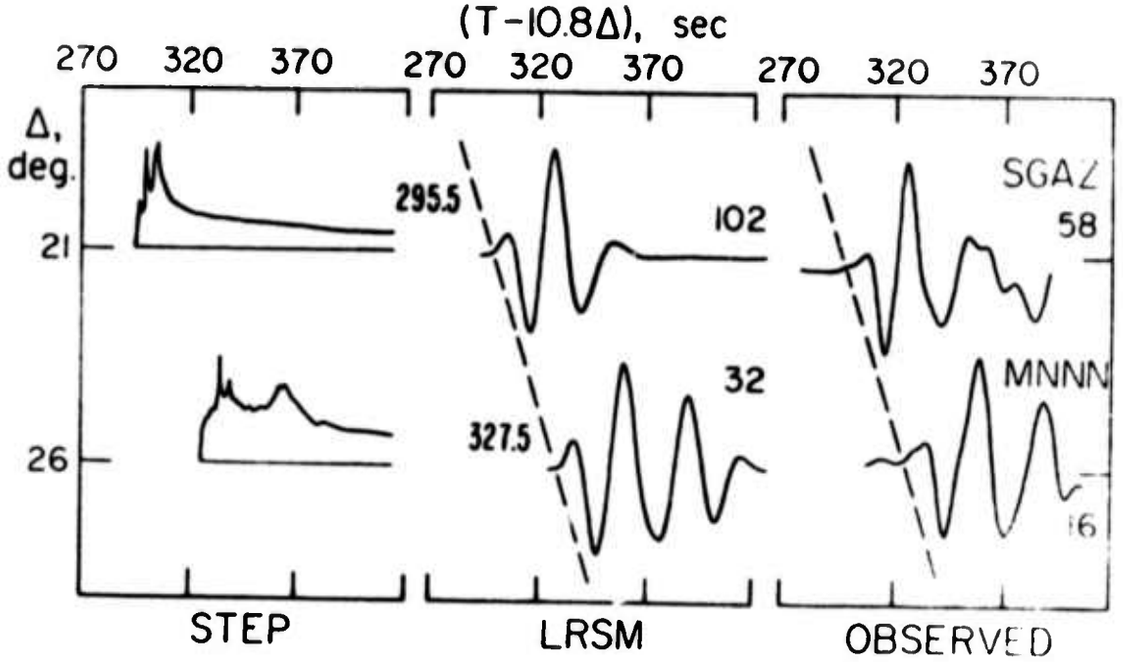
(T-10.8Δ), sec
270 320 370
270 320 370
270 320 370
Δ, deg.
21
26
295.5
102
327.5
32
SGAZ
58
MNNN
16
STEP
LRSM
OBSERVED

Fig. 19

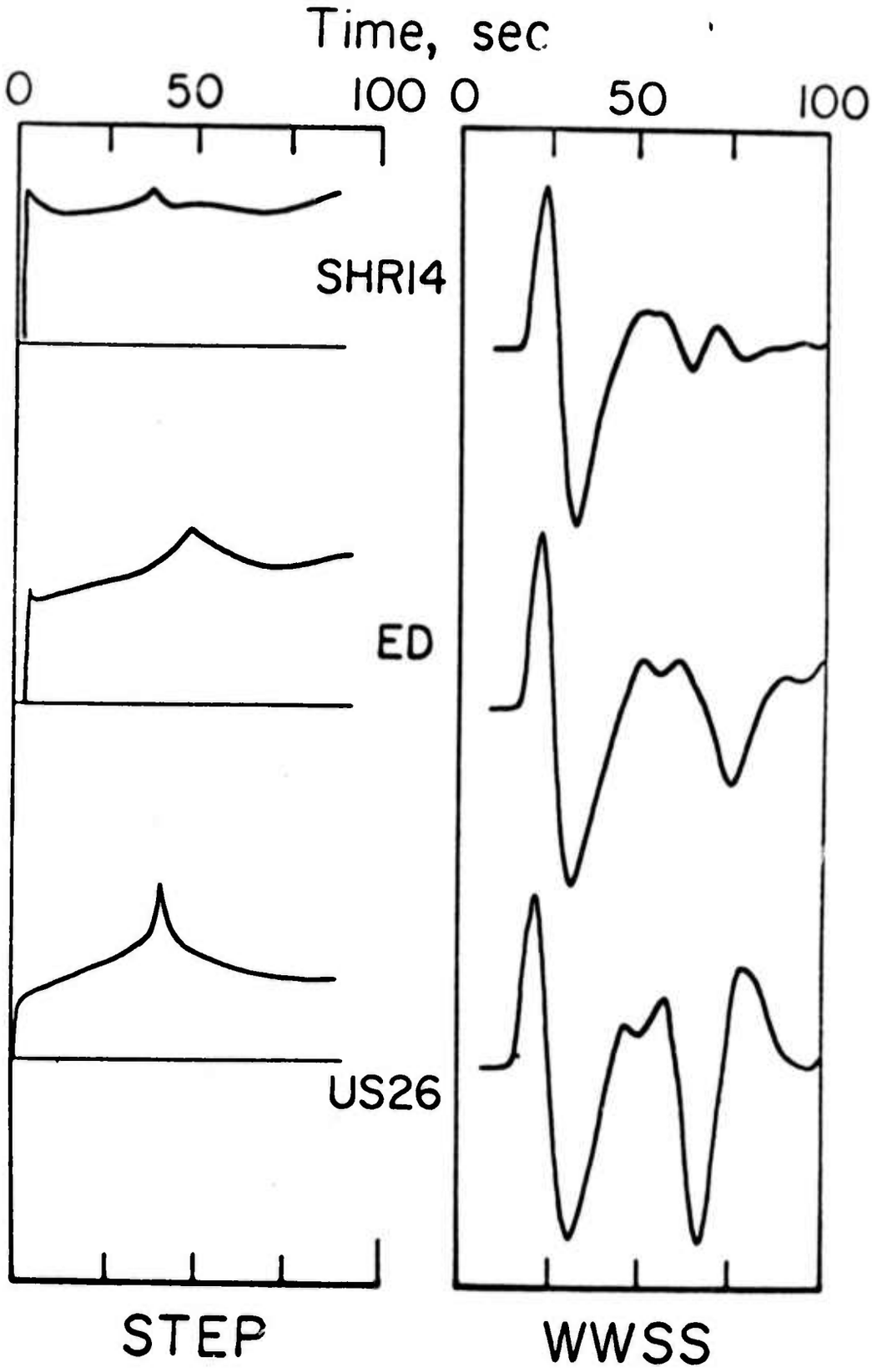

Fig. 20

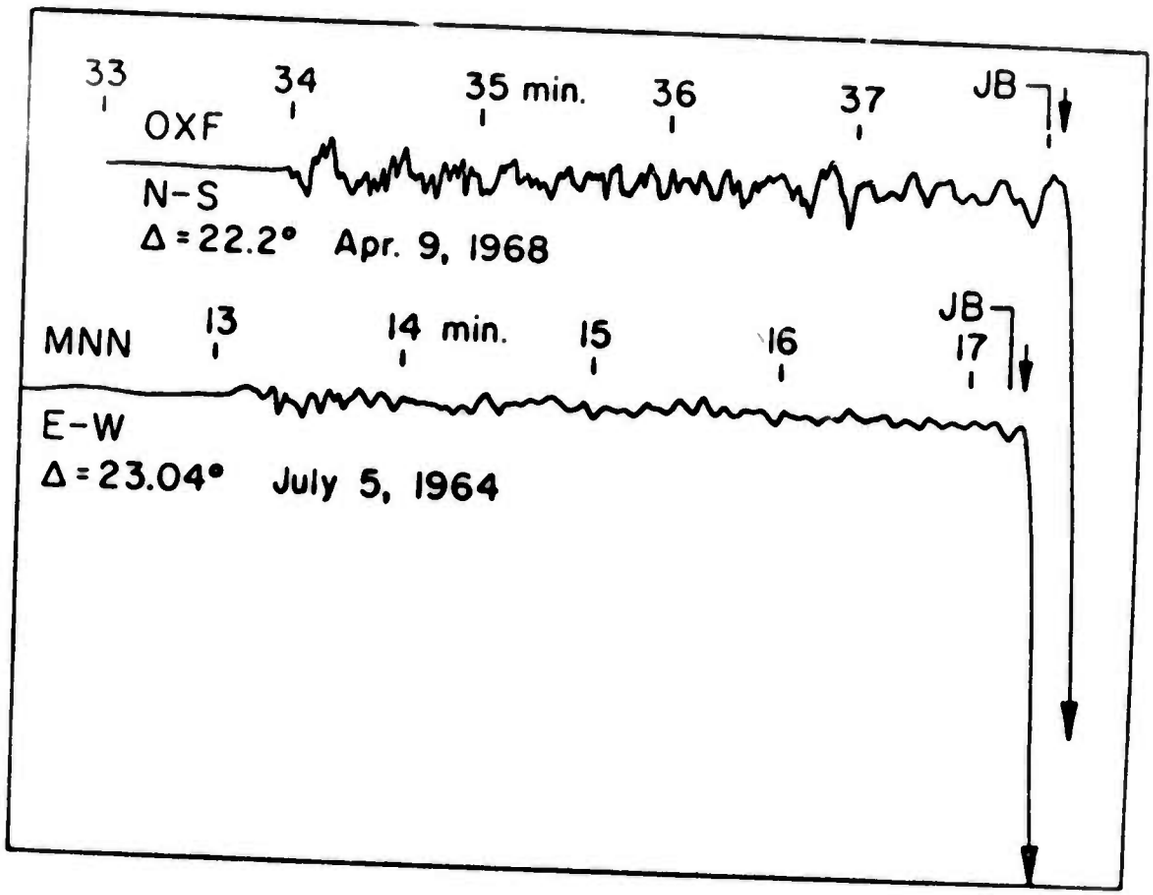
33
34
35 min.
36
37
JB
OXF
N-S
Δ = 22.2° Apr. 9, 1968
MNN
13
14 min.
15
16
JB
17
E-W
Δ = 23.04° July 5, 1964

Fig. 21

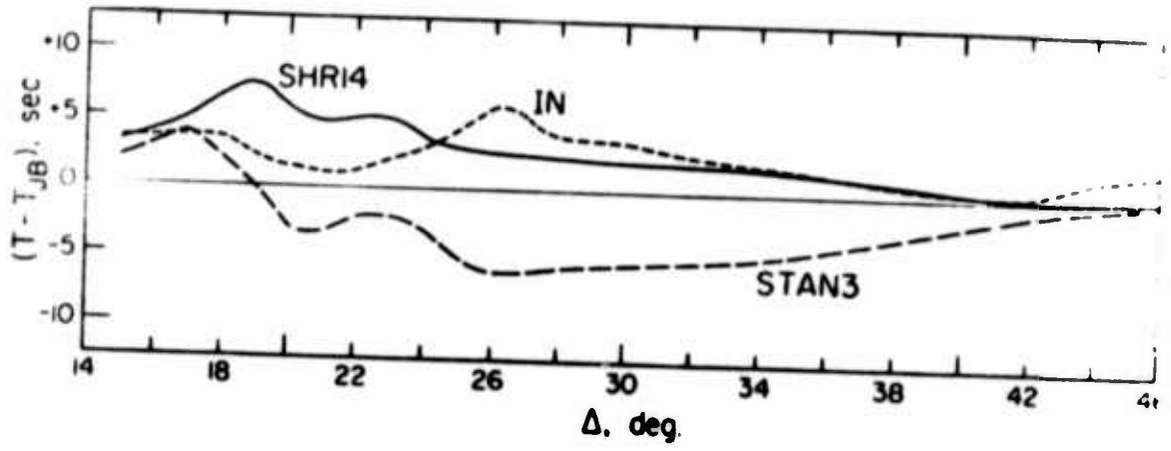

Fig. 22

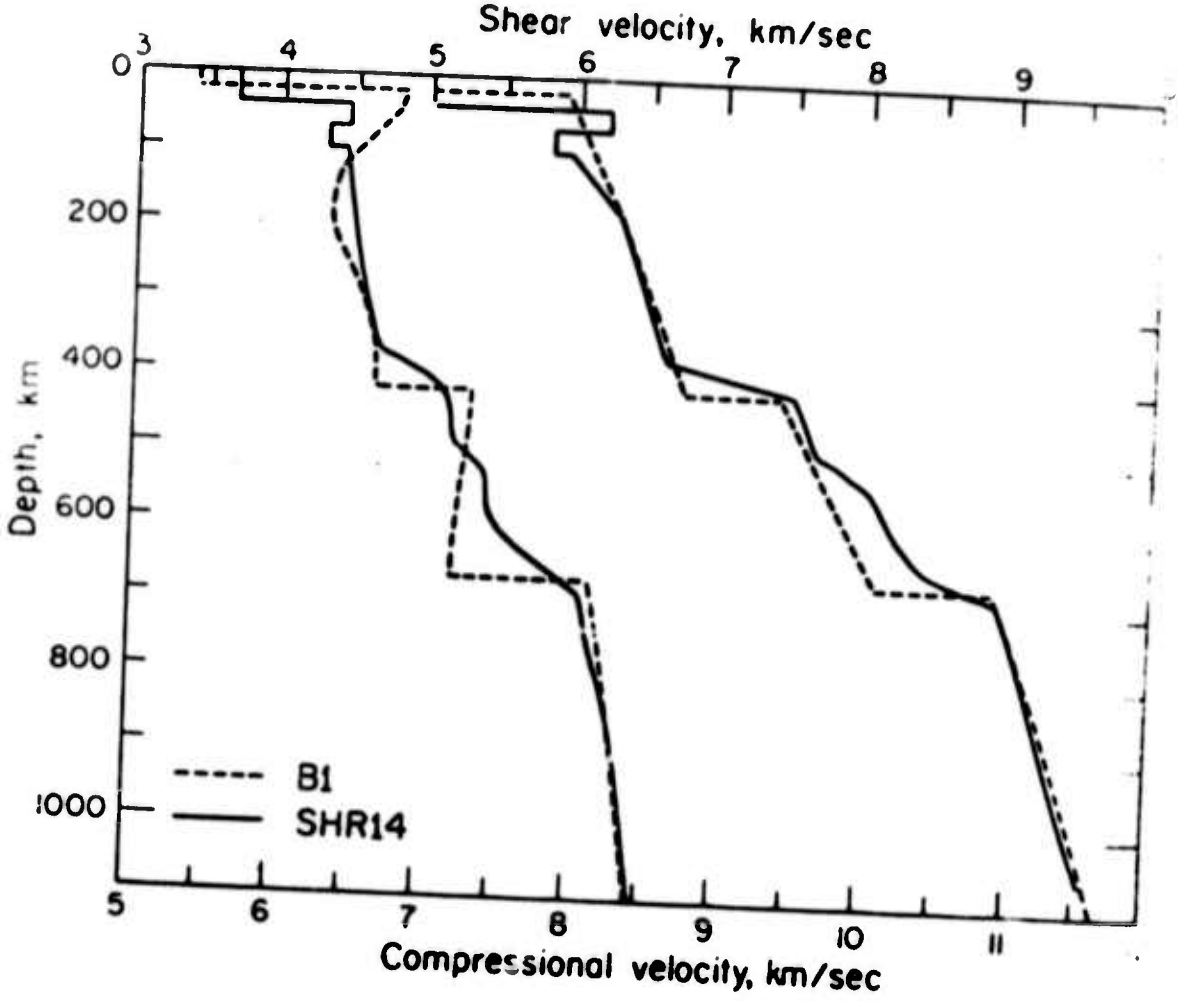
Shear velocity, km/sec
3
4
5
6
7
8
9
0
200
400
600
800
1000
Depth, km
B1
SHR14
5
6
7
8
9
10
11
Compressional velocity, km/sec

Fig. 23

Previous Technical Reports

1969 - Present

Teng, T. L., and Richards, P. G., 1969, Diffracted P, SV, and SH waves and their shadow boundary shifts: Jour. Geophys. Research, v. 74, no. 6, p. 1537-1555.

McGinley, J. R., Jr., and Anderson, D. L., 1969, Relative amplitudes of P and S waves as a mantle reconnaissance tool: Seismol. Soc. America Bull., v. 59, no. 3, p. 1189-1200.

Johnson, L. R., 1969, Array measurements of P velocities in the lower mantle: Seismol. Soc. America Bull., v. 59, no. 2, p. 973-1008.

McGinley, J. R., Jr., 1969, A comparison of observed permanent tilts and strains due to earthquakes with those calculated from displacement dislocations in elastic earth models: Ph.D. Thesis, California Institute of Technology, Pasadena, California.

Smith, M. L., and Franklin, J. N., 1969 Geophysical application of generalized inverse theory: Jour. Geophys. Research, v. 74, no. 10, p. 2783-2785.

Anderson, D. L., and Kovach, R. L., 196 , Universal dispersion tables, III, Free oscillation variational parameters: Seismol. Soc. America Bull., v. 59, no. 4, p. 1667-1693.

Anderson, D. L., and Julian, B. R., 1969, Shear velocities and elastic parameters of the mantle: Jour. Geophys. Research, v. 74, no. 12, p. p. 3281-3286.

Smith, S. W., McGinley, J. R., Jr., Johnson, L. R., and Scholz, C. H., 1969, Effects of large explosions on tectonic strain: Jour. Geophys. Research, v. 74, no. 12, p. 3308-3309.

Archambeau, C. B., Flinn, E. A., and Lambert, D. G., 1969, Fine structure of the upper mantle: Jour. Geophys. Research, v. 74, no. 25, p. 5825-5865.

Anderson, D. L., and Sammis, C. G., 1969, The low velocity zone: Geofisica Internac., v. 9, no. 1-3, p. 3-19.

Archambeau, C. B., and Sammis, C. G., 1970, Seismic radiation from explosions in prestressed media and the measurement of tectonic stress in the earth: Rev. Geophysics and Space Physics, v. 8, no. 3, p. 473-499.

Anderson, D. L., and Sammis, C. G., 1970, Partial melting in the upper mantle: Physics Earth and Planet. Interiors, v. 3, p. 41-50.

Arabasz, W. J., Brune, J. N., and Engen, G. R., 1970, Locations of small earthquakes near the trifurcation of the San Jacinto fault southeast of Anza, California: Seismol. Soc. America Bull., v. 60, no. 2, p. 617-627.

Jackson, D. D., and Anderson, D. L., 1970, Physical mechanisms of seismic-wave attenuation: Rev. Geophysics and Space Physics, v. 8, no. 1, p. 1-63.

Whitcomb, J. H., and Anderson, D. L., 1970, Reflection of P'P' seismic waves from discontinuities in the mantle: Jour. Geophys. Research, v. 75, no. 29, p. 5713-5728.

Julian, B. R., 1970, Regional variations in upper mantle structure beneath North America: Ph.D. thesis, California Institute of Technology, Pasadena, California.

Richards, P. G., 1970, A contribution to the theory of high frequency elastic waves, with applications to the shadow boundary of the earth's core: Ph.D. thesis, California Institute of Technology, Pasadena, California.

Wyss, Max, 1970, Observations and interpretations of tectonic strain release mechanisms: Ph.D. thesis, California Institute of Technology, Pasadena, California.

Archambeau, C. B., 1970, Theory of the seismic source: Proceedings of the Advanced Research Projects Agency Symposium on Discrimination of Earthquakes and Underground Explosions, Woods Hole, Massachusetts, July 20-23.

Gile, W. W., 1970, A mercury pendulum seismometer: IEEE Transactions on Geoscience Electronics (technical report).

Richards, P. G., 1971, Potentials for elastic displacement in spherically symmetric media: Acoust. Soc. America Jour., v. 50, no. 1, p. 188-197.

Richards, P. G., 1971, An elasticity theorem for heterogeneous media, with an example of body wave dispersion in the earth: Royal Astron. Soc. Geophys. Jour., v. 22, p. 453-472.

Liebermann, R. C., and Basham, P. W., 1971, Excitation of surface waves by the Aleutian underground explosion Milrow (October 2, 1969): Jour. Geophys. Research, v. 76, no. 17, p. 4030-4034.

Jordan, T. H., and Franklin, J. N., 1971, Optimal solutions to a linear inverse problem in geophysics: Natl. Acad. Sci. Proc., v. 68, no. 2, p. 291-293.

Hill, D. P., 1971, High frequency wave propagation in the earth: Theory and observation: Ph.D. thesis, California Institute of Technology, Pasadena, California.

Wyss, Max, Hanks, T. C., and Liebermann, R. C., 1971, Comparison of P-wave spectra of underground explosions and earthquakes: Jour. Geophys. Research, v. 76, no. 11, p. 2716-2729.

Hill, D. P., 1971, Velocity gradients and anelasticity from crustal body wave amplitudes: Jour. Geophys. Research, v. 76, no. 14, p. 3309-3325.

Jungels, P. H., and Anderson, D. L., 1971, Strains and tilts associated with the San Fernando earthquake, in The San Fernando, California, Earthquake of February 9, 1971: U.S. Geol. Survey Prof. Paper 733, p. 77-79.

Jordan, T. H., and Minster, J. B., 1971, An application of a stocha tic inverse to the geophysical inverse problem: Workshop on Mathematics of Profile Inversion, Ames Research Center, Moffitt Field, California, July 12-16.

Hill, D. P., 1971, Velocity gradients in the continental crust from head wave amplitudes: Am. Geophys. Union Mon. Ser. 14, p. 71-75.

Whitcomb, J. H., 1971, Reflections of P'P' seismic waves from 0 to 150 km depth under the Ninety-East Ridge, Indian Ocean, and the Atlantic-Indian Rise: Am. Geophys. Union Mon. Ser. 14, p. 211-225.

McKenzie, Dan, and Julian, Bruce, 1971, The Puget Sound, Washington, earthquake and the mantle structure beneath the northwestern United States: Geol. Soc. America Bull., v. 82, p. 3519-3524.

Helmberger, D. V., 1972, Long period body wave propagation from 4 to 13°: Seismol. Soc. America Bull., v. 62, no. 1, p. 325-341.

Archambeau, C. B., 1972, The theory of stress wave radiation from explosions in prestressed media: Royal Astron. Soc. Geophys. Jour., v. 29, p. 329-366.

Hanks, T. C., and Wyss, Max, 1972, The use of body-wave spectra in the determination of seismic source parameters: Seismol. Soc. America Bull., v. 62, no. 2, p. 561-589.

Hanks, T. C. and [illegible]her, W., 1972, A graphical representation of seismic source parameters: Jour. Geophys. Research, v. 77, no. 23, p. 4393-4405.

Alewine, R. W., 1972, Theoretical and observed distance corrections for Rayleigh wave magnitude: Seismol. Soc. America Bull., v. 62, no. 6, p. 1611-1619.

Helmberger, D. V., and Harkrider, D. G., 1972, Seismic source descriptions of underground explosions and a depth discriminate: Geophys. J. R. Astr. Soc., v. 31, p. 45-66.

Mizutani, H., and Abe, K., 1972, An earth model consistent with free oscillation and surface wave data: Phys. Earth Planet. Int., v. 5, p. 345-356.

Hill, D. P., 1972, Crustal and upper mantle structure of the Columbia Plateau from long-range seismic-refraction measurements: Geol. Soc. America Bull., v. 83, p. 1639-1648.

Lambert, D. G., Flinn, E. A., and Archambeau, C. B., 1972, A comparative study of the elastic wave radiation from earthquakes and underground explosions: Geophys. Jour., v. 29, p. 403-432.

Mitchell, B. J., 1973, Radiation and attenuation of Rayleigh waves from the southeastern Missouri earthquake of October 21, 1965: Jour. Geophys. Research, v. 78, no. 5, p. 886-899.

Kurita, T., 1973, A procedure and formulation for elucidating fine structure of the crust and upper mantle from seismological data: Seismol. Soc. America Bull., v. 63, no. 1, p. 189-209.

Wiggins, R., and Helmberger, D. V., 1973, Upper mantle structure of western United States: Jour. Geophys. Research, v. 78, no. 11, p. 1870-1880.

York, J. E., and Helmberger, D. V., 1973, Low velocity zone variations in the southwestern United States: Jour. Geophys. Research, v. 78, no. 11, p. 1883-1886.

Whitcomb, J. H., 1973, Part I. A study of the velocity structure of the earth by the use of core phases. Part II. The 1971 San Fernando earthquake series focal mechanisms and tectonics: Ph.D. Thesis, California Institute of Technology.

Jordan, T. H., 1973, Estimation of the radial variation of seismic velocities and density in the earth: Ph.D. Thesis, California Institute of Technology.

Whitcomb, J. H., 1973, Asymmetric P'P' -- an alternative to P'dP' reflections in the upper mantle (0-110 km): Seismol. Soc. America Bull., v. 63, p. 133-143.

Helmberger, D. V., 1973, Numerical seismograms of long-period body waves from seventeen to forty degrees: Seismol. Soc. America Bull., v. 63, p. 633-646.

Kurita, T., 1973, Regional variations in the structure of the crust in the Central United States from P-wave spectra: Seismol. Soc. America Bull., v. 63, p. 1663-1687.

Mitchell, B. J., 1973, Surface-wave attenuation and crustal anelasticity in Central North America: Seismol. Soc. America Bull., v. 63, p. 1057-1071.

Mitchell, B. J., and Helmberger, D. V., 1973, Shear velocities at the base of the mantle from observations of S and ScS: Jour. Geophys. Research, v. 78, p. 6609-6020.

Niazi, M., 1973, SH travel times and lateral heterogeneities in the lower mantle: Seismol. Soc. America Bull., v. 63, p. 2035-2046.

Helmberger, D. V., 1973, On the structure of the low velocity zone: Royal Astron. Soc. Geophys. Jour., v. 34, p. 251-263.

Helmberger, D. V., Generalized Ray Theory for Shear Dislocations: Bull. Seism. Soc. Am., in press.

Kurita, T., Upper Mantle Structure in the Central United States from P and S wave spectra: Phys. Earth and Planet. Inter., in press.

Minster, Jean-Bernard, 1974, Elastodynamics of failure in a continuum: Ph.D. Thesis, California Institute of Technology.

Alewine, Ralph W., 1974, Application of linear inversion theory toward the estimation of seismic source parameters, Ph.D. Thesis, California Institute of Technology.

PAPERS SUBMITTED FOR PUBLICATION

Hron, F., and Kanasewich, E. R., Synthetic seismograms for deep seismic sounding studies using generalized ray theory: submitted to Seismol. Soc. America Bull.

Minster, J. B., Transformation of multipolar expansions under rotation of the coordinate system: submitted to Royal Astron. Soc. Geophys. Jour.

Gile, W. W., and Taylor, R. A., Photon-coupled generated: submitted to Electronic Design

Wiggins, R. A., and Helmberger, D. V., Synthetic seismogram computation by expansion in generalized rays: submitted to Royal Astron. Soc. Geophys. Jour.

Jordan, T. H., and Anderson, D. L., Earth structure from free oscillations and travel times: submitted to Royal Astron. Soc. Geophys. Jour.

Geller, R. J., Body Force Equivalents for Stress Drop Seismic Sources: submitted to Geophys. Jour.

Geller, R. J., Representation theorems for an infinite shear fault: submitted to Jour. Geophys. Research.

Helmberger, D. V. and Engen, G. R., Upper-Mantle Shear Structure: submitted to Jour. Geophys. Research.

Langston, C.A. and Helmberger, D. V., Interpretation of Body and Rayleigh Waves from NTS to Tucson: submitted to Bull. Seism. Soc. Am.